A UNIFIED RELATIVISTIC TREATMENT OF TIDAL DISRUPTION EVENTS AND A NEW MODEL FOR SELF-INTERSECTIONS INVOLVING TIDAL DEBRIS STREAMS FOR SCHWARZSCHILD BLACK HOLES

by

Juan E. Servin

APPROVED BY SUPERVISORY COMMITTEE:

Michael Kesden, Chair

Mustapha Ishak-Boushaki

Lindsay J. King

Phillip C. Anderson

Yuri Gartstein

This dissertation is dedicated to my mother and father,

Tomasa and Jose, my siblings Nancy, Brayson, and Jose,

and my baby niece, Selena. Se lo dedico a ustedes!

A UNIFIED RELATIVISTIC TREATMENT OF TIDAL DISRUPTION EVENTS AND A NEW MODEL FOR SELF-INTERSECTIONS INVOLVING TIDAL DEBRIS STREAMS FOR SCHWARZSCHILD BLACK HOLES

by

JUAN E. SERVIN, BS, MS

DISSERTATION

Presented to the Faculty of

The University of Texas at Dallas

in Partial Fulfillment

of the Requirements

for the Degree of

DOCTOR OF PHILOSOPHY IN

PHYSICS

THE UNIVERSITY OF TEXAS AT DALLAS

August 2018

ACKNOWLEDGMENTS

The author would like to thank his dissertation committee members, and his doctoral advisor, Michael Kesden, in particular, for their support throughout the entire process.

June 2018

A UNIFIED RELATIVISTIC TREATMENT OF TIDAL DISRUPTION EVENTS AND A NEW MODEL FOR SELF-INTERSECTIONS INVOLVING TIDAL DEBRIS STREAMS FOR SCHWARZSCHILD BLACK HOLES

Juan E. Servin, PhD
The University of Texas at Dallas, 2018

Supervising Professor: Michael Kesden, Chair

This dissertation concerns the astrophysical phenomena known as tidal disruption events (TDEs), where stars are ripped apart by gravitational tides from their host galaxies' central supermassive black hole (SBH). Stars are driven onto orbits appropriate for disruption via gravitational interactions with their stellar neighbors, and it is these interactions that determine the rate at which we may observe TDEs. Observations for such events have gained popularity in recent years, as they provide an additional avenue for probing the spacetime near non-active galactic centers. Conveniently, measurements for galactic transients are already underway, and have found, up to the publication of this dissertation, a few dozen TDE candidates. Theoretical predictions for TDEs have been conducted under both Newtonian gravity and general relativity, with numerical simulations of TDE rates and the post disruption stream evolution being common examples. Models for TDEs, however, have proven to be a greater challenge, as the phenomenon covers a wide range of length and time scales. With the recent increased interest in black holes due to gravitational-wave detection, correcting current TDE models to fall more in line with observations can only aid our understanding of these massive galactic objects.

The rest of this dissertation is as follows. Our first chapter will introduce the reader to some basic history of TDEs, from their inception as a means to feed mass into galactic centers to their modern interpretations. We also provide a brief overview of Newtonian loss-cone theory (and its role in determining the rate at which TDEs are observed) and general relativity (which is used to correct for relativistic effects in the aforementioned loss-cone theory). The second chapter comprises a published work concerning a unified treatment of TDEs that maps Newtonian predictions to their relativistically corrected counterparts. Our third chapter presents a new model where we track the evolution of the post-disruption tidal stream and provides predictions for observations of light curves. Our fourth chapter discusses a generalization of our work in Chapter 2 from the Schwarzschild metric to the Kerr metric, and we close with some concluding remarks.

TABLE OF CONTENTS

LIST OF FIGURES

CHAPTER 1

INTRODUCTION AND BACKGROUND

1.1 A brief history of black holes and tidal disruption events

In 1915, Einstein published his theory of general relativity (GR), introducing the Einstein Field Equations (EFE),

$$G_{\alpha\beta} = \frac{8\pi G}{c^4} T_{\alpha\beta}, \tag{1.1}$$

where $G_{\alpha\beta} = R_{\alpha\beta} - \frac{1}{2} R g_{\alpha\beta}$ is the Einstein tensor, $R_{\alpha\beta}$ is the Ricci curvature tensor, $R = R^{\alpha}{}_{\alpha}$ is the trace of the Ricci tensor, $g_{\alpha\beta}$ is the metric tensor, $T_{\alpha\beta}$ is the stress-energy tensor, G is Newton's constant, and c is the speed of light. The left side of Eq. (1.1) describes the curvature of the spacetime, while the right side contains information about the mass, energy, and momentum content within the spacetime. Gravity was no longer treated as a force, and was instead interpreted as a manifestation of the curvature of spacetime due to the presence of matter. The properties of the spacetime are described by the metric tensor $g_{\alpha\beta}$, and in 1916 Schwarzschild (Schwarzschild, 1916) obtained a spherically symmetric vacuum solution to Eq. (1.1),

$$g_{\alpha\beta} = \begin{pmatrix} -\left(1 - \frac{2M}{r}\right) & 0 & 0 & 0 \\ 0 & \frac{r^2}{r^2 - 2Mr} & 0 & 0 \\ 0 & 0 & r^2 & 0 \\ 0 & 0 & 0 & r^2 \sin^2\theta \end{pmatrix}$$

where M is the mass inducing the spacetime curvature and $\{t, r, \theta, \phi\}$ are the Boyer-Lindquist coordinates. Since GR is a scale free theory, this solution can be applied to objects of any mass, including black holes.

Stars larger than our Sun with masses $9M_\odot \leq M_\star \leq 40M_\odot$, where $M_\odot \approx 2 \times 10^{30}$kg is the solar mass, are destined to die as supernovae (Heger et al., 2003), which are some of the brightest events in the Universe. Black holes are the result of the collapse of massive ($M_\star \geq 25M_\odot$) stars, where the degeneracy pressure between charged particles can no longer support the gravitational attraction between the particles. The mass collapses into a single point called a singularity that is enveloped by what is known as the event horizon, a boundary where the escape velocity becomes greater than the speed of light. According to the no-hair theorem (Carter, 1968) black holes can be fully characterized by three observable quantities: the black hole mass, $M_\bullet$, the (spin) angular momentum, a, and the charge q. This dissertation will concern itself only with the first two quantities.

At the centers of most galaxies are supermassive black holes (SBHs) with masses ranging between $10^6 M_\odot < M_\bullet < 10^{10} M_\odot$. Their smaller counterparts, often referred to as solar-mass black holes, have masses up to about $100M_\odot$. These smaller BHs were involved in the recent detection of gravitational waves (Abbott et al., 2016), and have contributed to a recent rise in interest for black holes in general. Note the rather large gap between the above mass ranges. As previously mentioned, stellar-mass black holes are created from the deaths of very large stars, and would thus require some mass source to grow into SBHs. There are currently three theories for SBH formation (Volonteri, 2010),

(1) SBHs are the remnants of first generation (PopIII) stars,

(2) SBH formation is triggered by gas-dynamical instabilities,

(3) SBH seeds are formed via stellar-dynamical processes.

In the first theory stellar-mass black holes grow by accreting gas, either from neighboring stars or from galactic gas clouds. The second theory postulates that SBHs form from the direct collapse of gas clouds and thus relaxes the need for gas accretion. The third theory

involves stellar collisions, where stars interact with each other gravitationally and possibly deflect one another towards the SBH. The latter process, while no longer favored for SBH formation, does lead to the phenomenon known as tidal disruption.

Tidal disruption events (TDEs) occur when stars are ripped apart by tidal stresses due to the SBH's gravity. Tides result from force gradients in non-uniform fields, where sections of an object become subject to differing amounts of acceleration with respect to one another. In the context of TDEs, stars are ripped apart when gravitational tides due to an SBH overcome the self gravitation of the star on its constituent gas particles. Treating tidal disruption as a two body problem, appropriate because the SBH dominates the dynamics of stars near their pericenters, we can define parameter thresholds for the orbits of stars that would lead to TDEs. Let r be the radial distance from the SBH to the center of the star and $0 < R < R_\odot$ be the radial distance from the center of the star outward. The Newtonian gravitational acceleration is $a(r) = GM_\bullet/r^2$, and thus the tidal acceleration on the outermost point of the star (with $R = R_\odot$) is,

$$a(R_\odot) = \frac{GM_\bullet}{(r - R_\odot)^2} \implies \frac{GM_\bullet}{r^2} + \frac{2GM_\bullet}{r^3} R_\odot + ... \tag{1.2}$$

where the right side of the equation is a Taylor expansion, valid because the radial distance from the star to the SBH is much greater than the size of the star ($R \ll r$). The zeroth order term in our expansion represents a uniform gravitational field, so to first order the tidal acceleration is approximately $GM_\bullet R_\odot/r^3$. Setting this tidal acceleration equal to the self gravity of the star on its outermost point would then allow us solve for the radial distance r_t (known as the tidal radius) from the SBH that the star must reach to be disrupted,

$$\frac{GM_\bullet R_\odot}{r^3} = \frac{GM_\odot}{R_\odot^2} \rightarrow r_t = \left(\frac{M_\bullet}{M_\odot}\right)^{1/3} R_\odot. \tag{1.3}$$

After disruption roughly half of the original star's mass becomes more tightly bound to the SBH (the other half becomes unbound), and it is this bound half that will eventually

power the TDE flare. The most bound element will have energy $E_t = GM_\bullet R_\odot / r_t^2$ with corresponding orbital period $\tau_{\rm mb}$,

$$\tau_{\rm mb} = 2\pi \left(\frac{(GM_\bullet)^2}{8E_{\rm t}^3} \right)^{1/2} = 2\pi r_t^3 \left(8GM_\bullet R_\odot^3 \right)^{1/2} = 41 \left(\frac{M_\bullet}{10^6 M_\odot} \right)^{1/2} \text{ days.} \tag{1.4}$$

In the late 1970s and the 1980s theoretical predictions (Rees, 1988; Evans and Kochanek, 1989; Genzel et al., 1986; Luminet and Carter, 1983) introduced what is now considered the signature feature of tidal disruption. Suppose the star had a flat mass-energy distribution $dM/dE = M_\odot/(2E_t)$. From Kepler's third law, we know that the orbital period of an object is related to its binding energy via $\tau \propto E^{-3/2}$. The rate at which gas falls into the SBH, called the fallback accretion rate $dM/d\tau$, is,

$$\frac{dM}{d\tau} = \frac{dM}{dE}\frac{dE}{dt} = \frac{\sqrt{2}}{3\pi G} \left(\frac{GM_\odot}{R_\odot} \right)^{3/2} \left(\frac{M_\odot}{M_\bullet} \right)^{1/2} \left(\frac{t}{\tau_{\rm mb}} \right)^{-5/3}. \tag{1.5}$$

The luminosity L is directly proportional to this fallback accretion rate, and so transient signals with a decay rate following $t^{-5/3}$ could be used to identify TDEs. At time $t = \tau_{\rm mb}$ the peak luminosity corresponding to the accretion rate from Eq. 1.5 would be (Stone et al., 2018),

$$L_{\rm peak} = \eta \frac{dM}{dt} c^2 = 1.68 \times 10^{46} \left(\frac{\eta}{0.1} \right) \left(\frac{M_\bullet}{10^6 M_\odot} \right)^{-1/2} \text{ erg/s} \tag{1.6}$$

where η is the radiative efficiency of the viscously accreted stream. We discuss viscous accretion in more detail in the next section. The Eddington luminosity $L_{\rm Edd}$ is given by,

$$L_{\rm Edd} = \frac{4\pi G M_\bullet c M_{\rm p}}{\sigma_{\rm T}} = 1.25 \times 10^{44} \left(\frac{M_\bullet}{10^6 M_\odot} \right) \text{erg/s} \tag{1.7}$$

where $M_{\rm p}$ is the proton mass and $\sigma_{\rm T}$ is the Thompson scattering cross-section for an electron. The Eddington luminosity is the maximum luminosity that a radiating body can achieve

such that the inward pull of gravity is balanced out by the outward radiation pressure. As a fraction of the Eddington luminosity, our $L_{\rm peak}$ is equal to,

$$\frac{L_{\rm peak}}{L_{\rm Edd}} = 130 \left(\frac{\eta}{0.1}\right) \left(\frac{M_\bullet}{M_\odot}\right)^{-3/2}, \tag{1.8}$$

meaning that for SBH of masses $10^6 - 10^7 M_\odot$ TDE flares would be brighter than quasars if they could achieve this peak luminosity.

We show in Fig. 1.1 one such set of observations, where the $t^{-5/3}$ decay is seen in the near UV and optical light bands (Gezari et al., 2012). More recent predictions (Wang and Merritt, 2004; Stone and Metzger, 2016; Magorrian and Tremaine, 1999) have provided theoretical observation rates as functions of the SBH masses and orbital parameters of stars. Numerical simulations (Guillochon and Ramirez-Ruiz, 2013; Lodato et al., 2009; Hayasaki et al., 2013) and theoretical models (Dai et al., 2015; Bonnerot et al., 2016; Guillochon and Ramirez-Ruiz, 2015) for the gaseous debris left behind by the disrupted stars have also been conducted, including some work (Luminet and Marck, 1985; Laguna et al., 1993; Diener et al., 1997; Ivanov et al., 2003; Ivanov and Chernyakova, 2006; Kesden, 2012; Sądowski et al., 2016) that has opted to study general relativistic effects on these predictions.

Studies of dark matter and dark energy during these times led to observational searches for supernovae which, fortuitously, are also light transients. The Sloan Digital Sky Survey (SDSS) (Wang et al., 2012), the All-Sky Automated Survey for SuperNovae (ASASSN) (Holoien et al., 2014), and the Palomar Transient Factory (PTF) (Hung et al., 2017) have found candidates in the optical band, and the Galaxy Evolution Explorer (GALEX) (Gezari et al., 2009) in the ultraviolet band. Earlier candidates were found in X-ray surveys by the Roentgenstellit (ROSAT) (Weisskopf et al., 2010) and XMM-Newton (Komossa and Bade, 1999) surveys. Altogether, these have shown rates consistent with those predicted by early models. Future surveys for light transients such as the Large

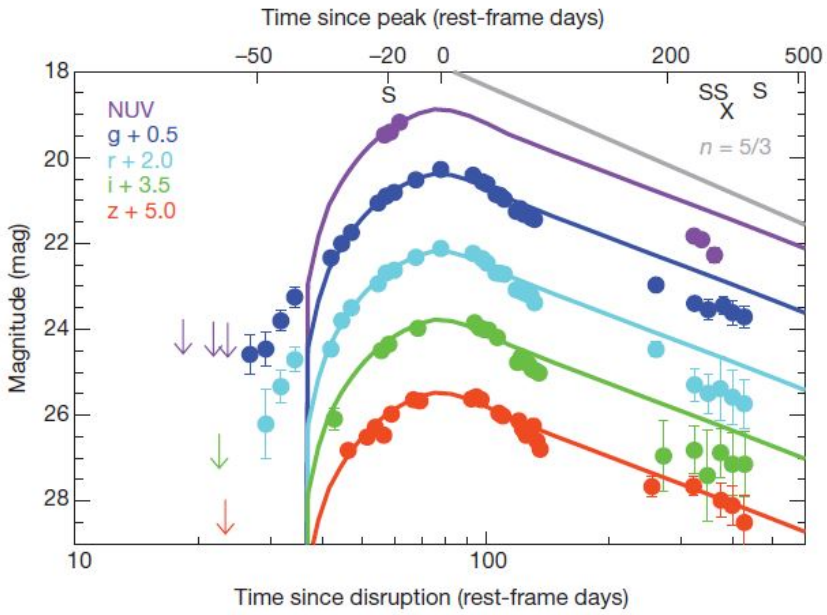

Figure 1.1: Light curves from PS1-10jh of a TDE candidate in the near-ultraviolet (NUV), green (g), red (r), infrared (i), and near infrared (z). The curves are vertically offset for presentational purposes. Figure adapted by permission from Springer Nature: Nature (Gezari et al., 2012), ©2012, Springer Nature.

Synoptic Survey Telescope (LSST) scheduled for 2021 and eROSITA, the Russian and German joint mission for X-ray observations scheduled to launch late 2018, will further bolster these numbers.

1.2 Viscous accretion of gas by supermassive black holes

After a star has been tidally disrupted, roughly half of the original star's mass becomes more tightly bound to the SBH and the other half becomes unbound. The TDE is powered by the conversion of gravitational potential energy into thermal energy via viscous accretion (Shakura and Sunyaev, 1973) of a circularized tidal stream, called an accretion disk. Viscosity in this accretion disk produces torques (Pringle, 1981) between neighboring sections of gas and causes angular momentum to be transported from the center of the disk outward. This allows the gas closest to the SBH to reach the innermost stable circular or-

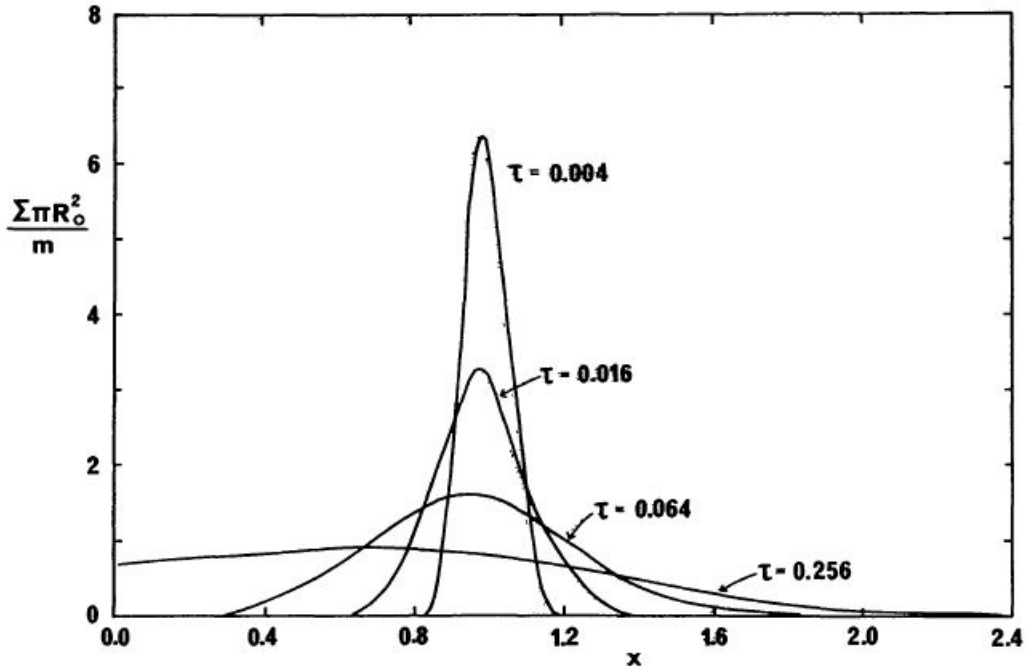

Figure 1.2: The viscous evolution of a ring of matter with mass m where Σ is the surface mass density, R_0 is the initial position, $x = R/R_0$, and τ is the time in units of $t_{\rm visc}/12$. As time progresses, the torques of the outer ring on the inner ring causes an outward flow of angular momentum, resulting in the inner (outer) mass tending to smaller (larger) x positions. Republished with permission of Annual Reviews, Inc., from "Accretion discs in astrophysics" (Pringle, 1981), Vol. 19: 137-162, © 1981; permission conveyed through Copyright Clearance Center, Inc.

bit (ISCO) and be accreted and causes the outer ring to expand to larger radii, as can be seen in Fig. 1.2. Viscous evolution occurs on the viscous time $t_{\rm visc}$,

$$t_{\rm visc} = \alpha^{-1} \left(\frac{h}{r}\right)^{-2} \tau_{\rm circ} \approx 10^3 \tau_{\rm circ}, \tag{1.9}$$

where $\alpha \approx 0.1$ is the dimensionless Shakura-Sunyaev parameter used to define the kinematic viscosity ν,

$$\nu = \alpha c_s h, \tag{1.10}$$

where c_s is the gas sound speed, h is the scale height of the accretion disk with $h/r \approx 0.1$, and $\tau_{\rm circ}$ is the orbital period of the accretion disk at $r_{\rm circ} = 2r_t$. The outer region of the accretion disk (at radius R) exerts a torque T on the inner disk,

$$T = (2\pi R)\,\nu\Sigma R^2 \frac{d\Omega}{dR}, \tag{1.11}$$

where Σ is the disk surface density and $\Omega(R)$ is the angular velocity of the gas given by,

$$\Omega(R) = \left(\frac{GM_\bullet}{R^3}\right)^{1/2}. \tag{1.12}$$

The derivative of Eq. (1.12) is negative, meaning that the torque T on the inner disk is negative and it loses angular momentum as previously stated.

The semi-major axis of the accretion disk is equal to twice the tidal radius, $a_{\rm circ} = 2r_t$, and so its orbital period is,

$$\tau_{\rm circ} = 2\pi \left(\frac{a_{\rm circ}^3}{GM_\bullet}\right)^{1/2} = 2\pi \left(\frac{8r_t^3}{GM_\bullet}\right)^{1/2}. \tag{1.13}$$

Compare this viscous time to the orbital period $\tau_{\rm mb}$ of the most bound pre-circularized stream element,

where we have used the expression $a_{\rm mb} = GM_\bullet/(2E_{\rm mb})$, with $E_{\rm mb} = GM_\bullet R_\star/r_t^2$ being the binding energy of the most bound stream element, to derive Eq. (1.4). As a ratio of the accretion disk's orbital period $\tau_{\rm mb}$ is,

$$\frac{\tau_{\rm mb}}{\tau_{\rm circ}} = \left(\frac{a_{\rm mb}}{a_{\rm circ}}\right)^{3/2} = \left(\frac{r_t}{4R_\star}\right)^{3/2} = \frac{1}{8}\left(\frac{M_\bullet}{M_\star}\right)^{1/2}. \tag{1.14}$$

For a $10^6 M_\odot$ SBH, then, we would have $\tau_{\rm mb}/\tau_{\rm circ} = 125$, short compared to the viscous time $t_{\rm visc} = 10^3\tau_{\rm circ}$. This suggests that the optical radiation released during the inelastic collisions between the pre-circularized stream elements could be used as a precursor for the X-rays released during viscous accretion.

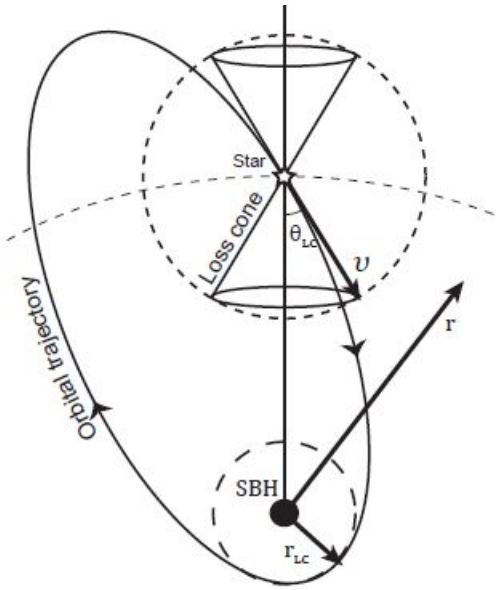

Figure 1.3: A depiction of the loss cone using a phase space of position and velocity. It is called the "loss cone" because stars with velocities inside the cone are "lost" due to tidal disruption. The loss cone radius here is labeled $r_{\rm LC}$. Republished with permission of IOP Publishing, LTD, from "Loss-cone dynamics" (Merritt, 2013), Volume 30, Number 24, © 2013; permission conveyed through Copyright Clearance Center, Inc.

1.3 Newtonian loss-cone theory

We can use this tidal radius from Eq. (1.3) to define a region in phase space (of position and velocity) where stars are at risk of being disrupted, known as the loss cone, which we show in Fig. 1.3. Stars whose pericenters fall within the tidal radius and with velocity vectors that point inside the loss cone will be disrupted upon pericenter passage. Due to the time invariance of the gravitational field and the spherical symmetry of the system the energy, E, and angular momentum, L, are both conserved. A star on a parabolic orbit with pericenter $r = r_t$ would have an angular momentum of,

$$L_t = \sqrt{2GM_\bullet r_t}. \tag{1.15}$$

We can then define the boundaries of the loss region using a phase space of energy and angular momentum, which we show in Fig. 1.4. We arrive to a bit of a conundrum: if all

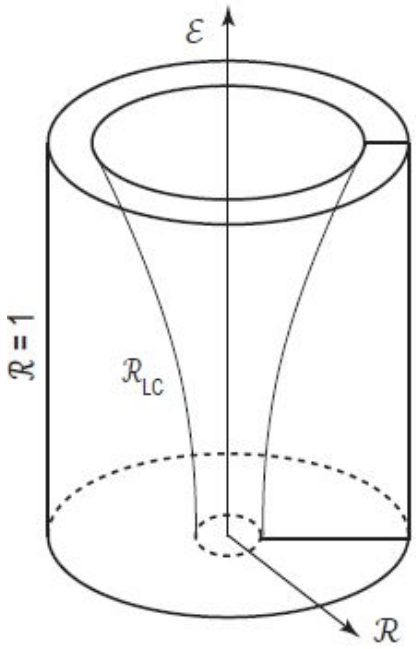

Figure 1.4: The loss region using an energy-angular momentum phase space. Here, $\mathcal{E} = -E$ and $\mathcal{R} = L^2/L_c^2$ are the binding energy and rescaled squared angular momentum, respectively, L_c is the angular momentum that a circular orbit with binding energy $\mathcal{E}$ would have, and $\mathcal{R}_{\rm LC}$ is the disruption threshold for the variable $\mathcal{R}$. Stars inside the funnel defined by $\mathcal{R}_{\rm LC}$ are disrupted once they reach a radial distance of $r_{\rm LC}$ from the SBH. Republished with permission of IOP Publishing, LTD, from "Loss-cone dynamics" (Merritt, 2013), Volume 30, Number 24, © 2013; permission conveyed through Copyright Clearance Center, Inc.

stars within the loss region will eventually be disrupted (and thus removed from the loss region), how are observations of TDEs in the local (present day) Universe possible?

Although we treated tidal disruption as a two-body problem in the derivation of the tidal radius, in reality the stars can interact with their stellar neighbors. These interactions can lead to gravitational scattering and cause an exchange of binding energies and angular momenta among the stars. This means that it is possible for stars to diffuse across the boundary of the loss region, and it is this diffusion that determines the rate at which we may observe TDEs. To determine the rate of this diffusion we use the (orbit-averaged) Fokker-Planck equation, which, in terms of the energy and angular momentum variables $\mathcal{E}$ and $\mathcal{R}$, is (Cohn and Kulsrud, 1978),

$$\frac{\partial N}{\partial t} = -\frac{\partial}{\partial \mathcal{E}}\left(N\left\langle \Delta\mathcal{E}\right\rangle_t\right) + \frac{1}{2}\frac{\partial^2}{\partial \mathcal{E}^2}\left(N\left\langle \left(\Delta\mathcal{E}\right)^2\right\rangle_t\right) - \frac{\partial}{\partial \mathcal{R}}\left(N\left\langle \Delta\mathcal{R}\right\rangle_t\right) + \frac{1}{2}\frac{\partial^2}{\partial \mathcal{R}^2}\left[N\left\langle \left(\Delta\mathcal{R}\right)^2\right\rangle_t\right] + \frac{\partial^2}{\partial \mathcal{E}\partial \mathcal{R}}\left[N\left\langle \Delta\mathcal{E}\Delta\mathcal{R}\right\rangle_t\right] \tag{1.16}$$

where N is the number density of stars in the phase space $(\mathcal{E}, \mathcal{R})$, $\langle\Delta\mathcal{E}\rangle$ and $\langle\Delta\mathcal{R}\rangle$ are the diffusion coefficients for the binding energy and rescaled angular momentum, respectively, and the subscript t denotes an orbit averaged quantity. These diffusion coefficients are generally very complex, and we will not concern ourselves with the details of their derivations here. What is important is that these coefficients can help us define the flux of stars into the loss cone for a particular binding energy $\mathcal{E}$ as,

$$F\left(\mathcal{E}\right) = -\frac{d}{dt}\left[\int_{\mathcal{R}_t}^{1} N\left(\mathcal{E}, \mathcal{R}\right) d\mathcal{R}\right], \tag{1.17}$$

where $\mathcal{R}_t$ is the value of $\mathcal{R}$ below which stars are within the loss region. In words, Eq. (1.17) states that the flux of stars into the loss cone is equal to the number of stars leaving the region outside the loss cone, for a particular value of $\mathcal{E}$. The TDE rate $\dot{N}$ could then be determined by integrating over all possible binding energies,

$$\dot{N} = \int F(\mathcal{E}) d\mathcal{E}. \tag{1.18}$$

The TDE rate thus depends on the distribution of stars over these binding energies. Throughout this dissertation, we will be using an isothermal stellar density profile of the form,

$$\rho(r) = \frac{\sigma^2}{2\pi G r^2}, \tag{1.19}$$

where r is the radial distance from the SBH and σ is the velocity dispersion of the stars within the galaxy that is related to the SBH mass via $M_\bullet = 1.48 \times 10^8 M_\odot (\sigma/(200\text{km/s}))^{4.65}$,

known as the $M_\bullet - \sigma$ relation (Merritt, 2013). This isothermal profile is a good approximation (Magorrian and Tremaine, 1999) for the power-law galaxies that dominate the TDE rate, and closely follows the theoretically predicted (Bahcall and Wolf, 1976) $\rho \propto r^{-7/4}$ for galactic centers with SBHs. The corresponding gravitational potential is then,

$$\psi(r) = \frac{GM_\bullet}{r} - 2\sigma^2 \ln\left(\frac{r}{r_h}\right) = -\Phi(r), \tag{1.20}$$

where the potential is defined such that it vanishes at the influence radius $r_h = GM_\bullet/\sigma^2$. The distribution function f is equal to the number of stars found within a volume in phase space. One could use Eddington's formula (Binney and Tremaine, 2008) to solve for this distribution function as,

$$f(\mathcal{E}) = \frac{1}{\sqrt{8}\pi^2 M_\odot} \frac{d}{d\mathcal{E}} \int_{-\infty}^{\mathcal{E}} \frac{d\rho}{d\psi} \frac{d\psi}{\sqrt{\mathcal{E} - \psi}}. \tag{1.21}$$

This distribution function is used to calculate the boundary conditions and diffusion coefficients for Eq. (1.16), which gives the TDE rate $\dot{N}$ through Eqs. (1.17) and (1.18). We show this TDE rate as a function of SBH mass in Fig. 1.5.

The reader may find the inverse relationship between the SBH mass and the TDE rate counterintuitive, as larger SBH masses would lead to larger tidal radii and, presumably, higher TDE rates. The density of stars, however, falls off as $\rho \propto r^{-2}$ according to Eq. (1.19), and so there is less scatter through the loss-cone boundary for larger SBH masses. One can then categorize TDE rates as being either in the full loss cone (FLC) and the empty loss cone (ELC) regime. While in the FLC (which corresponds to lower mass SBHs) stars diffuse into the loss cone faster than the SBH can consume them, meaning that all orbits that can be disrupted are always occupied. For the ELC (corresponding to very large SBHs), diffusion into the loss cone is very inefficient, and the SBH consumes stars as fast as they are being supplied.

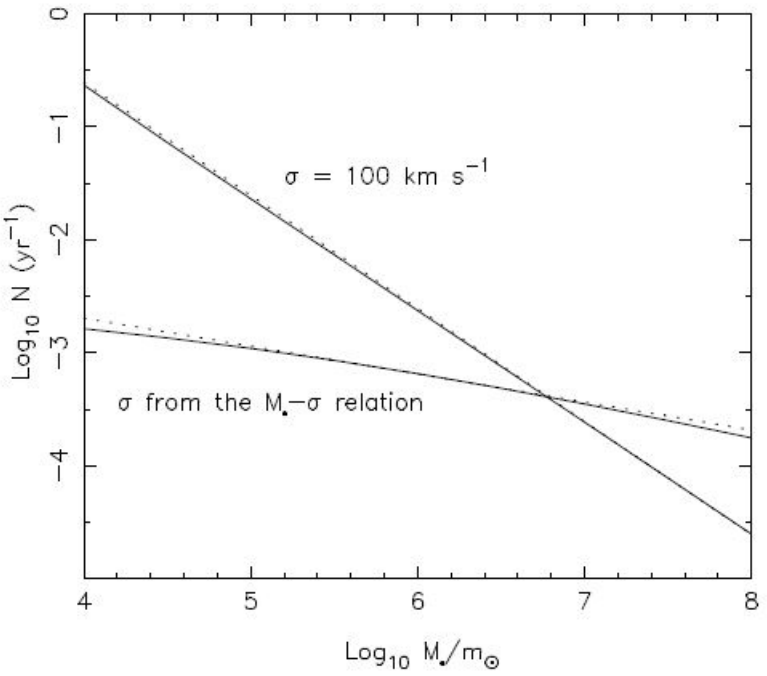

Figure 1.5: The TDE rate $\dot{N}$, labeled $N(\mathrm{yr}^{-1})$ in the figure, as a function of SBH mass $M_\bullet$ for a galaxy with an isothermal density profile. The velocity dispersion, σ, is obtained from the $M_\bullet - \sigma$ relation $M_\bullet = 1.48 \times 10^8 M_\odot (\sigma/200\mathrm{km/s})^{4.65}$, and is roughly equal to $\sigma = 100\mathrm{km/s}^{-1}$ for stars in the Milky Way galaxy core (Genzel et al., 1996). Figure adapted from (Wang and Merritt, 2004), © AAS. Reproduced with permission.

1.4 General Relativity and Tidal Disruption

We now discuss general relativity and its relevance to tidal disruption. The loss-cone physics in the previous section was conducted under Newtonian gravity, but black holes are intrinsically relativistic objects. The gravitational interactions among the stars that lead to diffusion accross the loss-cone boundary happen near the influence radius r_h, meaning that Eq. (1.17) is still valid. We need only adjust the thresholds for $\mathcal{R}$ to account for relativistic effects on the tidal stresses as disruption occurs near the SBH. Compare the tidal radius, which scales as $r_t \propto M_\bullet^{1/3}$, to the gravitational radius, $r_g = GM_\bullet/c^2$, which scales linearly in $M_\bullet$. With increasing SBH mass the ratio r_t/r_g approaches unity, implying that the disruption occurs

at more extreme spacetime curvatures (due to the proximity to the SBH event horizon) and relativistic effects become more important.

As stated in Section 1.1, gravity is no longer treated as a force under GR and is instead treated as a manifestation of the curvature of spacetime due to the presence of matter. The properties of the spacetime are described by a metric tensor $g_{\alpha\beta}$, where Greek letters are used as indices for the coordinates of the spacetime. Throughout this dissertation we will use Boyer-Linquist (BL) coordinates $\{t, r, \theta, \phi\}$, where t is the coordinate time, r is the radial coordinate, θ is the polar coordinate, and ϕ is the azimuthal coordinate, in units of $G = c = 1$. The Schwarzschild metric in these BL coordinates is,

$$ds^2 = -\left(1 - \frac{2M_\bullet}{r}\right) dt^2 + \frac{r^2}{r^2 - 2M_\bullet r} dr^2 + r^2(d\theta^2 + \sin\theta^2 d\phi^2). \tag{1.22}$$

Particles solely under the influence of gravity will travel on timelike geodesics $x^\mu(\tau)$ satisfying the equation,

$$\frac{d^2x^\mu}{d\tau^2} + \Gamma^\mu_{\rho\sigma}\frac{dx^\rho}{d\tau}\frac{dx^\sigma}{d\tau} = 0, \tag{1.23}$$

where τ is the proper time, $u^\mu = dx^\mu/d\tau$ is the 4-velocity of the particle, and $\Gamma^\mu_{\rho\sigma}$ are the Christoffel symbols, which in terms of the metric tensor are,

$$\Gamma^\mu_{\nu\xi} = \frac{1}{2} g^{\mu\sigma}(\partial_\nu g_{\xi\sigma} + \partial_\xi g_{\nu\sigma} - \partial_\sigma g_{\nu\xi}) \tag{1.24}$$

where the ∂_α denote partial derivatives. The Schwarzschild metric is time invariant and spherically symmetric, so we retain energy and angular momentum conservation as in the Newtonian case, with total energy E and angular momentum L equal to,

$$E \equiv -g_{\alpha\beta}u^\alpha \left(\frac{\partial}{\partial t}\right)^\beta, \tag{1.25a}$$

$$L \equiv g_{\alpha\beta}u^\alpha \left(\frac{\partial}{\partial \phi}\right)^\beta, \tag{1.25b}$$

where $\left(\frac{\partial}{\partial t}\right)^{\beta}$ and $\left(\frac{\partial}{\partial \phi}\right)^{\beta}$ are Killing vector fields along which the metric is preserved.

Our interpretation of gravity under GR necessitates a reinterpretation of tides. Tidal stresses arise due the tendency of parallel geodesics to deviate from each other in the presence of spacetime curvature. If two neighboring geodesics are separated by an infinitessimal spacelike 4-vector X^{β}, we can define the "relative velocity" between the geodesics as,

$$V^{\mu} = u^{\rho} \nabla_{\rho} X^{\mu}, \tag{1.26}$$

and the "relative acceleration" between two geodesics as,

$$A^{\mu} = u^{\rho} \nabla_{\rho} V^{\mu}, \tag{1.27}$$

where ∇_{α} are covariant derivatives. We then have the geodesic deviation equation,

$$\frac{d^2 X^{\beta}}{d\tau^2} = u^{\mu} \nabla_{\mu} (u^{\alpha} \nabla_{\alpha} X^{\beta}) = -C^{\beta}{}_{\alpha} X^{\alpha}, \tag{1.28}$$

where,

$$C^{\beta}{}_{\alpha} \equiv R^{\beta}{}_{\mu\alpha\nu} u^{\mu} u^{\nu}, \tag{1.29}$$

is the tidal tensor, with $R^{\beta}{}_{\mu\alpha\nu}$ being the Riemann curvature tensor.

The global BL coordinates above are not well suited for describing events on the scale of a solar radius. We instead transform to the more local Fermi-normal (FN) coordinates (Manasse and Misner, 1963) (τ, X^{i}), defined as follows. Let G be a geodesic traced by the center of the star at an arbitrary proper time $\tau = 0$ and let $\{\lambda^{\mu}{}_{(0)}, \lambda^{\mu}{}_{(i)}\}$ be an orthonormal tetrad defined by these coordinates, where $\lambda^{\mu}_{(0)}$ is the 4-velocity of the star and $\lambda^{\mu}{}_{(i)}$, with $i = \{1, 2, 3\}$,

are three spacelike 4-vectors that are parallel propogated along G. We can then project our tensors from Eq. (1.28) onto this basis as follows,

$$u^{\mu} = \lambda^{\mu}{}_{(0)}, \tag{1.30a}$$

$$X^{\mu} = X^{(i)}\lambda^{\mu}_{(i)}, \tag{1.30b}$$

$$R^{\beta}{}_{\mu\alpha\nu} = R^{(\gamma)}{}_{(\delta)(\kappa)(\xi)}\lambda^{\beta}{}_{(\gamma)}\lambda^{(\delta)}{}_{\mu}\lambda^{(\kappa)}{}_{\alpha}\lambda^{(\xi)}{}_{\nu}, \tag{1.30c}$$

$$C^{\beta}{}_{\alpha} = C^{(i)}{}_{(j)}\lambda^{\beta}{}_{(i)}\lambda^{(j)}{}_{\alpha}. \tag{1.30d}$$

The indices of the tensors can be raised and lowered using the Schwarzschild metric (Eq. (1.22)) for the BL indices and the Lorentz metric $\eta_{(\mu)(\nu)}$ for the FN indices. The geodesic deviation equation then becomes,

$$\frac{d^2X^{(i)}}{d\tau^2} = -C^{(i)}{}_{(j)}X^{(j)}. \tag{1.31}$$

The tidal tensor $C^{(i)}{}_{(j)}$ is a real, symmetric 3×3 tensor and thus has three eigenvectors along the directions that the star is compressed and stretched. The sign convention of Eq. (1.31) means that the negative eigenvalue corresponds to tidal stretching, and setting this eigenvalue equal to the self gravity of the star would allow one to determine the orbital parameters necessary for TDEs to occur under Schwarzschild geometry. Similar arguments would hold under the Kerr metric, but the loss of spherical symmetry makes the problem more computationally difficult to solve.

CHAPTER 2

UNIFIED TREATMENT OF TIDAL DISRUPTION BY SCHWARZSCHILD BLACK HOLES

Authors – Juan Servin and Michael Kesden

The Department of Physics, PHY 36

The University of Texas at Dallas

800 West Campbell Road

Richardson, Texas 75080-3021

Key words: black holes, tidal disruption, astrophysics
Corresponding author: Juan Servin

The work presented in this chapter originally appeared in "Unified treatment of tidal disruption by Schwarzschild black holes", J. Servin and M. Kesden (2017), Physical Review D 95, 083001, © APS. JS performed all calculations and writing for this work in collaboration with MK. JS independently developed the MATLAB code used in the calculations of the TDE rates and the remapping procedure for β. MK provided the expressions for the energy and angular momentum distribution widths. This paper (Servin and Kesden, 2017) was published in PRD (Physical Review D) on April 3rd, 2017.

2.1 Introduction

Supermassive black holes (SBHs) with masses in the range from $10^6 M_\odot \leq M_\bullet \leq 10^{10} M_\odot$ are found at the centers of most large galaxies (Kormendy and Richstone, 1995; Magorrian et al., 1998). Observations of quasars (Schmidt, 1963) and active galactic nuclei (AGN) have aided our understanding of these massive celestial objects, but these constitute only a small fraction (Kauffman et al., 2003) of all SBHs in the local universe, making it difficult to take a fully representative census of galactic nuclei. Studying quiescent SBHs, visible via their interactions with nearby stellar objects through the phenomena of tidal disruption events (TDEs) (Rees, 1988), would allow one to fill in this population gap, particularly for lower mass SBHs. Quiescent SBHs also have dynamical effects on neighboring stars and gas, but these can only be observed locally where the influence radius can be resolved.

TDEs occur when tidal forces due to a SBH's gravitational field overcome an orbiting star's self gravity, causing roughly half of the resulting debris to become more tightly bound to the SBH (Rees, 1988). This bound debris quickly forms a disk that is accreted by the SBH, releasing large amounts of energy in what is known as a tidal flare. Flares can be found in the optical (van Velzen et al., 2011; Gezari et al., 2012; Cenko et al., 2012; Arcavi et al., 2014; Chornock et al., 2014; Holoien et al., 2014; Vinkó et al., 2015), ultraviolet (Stern et al., 2004; Gezari et al., 2006, 2008, 2009), soft X-ray (Bade et al., 1996; Grupe et al.,

1999; Donley et al., 2002; Esquej et al., 2008; Maksym et al., 2010; Saxton et al., 2012), and hard X-ray (Bloom et al., 2011; Burrows et al., 2011; Cenko et al., 2012) bands. A recent survey (Donley et al., 2002) discovered many candidate TDEs, showing rates consistent with those previously predicted by early models, resulting in an increased interest in TDEs in recent years.

Analysis of TDEs has been conducted under both Newtonian gravity (Rees, 1988; Magorrian and Tremaine, 1999; Wang and Merritt, 2004; Merritt, 2013; Cohn and Kulsrud, 1978; Evans and Kochanek, 1989; Lodato et al., 2009) and general relativity (Luminet and Marck, 1985; Laguna et al., 1993; Diener et al., 1997; Ivanov et al., 2003; Ivanov and Chernyakova, 2006; Kesden, 2012; Sądowski et al., 2016). In this paper, we provide a unified, self-consistent treatment of several aspects of the tidal-disruption process that are sensitive to general relativity. We explore how relativity changes the boundaries of the loss cone in phase space that determines TDE rates and the distribution of orbital elements for tidally disrupted stars. We then examine how relativity affects the distributions of the specific energy and angular momentum of the tidal debris and combine these results with recent hydrodynamical simulations to predict the rate at which this debris falls back onto the SBH to fuel a tidal flare (Guillochon and Ramirez-Ruiz, 2013).

We restrict ourselves in this paper to the Schwarzschild spacetime (Schwarzschild, 1916) corresponding to non-spinning SBHs. The spherical symmetry of the Schwarzschild metric implies that only the magnitudes of the orbital energy and angular momentum are needed to define the boundaries of the loss cone. However, in the Kerr spacetime (Kerr, 1963) of spinning SBHs, the orientation of the tidally disrupted star's orbit with respect to the SBH's equatorial plane affects the magnitude of the tidal stresses (Ivanov and Chernyakova, 2006). This creates a higher-dimensional parameter space, the analysis of which is beyond the scope of this paper. We will, however, provide some comments on SBH spin when relevant throughout the paper and lay the foundation for future work that will focus on incorporating spin dependence into our procedure.

The rest of this paper is structured as follows. Sec. 2.2 provides a brief overview of how loss-cone theory is used to calculate TDE rates in Newtonian gravity. Sec. 2.3 details how relativity changes the boundaries of the loss cone, allowing us to compare the TDE rates predicted in Newtonian gravity and general relativity. We then focus on trying to compare individual TDEs in the two gravitational theories, which introduces the somewhat subtle issue of which parameter to hold constant in these comparisons. We introduce a new procedure to map between Newtonian orbits and relativistic geodesics in Sec. 2.4 that allows us to estimate how relativity would modify simulations performed in Newtonian gravity. In Sec. 2.5, we use this mapping and loss-cone theory to predict distributions of physical quantities like the peak fallback accretion rate and amount of apsidal precession that affect observed TDE properties. A summary of our key results, their implications for TDE observations, and our plans to generalize to the Kerr spacetime are provided in Sec. 2.6.

2.2 Newtonian loss-cone theory

We begin by providing a brief summary of Newtonian loss-cone theory (Cohn and Kulsrud, 1978; Magorrian and Tremaine, 1999; Wang and Merritt, 2004; Merritt, 2013). We define the tidal radius as

$$r_t \equiv \left(\frac{M_\bullet}{M_\star}\right)^{1/3} R_\star \tag{2.1}$$

where $M_\bullet$ is the mass of the SBH, $M_\star$ is the mass of the tidally disrupted star, and $R_\star$ is the stellar radius. This definition provides an order-of-magnitude estimate of the distance from the SBH at which tidal disruption occurs. Stars on parabolic orbits with pericenters equal to r_t will have orbital angular momentum

$$L_t \equiv (2GM_\bullet r_t)^{1/2} \ . \tag{2.2}$$

Any star on an orbit with angular momentum $L \lesssim L_t$ will become tidally disrupted once it reaches a distance $r \sim r_t$ from the SBH. We can quantify the threshold for full tidal

disruption by introducing the parameter α to account for stellar structure, allowing us to define

$$r_d \equiv \alpha^2 r_t \ , \tag{2.3a}$$

$$L_d \equiv \alpha L_t \ , \tag{2.3b}$$

where r_d is the radial distance and L_d is the maximum orbital angular momentum at which a star described by parameter α is fully disrupted. Throughout this paper, we use the value $\alpha = 1.9^{-1/2} \simeq 0.725$ consistent with the threshold for full tidal disruption in Guillochon and Ramirez-Ruiz (Guillochon and Ramirez-Ruiz, 2013) for a Solar-type star with polytropic index $\gamma = 4/3$.

The TDE rate thus depends on the rate at which stars are driven onto such orbits, which are said to lie in the loss cone in phase space because the velocity vector lies in a cone about the radial direction. We assume that the stellar distributions in galactic centers are described by isothermal spheres with density profile

$$\rho(r) = \frac{\sigma^2}{2\pi G r^2} \tag{2.4}$$

where σ is the velocity dispersion given by the $M_\bullet - \sigma$ relation (Gebhardt et al., 2000; Ferrarese and Merritt, 2000). This profile is slightly steeper than the $\rho \propto r^{-7/4}$ Bahcall-Wolf equilibrium solution (Bahcall and Wolf, 1976) towards which stellar distributions are expected to relax. Observationally, galaxies can be classified as having either "cored" or "power-law" stellar density profiles (Lauer et al., 2005); isothermal spheres are reasonable approximations for the power-law galaxies that dominate the global TDE rate (Magorrian and Tremaine, 1999; Wang and Merritt, 2004). Recent observations suggest that post-starburst galaxies with even steeper stellar density profiles than isothermal spheres are heavily over-represented among TDE host galaxies (French et al., 2016; Stone and van Velzen, 2016).

We assume that loss-cone orbits are refilled by two-body non-resonant relaxation (Cohn and Kulsrud, 1978; Magorrian and Tremaine, 1999; Wang and Merritt, 2004; Merritt, 2013),

in which case the differential flux F of stars into the loss cone per unit dimensionless specific binding energy $\varepsilon^* \equiv \varepsilon/\sigma^2$, following the approach and notation of Merritt (Merritt, 2013), is given by

$$F(\varepsilon^*) = 4\pi^2 q(\varepsilon^*) L_d^2 \left[\int_0^{y_d} f(\varepsilon^*, y) dy \right] \ . \tag{2.5}$$

Here $q(\varepsilon^*)$ is the orbital period divided by the time a star takes to diffuse across the loss cone, $y \equiv L^2/qL_d^2$ is a dimensionless angular-momentum variable, $y_d \equiv 1/q$, and $f(\varepsilon^*, y)$ is the stellar phase-space density as a function of our dimensionless variables. For the stellar density profile of Eq. (2.4),

$$q(\varepsilon^*) = \frac{32\pi^2}{3\sqrt{2}} \ln\Lambda \left(\frac{M_\star}{M_\bullet}\right) \frac{h(\varepsilon^*)}{\psi^*(r_d) - \varepsilon^*} \left(\frac{r_d}{r_h}\right)^{-2} \tag{2.6}$$

where $\ln\Lambda$ is the Coulomb logarithm (Chandrasekhar, 1943), $\psi^*(r) \equiv -\Phi(r)/\sigma^2$ is the negative dimensionless potential energy (including contributions from both the isothermal stellar density profile and the SBH), $r_h = GM_\bullet/\sigma^2$ is the influence radius (Peebles, 1972), and $h(\varepsilon^*)$ (Eq. (6.78) of Merritt (Merritt, 2013)) is a function derived from the isotropic distribution function consistent with our isothermal stellar density profile $\rho(r)$. We set $\Lambda = 0.4 M_\bullet/M_\odot$, appropriate for stars whose velocity distribution is consistent with the virial theorem (Spitzer and Hart, 1971; Wang and Merritt, 2004).

The ratio q helps provide intuition about how two-body relaxation feeds stars into SBHs. Portions of phase space with $q \ll 1$ are said to belong to the empty loss-cone (ELC) regime because diffusion is not efficient enough to repopulate loss-cone orbits on their dynamical timescale. Conversely, $q \gg 1$ corresponds to the full loss-cone (FLC) regime where diffusion is effective enough to keep orbits in these parts of phase space filled. SBHs with $M_\bullet \gtrsim 10^7\, M_\odot$ have $q \ll 1$ for $\varepsilon^* > 1$ and thus belong primarily to the ELC regime, implying lower TDE rates despite their larger tidal radii (Merritt, 2013). Approximately 30% of TDEs occur in the FLC regime for the galaxy sample considered in Stone and Metzger (Stone and Metzger, 2016), where $\sim 50\%$ result in full rather than partial disruptions.

The integrand in Eq. (2.5) for the isotropic distribution function consistent with the isothermal density profile of Eq. (2.4) is given by

$$f(y) = f(y_d)\left[1 - \frac{2}{\sqrt{y_d}}\sum_{m=1}^{\infty}\frac{e^{-\gamma_m^2/4}}{\gamma_m}\frac{J_0(\gamma_m\sqrt{y})}{J_1(\gamma_m\sqrt{y_d})}\right] \tag{2.7}$$

where J_0 and J_1 are Bessel functions of the first kind and γ_m is defined such that $\gamma_m\sqrt{y_d}$ is the m-th zero of J_0 (Merritt, 2013). The flux of stars into the loss cone is then,

$$F(\varepsilon^*) = 4\pi^2 L_d^2 f(y_d)\xi(q) \tag{2.8}$$

where $\xi(q)$ is defined to be q times the integral in Eq. (2.5) and is well approximated by $\xi(q) \approx q/(q^2+q^4)^{1/4}$. Note that $\xi(q)$ is implicitly dependent on ε^* through Eq. (2.6). The total TDE rate is obtained by integrating over all binding energies,

$$\dot{N} = \int F(\varepsilon^*)\, d\varepsilon^*, \tag{2.9}$$

and depends implicitly on the SBH mass $M_\bullet$.

2.3 Relativistic tidal forces

In Newtonian gravity, the tidal force acting on a fluid element of a star is simply the gravitational force in a frame freely falling with the star's center of mass. In general relativity however, gravity affects particle motion through the curvature of spacetime. In this section, we review how tides arise in general relativity so that we can determine the value of the angular momentum L_d that sets the boundary of the loss cone in this gravitational theory. We restrict our analysis in this paper to the Schwarzschild metric (Schwarzschild, 1916) describing non-spinning SBHs, which in Boyer-Lindquist coordinates (Boyer and Lindquist, 1967) is

$$\begin{aligned} ds^2 = &-\left(1 - \frac{2M_\bullet}{r}\right)dt^2 + \frac{r^2}{r^2 - 2M_\bullet r}dr^2 \\ &+ r^2(d\theta^2 + \sin^2\theta d\phi^2). \end{aligned} \tag{2.10}$$

Massive test particles experiencing no non-gravitational forces travel on timelike geodesics $x^\mu(\tau)$ of this metric, the generalization of straight lines in flat space. We can choose to parameterize these geodesics by the proper time τ. Particles traveling on these geodesics have conserved specific energy E and specific angular momentum L since the Schwarzschild metric is both time independent and spherically symmetric. Note that the specific energy

$$E \equiv -g_{\mu\nu} U^\mu \left(\frac{\partial}{\partial t}\right)^\nu = \left(1 - \frac{2M_\bullet}{r}\right) \frac{dt}{d\tau}\,, \tag{2.11}$$

where

$$U^\mu = \frac{dx^\mu}{d\tau} = \left(\frac{dt}{d\tau}, \frac{dr}{d\tau}, \frac{d\theta}{d\tau}, \frac{d\phi}{d\tau}\right) \tag{2.12}$$

is the 4-velocity, asymptotes to unity for particles at rest far from the SBH since it contains the rest-mass energy. We approximate $E = 1$ for the orbits of tidally disrupted stars because the velocity dispersion σ of their host galaxies is much less than the speed of light. This 4-velocity satisfies the geodesic equation

$$\frac{dU^\mu}{d\tau} + \Gamma^\mu_{\nu\alpha} U^\nu U^\alpha = 0 \tag{2.13}$$

where $\Gamma^\mu_{\nu\alpha}$ are the Christoffel symbols for the Schwarzschild metric. Note the resemblance to Newton's second law $d\mathbf{v}/dt = 0$ for force-free motion for vanishing Christoffel symbols as can be chosen for flat space.

In general relativity, tidal forces arise because of the tendency of parallel geodesics to deviate from each other in the presence of spacetime curvature. If two neighboring particles with 4-velocity U^μ are separated by an infinitesimal spacelike deviation 4-vector X^β, this deviation will evolve with proper time τ according to the geodesic deviation equation

$$\begin{aligned} \frac{d^2 X^\beta}{d\tau^2} &= U^\mu \nabla_\mu (U^\alpha \nabla_\alpha X^\beta) = -R^\beta{}_{\mu\alpha\nu} U^\mu X^\alpha U^\nu \\ &= -C^\beta{}_\alpha X^\alpha \end{aligned} \tag{2.14}$$

where ∇_μ are covariant derivatives, $d/d\tau \equiv U^\alpha \nabla_\alpha$ is the derivative with respect to the proper time, $R^\beta{}_{\mu\alpha\nu}$ is the Riemann curvature tensor, and

$$C^\beta{}_\alpha \equiv R^\beta{}_{\mu\alpha\nu} U^\mu U^\nu \tag{2.15}$$

is the tidal tensor. Although we restrict ourselves to this lowest-order result in this paper, the geodesic deviation equation in both the Newtonian (Brassart and Luminet, 2008) and relativistic (Cheng and Evans, 2013) regimes is corrected by octupole and higher tides at higher order in the deviation vector X^α. In Newtonian gravity, a fluid element is tidally stripped from the surface of a star when the tidal force exerted by the SBH exceeds the force exerted on this fluid element by that star's self gravity. If the escape velocity of the star is not relativistic, we can approximate its self gravity as Newtonian even if general relativity is needed to describe the geodesics of the SBH. In this approximation, the fluid element is tidally stripped when the acceleration due to this self gravity is exceeded by the proper acceleration $d^2X/d\tau^2$ given by the geodesic deviation equation (2.14) (Luminet and Marck, 1983).

We can solve this equation more easily by transforming from the global Boyer-Lindquist coordinates given by Eq. (2.10) to local Fermi normal coordinates $(\tau, X^{(i)})$ valid in a neighborhood of spacetime about the center of mass of the star at an arbitrarily chosen proper time $\tau = 0$ (Manasse and Misner, 1963). These coordinates define an orthonormal tetrad: the star's 4-velocity provides the timelike 4-vector $\lambda^\mu{}_{(0)}$, and three spacelike 4-vectors $\lambda^\mu{}_{(i)}$ are chosen that are parallel transported along the geodesic. Spatial indices that run from 1 to 3 are denoted by Latin indices, unlike Greek indices that run from 0 to 3. All of the

tensors appearing in the geodesic deviation equation can be projected into this basis:

$$U^{\mu} = \lambda^{\mu}{}_{(0)} \tag{2.16a}$$

$$X^{\alpha} = X^{(i)}\lambda^{\alpha}{}_{(i)} \tag{2.16b}$$

$$R^{\beta}{}_{\mu\alpha\nu} = R^{(\gamma)}{}_{(\delta)(\kappa)(\xi)}\lambda^{\beta}{}_{(\gamma)}\lambda_{\mu}{}^{(\delta)}\lambda_{\alpha}{}^{(\kappa)}\lambda_{\nu}{}^{(\xi)} \tag{2.16c}$$

$$C^{\beta}{}_{\alpha} = C^{(i)}{}_{(j)}\lambda^{\beta}{}_{(i)}\lambda_{\alpha}{}^{(j)} = R^{(i)}{}_{(0)(j)(0)}\lambda^{\beta}{}_{(i)}\lambda_{\alpha}{}^{(j)}. \tag{2.16d}$$

The Boyer-Lindquist indices are raised and lowered by the Schwarzschild metric (2.10) while the Fermi normal coordinate indices in brackets are raised and lowered by the Lorentz metric $\eta_{(\mu)(\nu)}$. Note that the symmetry of the Riemann tensor implies that the tidal tensor is symmetric and only has spatial components in Fermi normal coordinates. Inserting Eq. (2.16) into (2.14) yields the geodesic deviation equation in Fermi normal coordinates

$$\frac{d^2X^{(i)}}{d\tau^2} = -C^{(i)}{}_{(j)}X^{(j)}. \tag{2.17}$$

Because $C^{(i)}{}_{(j)}$ is a real, symmetric 3×3 tensor, it has 3 real eigenvalues which in Boyer-Lindquist coordinates are $M_{\bullet}/r^3$, $(1 + 3L^2/r^2)M_{\bullet}/r^3$, and $-2(1 + 3L^2/2r^2)M_{\bullet}/r^3$. The negative sign in Eq. (2.17) implies that the eigenvectors associated with the positive eigenvalues correspond to directions along which the star is compressed, while the eigenvector associated with the negative eigenvalue corresponds to the direction in which the star is stretched. Equating the magnitude of this negative eigenvalue times the stellar radius $R_{\star}$ with the acceleration $2M_{\star}/(\alpha^3 R_{\star})^2$ due to the star's self gravity yields

$$\left(1 + \frac{3L^2}{2r^2}\right)\frac{2M_{\bullet}R_{\star}}{r^3} = \frac{2M_{\star}}{(\alpha^3 R_{\star})^2}. \tag{2.18}$$

Combining this result with the relation

$$L^2 = \frac{2M_{\bullet}r^2}{r - 2M_{\bullet}}, \tag{2.19}$$

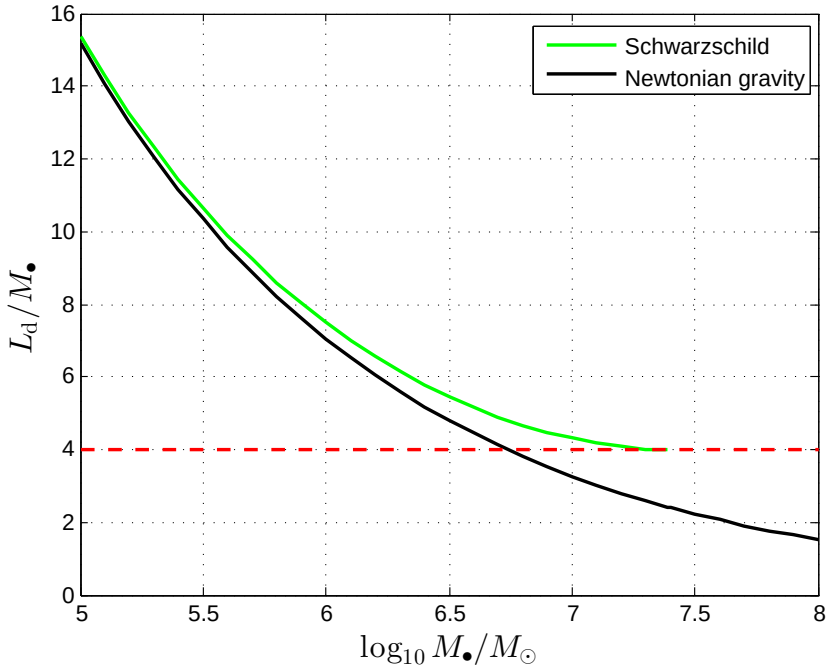

Figure 2.1: The angular-momentum threshold L_d for tidal disruption as a function of SBH mass $M_\bullet$ in both Newtonian gravity (solid black) and general relativity (solid green). As the mass of the SBH increases, L_d falls less steeply in relativity than in Newtonian gravity because of the stronger tidal forces. The horizontal red dashed line at $L_{\rm cap} = 4M_\bullet$ indicates that direct capture by the event horizon occurs below this value, implying that SBHs with $M_\bullet > M_{\rm max} \simeq 10^{7.39} M_\odot$ cannot fully disrupt Solar-type stars.

between the orbital angular momentum L and Boyer-Lindquist coordinate r at pericenter provides two equations that can be solved for the the relativistic tidal radius r_d and angular-momentum threshold L_d for tidal disruption. Note that in the limit $r \gg 2M_\bullet$ these reduce to the Newtonian expressions of Eqs. (2.2) and (2.3).

Fig. 2.1 shows how the angular-momentum threshold L_d depends on SBH mass $M_\bullet$ in both Newtonian gravity and general relativity. All orbits with angular momentum L below this threshold are considered to be inside the loss cone. The Newtonian tidal radius $r_t \propto M_\bullet^{1/3}$ according to Eq. (2.1), while the gravitational radius $r_g \equiv GM_\bullet/c^2$ scales linearly with SBH mass. This implies that relativistic effects become negligible for small SBH masses and the two curves in Fig. 2.1 converge towards the left edge of the plot. The fact that the term

in brackets on the left-hand side of Eq. (2.18) is greater than unity implies that tidal forces are stronger in general relativity than in Newtonian gravity for orbits with the same angular momentum. This explains why the relativistic curve in Fig. 2.1 is above the Newtonian curve; stronger tides allow the SBH to disrupt stars at larger angular momentum L_d in relativity. This result of stronger tides in relativity is confirmed by comparisons between numerical simulations of tidal disruption in Newtonian gravity and Schwarzschild spacetimes (Cheng and Bogdanović, 2014).

Relativity also introduces the phenomena of stellar capture; stars on orbits with angular momentum less than $L_{\rm cap} = 4M_\bullet$ will plunge directly into the event horizon leaving no debris to emit photons and generate an observable TDE. This angular-momentum threshold for direct capture, shown by the horizontal red dashed line in Fig. 2.1, grows linearly with SBH mass and eventually exceeds the threshold L_d for tidal disruption at $M_\bullet = M_{\rm max} \simeq 10^{7.39} M_\odot$. This limit is proportional to α^3, where α is the parameter defined in Eq. (2.3) to account for the dependence of the tidal radius on stellar structure. Kesden (Kesden, 2012) implicitly used the value $\alpha = 2^{1/6} \simeq 1.12$ compared to the choice $\alpha = 0.725$ used in this paper, leading to a higher threshold $M_{\rm max} \simeq (1.12/0.725)^3 \times 10^{7.39} M_\odot = 10^{7.96} M_\odot$. SBHs with masses above this value, shown by the intersection of the solid green and dashed red curves in Fig. 2.1, cannot produce observable full TDEs.

Fig. 2.2 shows the rates of observable TDEs (both full and partial) and direct stellar capture predicted when two-body relaxation is responsible for refilling the loss cone as described in Sec. 2.2. Although $\alpha \simeq 0.725$ sets the threshold $L_d = \alpha L_t$ for full tidal disruption, hydrodynamical simulations (Guillochon and Ramirez-Ruiz, 2013) indicate that Solar-type stars with polytropic index $\gamma = 4/3$ can be partially disrupted on orbits with $L \leq L_{pd} = \alpha_{pd} L_t$, where $\alpha_{pd} = 0.6^{-1/2} \simeq 1.29$. Eq. (2.9) gives the rate of full TDEs, while the rate of partial TDEs is determined by summing the contributions from orbits with $L_d \leq L \leq L_{pd}$ as described in greater detail in Sec. 2.5. Relativity modifies these Newtonian predictions in two

ways. It changes the the thresholds r_d and L_d in Eqs. (2.6) and (2.7) to the maximum of the thresholds set by full disruption and direct capture, and modifies the limits of the integral in Eq. (2.5) to account for the three outcomes of partial disruption, full disruption, and direct capture. For SBH masses $M_\bullet < M_{\rm max}$, $L_{\rm cap} < L_d < L_{pd}$ and so the integral must be decomposed into three contributions: (1) an integral from 0 to $y_{\rm cap}$ giving the capture rate, (2) an integral from $y_{\rm cap}$ to y_d giving the full TDE rate, and (3) an integral from y_d to y_{pd} giving the partial TDE rate. As $M_\bullet$ increases above $M_{\rm max}$, $L_{\rm cap} \geq L_d$ implying that contribution (2) above vanishes and only partial TDEs are observable. For $M_\bullet \geq M_{\rm max,pd} \simeq 10^{8.15} M_\odot$, $L_{\rm cap} \geq L_{pd}$ and there are no observable TDEs (a single integral from 0 to $y_{\rm cap}$ gives the capture rate).

The TDE rates shown in Fig. 2.2 are sensitive to the choice of stellar density profile (Magorrian and Tremaine, 1999; Wang and Merritt, 2004). Steeper inner power-law slopes yield higher TDE rates, and core galaxies have a higher fraction of TDEs in the full loss-cone regime at fixed SBH mass (Stone and Metzger, 2016). Exploring the degeneracy in the TDE rate between relativistic effects and choice of stellar density profile of the host galaxy would be a valuable project but is beyond the scope of this paper.

2.4 Comparing tidal disruption in Newtonian gravity and general relativity

Having introduced tidal disruption in Newtonian gravity and general relativity in Secs. 2.2 and 2.3, we now seek to compare the predictions of the two theories. This point is more subtle than it might initially appear, as there is no unique way to map Keplerian orbits in Newtonian gravity to geodesics of the Schwarzschild metric in general relativity. In the limit that the pericenter $r \to \infty$, it is natural to map a geodesic to its identical Keplerian counterpart, but this limiting behavior is insufficient to fully specify the mapping. The appropriate mapping to use depends on the nature of the problem one is trying to solve. We

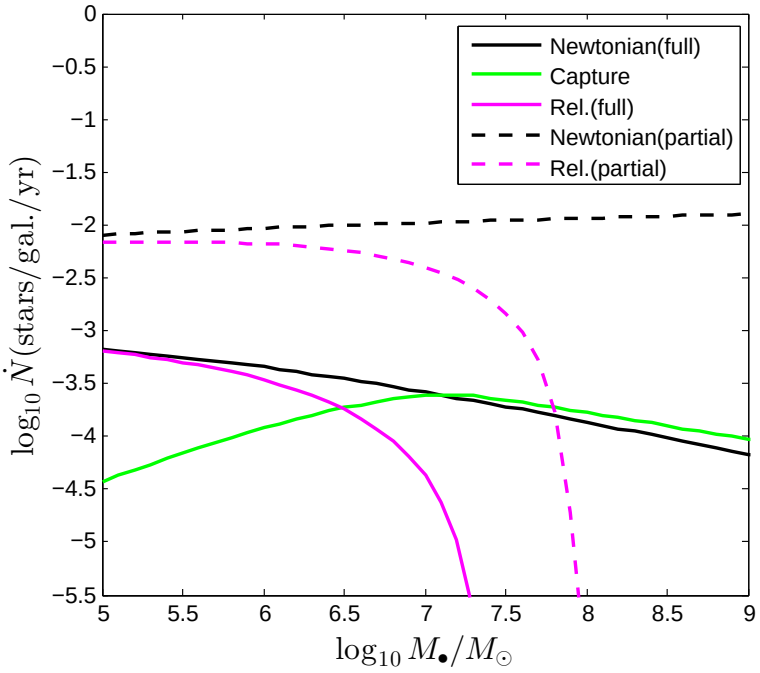

Figure 2.2: TDE rates in Newtonian gravity and general relativity as functions of SBH mass $M_\bullet$. The solid (dashed) black curve shows the TDE rate in Newtonian gravity for fully (partially) disrupted stars. In relativity, observable TDEs occur when tides are strong enough to disrupt the star and the debris has enough angular momentum to avoid direct capture by the SBH's event horizon. The rate of such observable TDEs is given by the solid (dashed) magenta curve for fully (partially) disrupted stars, while the capture rate is shown by the solid green curve. Stronger tides in relativity slightly increase this total rate, but capture reduces the full TDE rate in relativity below that of Newtonian gravity.

consider in this section three distinct mappings that all possess the desired behavior in the Newtonian limit; these three mappings identify:

(1) orbits with equal pericenter coordinates r,

(2) orbits with equal angular momenta L,

(3) orbits on which a star experiences equal tidal forces at pericenter.

Mapping (1) is perhaps the most obvious choice and was used for the corrections to the orbital constants provided in Kesden (Kesden, 2012). However, according to the Schwarzschild

metric in Boyer-Lindquist coordinates given in Eq. (2.10), the physical significance of this mapping is that it identifies parabolic orbits such that the circular orbits in the two gravitational theories with the same pericenter r would have the same circumference $2\pi r$. It is unclear why this choice of mapping would be particularly useful for analyzing the tidal disruption of stars on non-circular orbits.

Mapping (2) identifies orbits in the two theories with the same values of the gauge-invariant orbital angular momentum, defined for the Schwarzschild metric as

$$L \equiv g_{\mu\nu} U^{\mu} \left(\frac{\partial}{\partial \phi} \right)^{\nu} = r^2 \frac{d\phi}{d\tau} \tag{2.20}$$

for equatorial orbits ($\theta = \pi/2$). This mapping seems like a useful choice, as TDE properties do depend on the orbital angular momentum as seen in the recent simulations of Guillochon and Ramirez-Ruiz (Guillochon and Ramirez-Ruiz, 2013). However, tides are stronger on Schwarzschild geodesics than on Keplerian orbits with the same value of L as established in Sec. 2.3, so it seems unlikely that TDEs on orbits in the two theories identified in this manner would have the same properties.

We conjecture that TDEs resulting from stars initially on orbits identified by mapping (3) will have similar properties because the stars were subjected to similar tidal forces. This conjecture is supported by the "freezing" model of Lodato, King, and Pringle (Lodato et al., 2009) which proposed that the orbital energy distribution of tidal debris is frozen in following an instantaneous tidal disruption of an unperturbed star. This model was used with reasonable success to describe the light curve of the TDE PS1-10jh (Gezari et al., 2012). We will use this freezing assumption later in Sec. 2.5 to determine the appropriate relativistic correction to the energy distribution, but we will apply the correction at the disruption radius r_d rather than pericenter. This is consistent with the analytic model of Stone, Sari, and Loeb (Stone et al., 2013) and some hydrodynamical simulations of TDEs (Hayasaki et al., 2013; Guillochon and Ramirez-Ruiz, 2013) which showed that the spread in

debris energy was largely independent of the orbital angular momentum L for full disrupted stars.

To implement mapping (3), we must find the angular momentum L_N of the orbit in Newtonian gravity that has the same peak tidal force as that experienced by a star on a Schwarzschild geodesic with angular momentum L and pericenter r. We accomplish this by setting the magnitude of the negative eigenvalue of the tidal tensor $C^{(i)}{}_{(j)}$ equal to its Newtonian limit for an orbit with angular momentum L_N:

$$\left(1+\frac{3L^2}{2r^2}\right)\frac{1}{r^3}=\left(\frac{2M_\bullet}{L_N^2}\right)^3. \tag{2.21}$$

This equation, combined with Eq. (2.19) relating the angular momentum L to the pericenter r in Boyer-Lindquist coordinates, can be solved to determine $L_N(L)$ for mapping (3).

Instead of using the angular momentum L to identify orbits, the TDE literature often uses the penetration factor

$$\beta\equiv\frac{L_t^2}{L^2}, \tag{2.22}$$

where L_t is defined in Eq. (2.2). This choice is convenient because stars on orbits with $\beta\geq\beta_d\equiv L_t^2/L_d^2$ are tidally disrupted, where β_d is of order unity. Our mapping $L_N(L)$ implies an equivalent mapping $\beta_N(\beta)$, where

$$\beta_N\equiv\frac{L_t^2}{L_N^2}=\left(\frac{r+M_\bullet}{r-2M_\bullet}\right)^{1/3}\frac{r_t}{r} \tag{2.23}$$

and r is an implicit function of L and hence β through Eq. (2.19). We show this mapping for several values of the SBH mass $M_\bullet$ in Fig. 2.3. These mappings are undefined for $\beta>\beta_{\rm cap}\equiv L_t^2/L_{\rm cap}^2$ since such geodesics plunge directly into the event horizon and therefore do not have pericenters at which one can calculate the tidal force. The mappings $\beta_N(\beta)$ are above the diagonal and have positive curvature because tides are stronger in general relativity, requiring Newtonian orbits to have deeper penetration factors β_N to match the tides on Schwarzschild geodesics at pericenter. The mapping for SBH mass $M_{\rm max}\simeq10^{7.39}M_\odot$

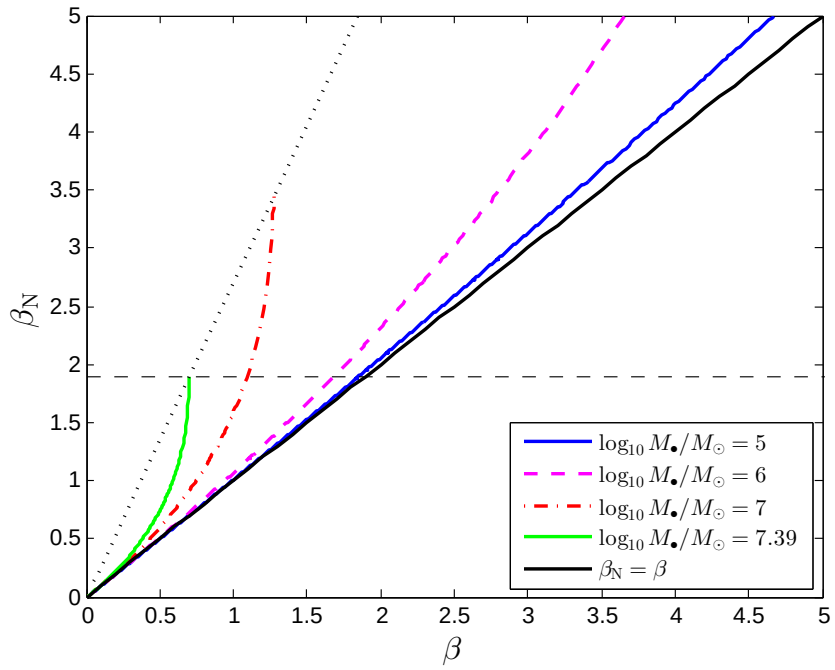

Figure 2.3: The mapping between Schwarzschild geodesics with penetration factor β and orbits in Newtonian gravity with penetration factor β_N on which stars experience the same tidal forces at pericenter. The solid blue, dashed magenta, dot-dashed red, and solid green curves show this mapping for SBHs with masses $M_\bullet/M_\odot$ of 10^5, 10^6, 10^7, and $10^{7.39}$, respectively. The solid black diagonal $\beta_N = \beta$ shows the limit of these curves as $M_\bullet \to 0$, while the dotted black curve shows the relation $\beta_N(\beta_{\rm cap})$ beyond which these mappings are undefined. The horizontal black dashed line $\beta_{N,d} = 1.9$ corresponds to full disruption in the hydrodynamical simulations of Guillochon and Ramirez-Ruiz (Guillochon and Ramirez-Ruiz, 2013).

terminates at $\beta_N(\beta_{\rm cap}) = \beta_{N,d} = 1.9$, precisely the threshold for the full disruption of Solar-type stars (Guillochon and Ramirez-Ruiz, 2013) seen in Fig. 2.1 for $L_d = L_{\rm cap}$.

To further illustrate how relativity affects the minimum penetration factor β_d for tidal disruption, we show its dependence on SBH mass $M_\bullet$ in Fig. 2.4 for both full and partial tidal disruptions. Newtonian hydrodynamical simulations (Guillochon and Ramirez-Ruiz, 2013) indicate that Solar-type stars are fully disrupted for $\beta_N > \beta_{N,d} = 1.9$, while partial disruptions occur for $\beta_N > \beta_{N,pd} = 0.6$. As $M_\bullet$ increases and β_d approaches $\beta_{\rm cap}$, the β_d curves fall increasingly below these Newtonian thresholds because of the stronger tides in

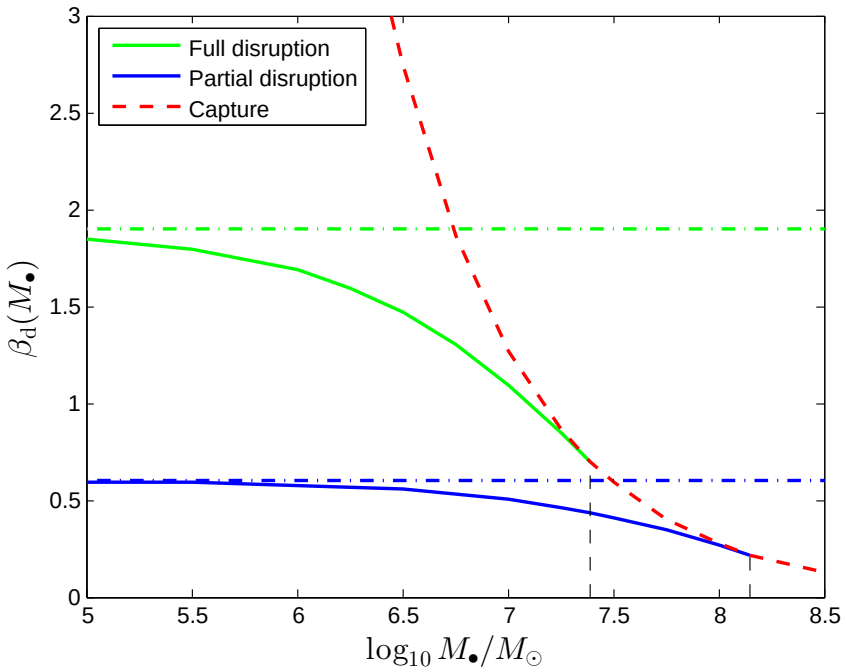

Figure 2.4: The minimum penetration factors β_d and β_{pd} for full and partial tidal disruption in general relativity as functions of SBH mass $M_\bullet$. The horizontal dot-dashed green and blue lines show the thresholds $\beta_{N,d} = 1.9$ and $\beta_{N,pd} = 0.6$ for full and partial disruption in Newtonian gravity (Guillochon and Ramirez-Ruiz, 2013). The solid green and blue curves show the values of β_d for Schwarzschild geodesics on which stars experience the same tidal forces at pericenter. The intersections between these curves and the dashed red curve $\beta_{\rm cap}(M_\bullet)$, marked by the vertical dashed lines, occur at the maximum SBH masses $M_{\rm max,FD} \simeq 10^{7.39} M_\odot$ and $M_{\rm max,PD} \simeq 10^{8.15} M_\odot$ capable of full and partial tidal disruption.

general relativity. The values of $M_\bullet$ at which these curves intersect the $\beta_{\rm cap}$ curve are the maximum masses $M_{\rm max,FD} \simeq 10^{7.39} M_\odot$ and $M_{\rm max,PD} \simeq 10^{8.15} M_\odot$ capable of full and partial tidal disruption. These limits are consistent with recent work suggesting that observable TDEs by SBHs with masses above $10^8 M_\odot$ result exclusively from giant stars (MacLeod et al., 2012). Determinations of $M_{\rm max}$ that failed to account for the stronger relativistic tides, effectively using mapping (2) $\beta_d = \beta_{N,d}$ shown by the horizontal lines in Fig. 2.4, would underestimate $M_{\rm max}$ by a factor of ~ 4.5 for both full and partial disruptions. Future work will explore how SBH spin can push $M_{\rm max}$ to even higher values for stars on prograde orbits.

2.5 Distributions of relativistic TDE properties

In this section, we use concepts developed earlier in the paper to predict distributions of several quantities that may affect the observed properties of TDEs. These properties include the peak accretion rate $\dot{M}_{\rm peak}$ at which tidal debris falls back onto the SBH, the time delay $t_{\rm peak}$ between tidal disruption and when this peak fallback accretion occurs, a parameter f_L measuring the vulnerability of the tidal debris to direct capture by the event horizon of the SBH, and the pericenter precession $\Delta\omega$ of the disrupted star. The peak accretion rate $\dot{M}_{\rm peak}$ may be proportional to the peak bolometric luminosity if accretion remains below the Eddington rate (Lodato et al., 2009). The time delay $t_{\rm peak}$ could in principle be measured if in addition to the peak of the TDE light curve one could also observe a prompt electromagnetic signature associated with disruption like an X-ray shock breakout (Kobayashi et al., 2004; Guillochon et al., 2009). The direct capture of tidal debris, occurring for $f_L < 0$, could suppress emission responsible for the early portion of the TDE light curve (Kesden, 2012). Relativistic pericenter precession has been shown in theoretical work to affect the time needed to circularize the orbits of the tidal debris and produce emission from the newly formed disk (Hayasaki et al., 2013; Dai et al., 2013; Guillochon et al., 2014; Guillochon and Ramirez-Ruiz, 2015; Shiokawa et al., 2015).

Guillochon and Ramirez-Ruiz (Guillochon and Ramirez-Ruiz, 2013) performed Newtonian hydrodynamical simulations to determine the peak fallback accretion rate $\dot{M}_{\rm peak}$ and time delay $t_{\rm peak}$. They then provided analytic fits to these quantities as functions of the Newtonian penetration factor β_N. Under the approximation that these quantities depend only on the peak tidal forces along each orbit, we use the inverse of the mapping $\beta_N(\beta)$ shown in Fig. 2.3 to derive fits to $\dot{M}_{\rm peak}$ and $t_{\rm peak}$ as functions of the relativistic penetration factor β in the Schwarzschild spacetime. We then use the loss-cone theory discussed in Sec. 2.2, modified by the relativistic corrections to the boundaries of the loss cone shown in Fig. 2.1, to predict the distributions of these quantities for different SBH masses.

In Subsec. 2.5.1, we determine the differential TDE rate $d\dot{N}/d\beta$ per unit relativistic penetration factor β. In Subsec. 2.5.2, we use this rate and our corrected fits $\dot{M}_{\rm peak}(\beta)$ and $t_{\rm peak}(\beta)$ to derive initial estimates for the differential TDE rates $d\dot{N}/d\dot{M}_{\rm peak}$ and $d\dot{N}/dt_{\rm peak}$ per unit peak fallback accretion rate and time delay, respectively. These initial estimates do not account for an additional relativistic effect discussed in Kesden (Kesden, 2012), that the gradient of the potential well that determines the width of debris energy distribution differs in general relativity and Newtonian gravity. We review this result and then derive revised estimates for $d\dot{N}/d\dot{M}_{\rm peak}$ and $d\dot{N}/dt_{\rm peak}$ in Subsec. 2.5.3. The stellar debris produced following tidal disruption will also have a distribution of orbital angular momentum, but this often receives less attention in Newtonian gravity where the orbital periods that determine the fallback accretion rate depend on energy but not angular momentum. However, the distribution of orbital angular momentum can be very important when considering highly relativistic TDEs for which much of the debris can lose enough specific angular momentum to fall below the threshold for capture $L_{\rm cap}$ even if the initial star was above this threshold. We discuss this regime in Subsec. 2.5.4 and show that this effect sharply limits the relativistic correction to the peak fallback accretion rate. Finally, in Subsec. 2.5.5 we use our relativistically corrected loss-cone theory to determine the differential TDE rate $d\dot{N}/d\Delta\omega$ per unit relativistic shift in argument of pericenter, an important effect responsible for tidal stream crossings and the prompt circularization of debris (Hayasaki et al., 2013; Dai et al., 2013; Guillochon et al., 2014; Guillochon and Ramirez-Ruiz, 2015; Shiokawa et al., 2015).

2.5.1 Distribution of penetration factor β

We begin by calculating the differential TDE rate $d\dot{N}/d\beta$ in Newtonian gravity. The angular-momentum variable y can be expressed in terms of the penetration factor β as

$$y = \frac{L_t^2}{qL_d^2\beta} \ . \tag{2.24}$$

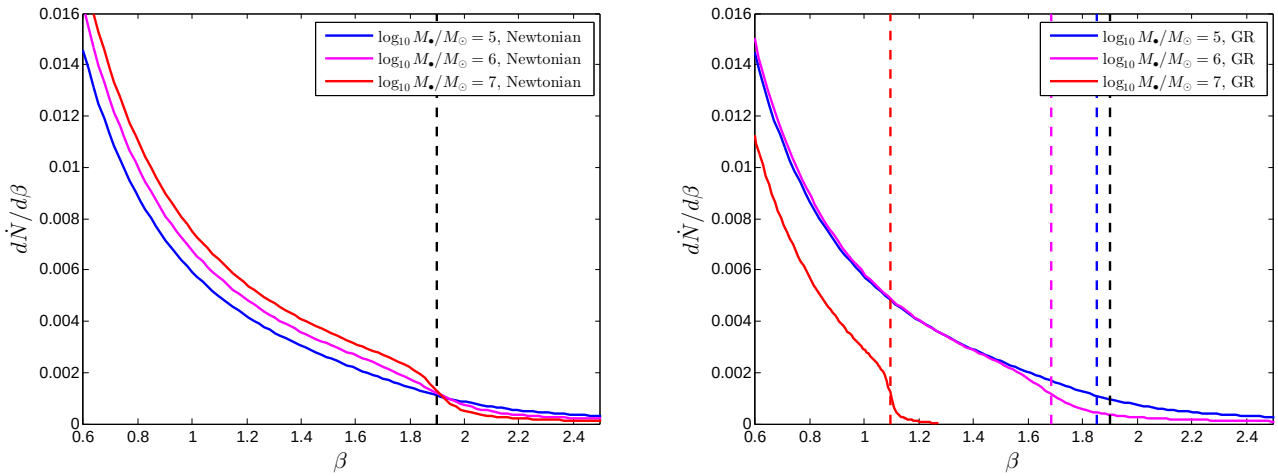

Figure 2.5: The differential TDE rate $d\dot{N}/d\beta$ per unit penetration factor for various SBH masses under Newtonian gravity (left) and relativity (right). The dashed black line in both panels shows the Newtonian threshold $\beta_{N,d} = 1.9$ for full disruption, while the blue, magenta, and red dashed lines in the right panel show the thresholds β_d in relativity defined through the the mapping $\beta_N(\beta_d) = \beta_{N,d}$ between Newtonian orbits and Schwarzschild geodesics with the same tidal forces at pericenter.

This relation allows us to differentiate Eq. (2.5) with respect to β, which when combined with the distribution function in Eq. (2.7) yields,

$$\frac{dF}{d\beta} = \left(\frac{2\pi L_t}{\beta}\right)^2 f(y_d) \times \left[1 - 2\sqrt{q}\sum_{m=1}^{\infty} \frac{e^{-\gamma_m^2/4}}{\gamma_m} \frac{J_0(\gamma_m L_t/L_d\sqrt{q\beta})}{J_1(\gamma_m/\sqrt{q})}\right] . \quad (2.25)$$

Integrating this expression with respect to the dimensionless specific binding energy ε^* gives us the Newtonian differential TDE rate $d\dot{N}/d\beta$ shown in the left panel of Fig. 2.5 above. The total TDE rate is the area under this curve for $\beta_N > \beta_{N,d}$ which decreases with increasing SBH mass $M_\bullet$ consistent with the TDE rates seen in Fig. 2.2. The blue curve in the left panel of Fig. 2.5 extends smoothly beyond $\beta_{N,d}$ because much of the phase space beyond this value is still in the full loss-cone regime $q \gg 1$ for which $d\dot{N}/d\beta \propto \beta^{-1}$ (Stone and Metzger, 2016). However, as $M_\bullet$ increases towards $10^7 M_\odot$, the differential TDE rate becomes exponentially

suppressed for $\beta_N > \beta_{N,d}$ reflecting that much of the phase space beyond this point now lies in the empty loss-cone regime (Stone and Metzger, 2016).

Relativity introduces two changes into the calculation of the differential TDE rate $d\dot{N}/d\beta$: (1) the stronger tides increase the numerical value of L_d from the Newtonian result given by the black curve in Fig. 2.1 to the relativistic result given by the green curve in this figure, and (2) capture by the event horizon cause the differential rate to fall discontinuously to zero for $\beta \geq \beta_{\rm cap}$. As most stars diffusing into the loss cone have apocenters near the influence radius $r_h = GM_\bullet/\sigma^2 \gg r_g = GM_\bullet/c^2$ (Frank and Rees, 1976), the Newtonian treatment of stellar diffusion encapsulated in the ratio q remains an accurate approximation. Both of the changes listed above leave signatures in the relativistic differential TDE rate $d\dot{N}/d\beta$ seen in the right panel of Fig. 2.5. The bends in these curves marking the threshold for full disruption in the empty loss-cone regime migrate to lower values of β consistent with the SBH mass dependence of the mapping $\beta_N(\beta)$ shown in Fig. 2.3. The curves also end abruptly at $\beta_{\rm cap}$ as can be seen in the red curve corresponding to SBH mass $M_\bullet = 10^7 M_\odot$ for which $\beta_{\rm cap} \simeq 1.27$. Integrating the curves in Fig. 2.5 within the appropriate β ranges ($0.6 < \beta_N < 1.9$ for partial disruptions and $1.9 < \beta_N < \beta_{\rm cap}$ for full disruptions) would reproduce the full and partial TDE rates shown in Fig. 2.2.

2.5.2 Distributions of peak fallback accretion rate $\dot{M}_{\rm peak}$ and time delay $t_{\rm peak}$

Guillochon and Ramirez-Ruiz (Guillochon and Ramirez-Ruiz, 2013) performed a series of Newtonian hydrodynamical simulations at different penetration factors β_N and used them to derive analytic fits to the peak fallback accretion rate $d\dot{M}_{\rm peak}/dt$ and time delay $t_{\rm peak}$ for Solar-type stars with polytropic index $\gamma = 4/3$:

$$\dot{M}_{\rm peak} = A_{4/3} \left(\frac{M_\bullet}{10^6 M_\odot} \right)^{-1/2}, \tag{2.26a}$$

$$t_{\rm peak} = B_{4/3} \left(\frac{M_\bullet}{10^6 M_\odot} \right)^{1/2}, \tag{2.26b}$$

where,

$$A_{4/3} = \exp\left(\frac{27.3 - 27.5\beta_N + 3.87\beta_N^2}{1 - 3.26\beta_N - 1.39\beta_N^2}\right), \tag{2.27a}$$

$$B_{4/3} = \frac{-0.387 + 0.573\sqrt{\beta_N} - 0.312\beta_N}{1 - 1.27\sqrt{\beta_N} - 0.9\beta_N}, \tag{2.27b}$$

and $0.6 \leq \beta_N \leq 4.0$. Given these fits, the mapping $\beta_N(\beta)$ derived in Sec. 2.4, and the differential TDE rate $d\dot{N}/d\beta$ obtained in the previous subsection, we can calculate differential rates

$$\frac{d\dot{N}}{dX} = \frac{d\dot{N}}{d\beta}\left(\frac{d\beta_N}{d\beta}\frac{dX}{d\beta_N}\right)^{-1} \tag{2.28}$$

for $X \in \{\dot{M}_{\rm peak}, t_{\rm peak}\}$.

We show these differential TDE rates in Fig. 2.6 above. A complication arises from the fact that the dependence on penetration factor in Eq. (2.27) is not monotonic; $\dot{M}_{\rm peak}$ ($t_{\rm peak}$) increases (decreases) with β_N until the threshold for full disruption $\beta_{N,d}$ is reached, then decreases (increases) for TDEs that penetrate more deeply into the SBH's potential well. This β_N dependence contradicts the naive predictions of freezing models which assume that the energy distribution of the tidal debris is frozen in at the disruption radius r_d, but does not fatally compromise our analyis. We address this complication by plotting the TDEs from partial ($\beta_N < \beta_{N,d}$) and full ($\beta_N > \beta_{N,d}$) disruptions separately in the left and right panels of Fig. 2.6. The differential rates diverge at the extremum $\beta_N = \beta_{N,d}$ shown by the vertical black dashed lines in these plots, but the total rates (areas under the curves) remain finite. We see that the stronger tides of relativity suppress the rates of both full and partial TDEs, particularly for SBH masses $M_\bullet \geq 10^7 M_\odot$ for which portions of phase space with $\beta_N > \beta_{N,d}$ lie primarily in the empty loss-cone regime. This emptiness even reduces the rate of partial TDEs because of the sharper gradients driving stronger diffusion across the boundary as seen by the dip near the threshold in the top left panel of Fig. 2.6. More quantitatively, for a $10^7 M_\odot$ SBH, relativity increases the mean value of the (scaled) peak

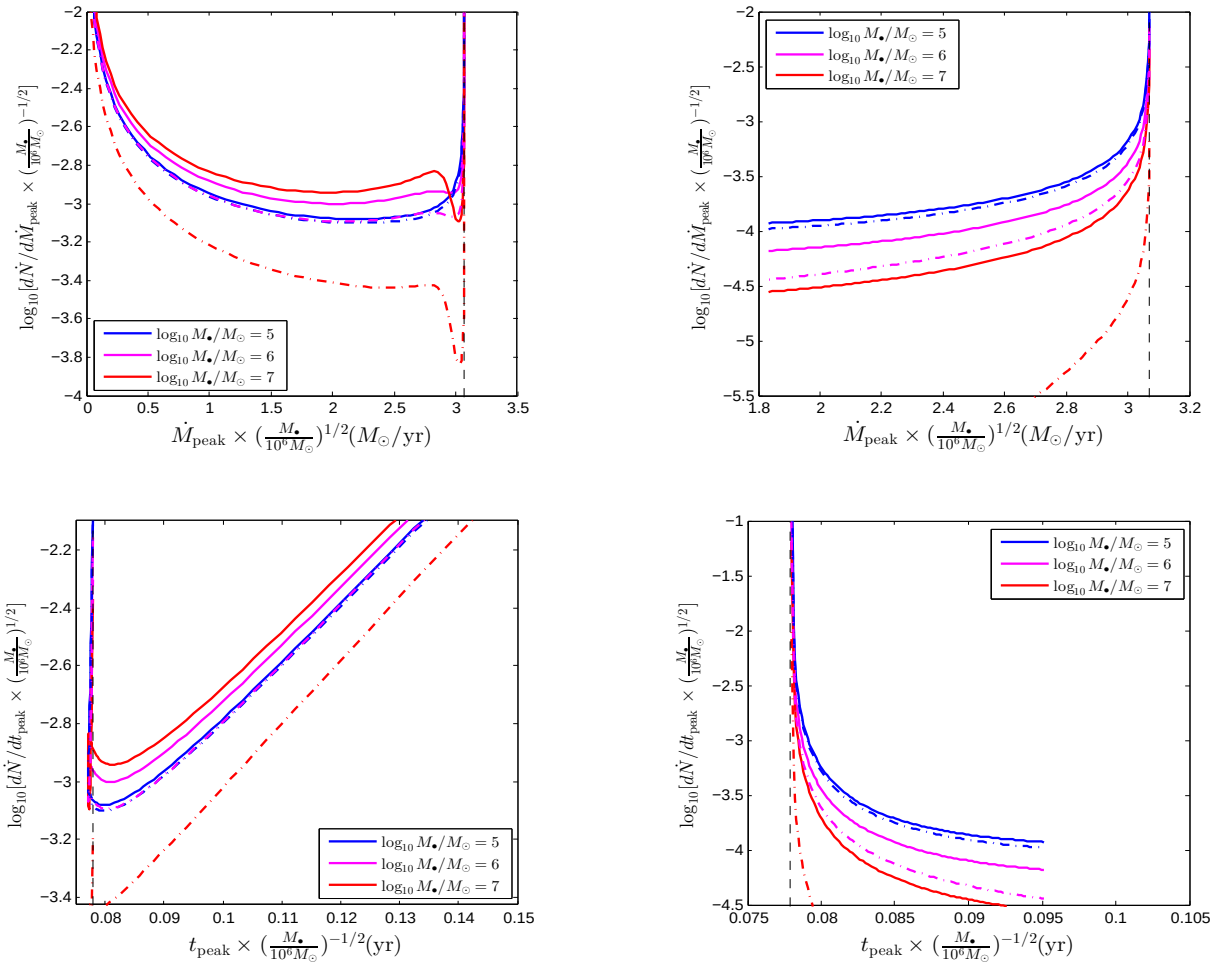

Figure 2.6: The differential TDE rates $d\dot{N}/d\dot{M}_{\rm peak}$ (top panels) and $d\dot{N}/dt_{\rm peak}$ (bottom panels) as functions of the peak fallback accretion rate $\dot{M}_{\rm peak}$ and time delay $t_{\rm peak}$ for partial (left panels) and full (right panels) disruptions. To clarify the presentation of relativistic effects, we have scaled out the explicit dependence on SBH mass $M_\bullet$ given on the right-hand side of Eq. (2.26). The solid (dot-dashed) curves show the differential TDE rates in Newtonian gravity (general relativity). The vertical dashed black lines indicate the values of $\dot{M}_{\rm peak}$ and time delay $t_{\rm peak}$ and the threshold $\beta_{N,d} = 1.9$ of full disrpution.

accretion rate $\dot{M}_{\rm peak}$ for full TDEs to $2.965\,M_\odot/{\rm yr}$ from its Newtonian value of $2.757\,M_\odot/{\rm yr}$ and decreases the mean value of the (scaled) time delay $t_{\rm peak}$ to 0.078 yr from its Newtonian value of 0.0792 yr. These changes occur because direct capture by the SBH event horizon prevents stars on deeply penetrating orbits from producing observable TDEs, and simulations

(Guillochon and Ramirez-Ruiz, 2013) show that such deeply penetrating TDEs yield lower peak accretion and longer delays.

2.5.3 Relativistic correction to the debris energy distribution

The estimated differential TDE rates $d\dot{N}/d\dot{M}_{\rm peak}$ and $d\dot{N}/dt_{\rm peak}$ in the previous subsection accounted for relativistic corrections to the boundaries of the loss cone, but in the interest of a systematic exploration of relativistic effects we did not simulataneously include relativistic corrections to the energy distribution of the tidal debris. We turn our attention to this effect in this subsection.

A key approximation often used in the analysis of TDEs is that the tidal debris travels on ballistic trajectories following disruption, and that orbit circularization followed by viscous accretion occurs promptly after the bound debris falls back to pericenter (Rees, 1988; Evans and Kochanek, 1989; Kochanek, 1994). The fallback accretion rate onto the SBH, and thus its peak value $\dot{M}_{\rm peak}$ and the time $t_{\rm peak}$ between disruption and when this peak occurs, is determined by the distribution of orbital periods of the tidal debris, which is in turn set by the energy distribution through Kepler's third law

$$\tau = 2\pi \left(\frac{a^3}{M_\bullet}\right)^{1/2} = 2\pi M_\bullet (2E)^{-3/2}\,. \tag{2.29}$$

This Newtonian relation remains an excellent approximation even for relativistic TDEs, because most of the debris is on highly eccentric orbits prior to circularization and spends most of its time near apocenter where Eq. (2.29) holds. However, if the tidal disruption itself occurs near pericenter where relativistic effects are strongest, Newtonian predictions for the specific binding energy E entering into Eq. (2.29) may not be accurate. TDE simulations in general relativity (Hayasaki et al., 2013; Cheng and Bogdanović, 2014; Bonnerot et al., 2016; Shiokawa et al., 2015; Cheng and Evans, 2013) naturally yield proper relativistic energy distributions, but our goal in this section is to study how relativistic corrections might alter the predictions of Newtonian simulations.

We addressed this issue in Kesden (Kesden, 2012), where we found that for an undistorted star of radius $R_\star$, the width of the potential-energy distribution before disruption and thus the width of the debris energy distribution after disruption is given in general relativity by the expression

$$\sigma_{E,\mathrm{GR}} = |\lambda^{\alpha}{}_{(i)} \nabla_\alpha E| R_\star = |g_{\beta\gamma} \lambda^{\beta}{}_{(0)} \lambda^{\alpha}{}_{(i)} \Gamma^{\gamma}_{\alpha t}| R_\star, \tag{2.30}$$

where $g_{\beta\gamma}$ is the metric tensor, $\Gamma^{\gamma}_{\alpha t}$ are the Christoffel symbols, and $\lambda^{\beta}{}_{(0)}$ and $\lambda^{\alpha}{}_{(i)}$ are the orthonormal tetrad of basis 4-vectors determined by our choice of Fermi normal coordinates in Sec 2.3. For $\beta < \beta_d$ corresponding to partial disruptions, tidal debris is assumed to be liberated at pericenter where the tidal forces are strongest. Evaluating Eq. (2.30) at pericenter for such orbits yields

$$\begin{aligned} \sigma_{E,\mathrm{GR,PD}} &= \frac{M_\bullet R_\star}{r^2} \left(1 - \frac{2M_\bullet}{r}\right)^{-1/2} \\ &= E_t \left(\frac{r_t}{r}\right)^2 \left(1 - \frac{2M_\bullet}{r}\right)^{-1/2}. \end{aligned} \tag{2.31}$$

The pericenter r in Boyer-Lindquist coordinates can be expressed in terms of the angular momentum L using Eq. (2.19),

$$E_t \equiv \frac{M_\bullet R_\star}{r_t^2} = \left(\frac{M_\bullet}{M_\star}\right)^{1/3} \frac{M_\star}{R_\star} = \left(\frac{M_\bullet}{M_\star}\right)^{1/3} E_\star \tag{2.32}$$

is an order-of-magnitude estimate for the width of this energy distribution, and $E_\star \equiv M_\star/R_\star$ is a similar estimate for the specific self-binding energy of the star. The mass hierarchy $M_\star \ll M_\bullet$ implies that $E_\star \ll E_t$, supporting the assumption of freezing models that the relative velocities of fluid elements at the time of disruption can be neglected when determining the debris energy distribution.

In trying to compare this relativistic result to Newtonian predictions, we encounter the same issue of choosing a mapping between the two gravitational theories that we addressed in Sec. 2.4. Mapping (1), which was used in Kesden (Kesden, 2012), compared Eq. (2.31) to

Newtonian orbits with the same pericenter coordinate and found

$$\sigma_{E,\mathrm{N,PD(1)}} = \frac{M_\bullet R_\star}{r^2} = E_t \left(\frac{r_t}{r}\right)^2 . \tag{2.33}$$

Dividing Eq. (2.31) by Eq. (2.33) yields a peak correction of $\sqrt{2}$ for $r = 4M_\bullet$, the minimum pericenter for an orbit that avoids direct capture by the horizon. As argued in Sec. 2.4 however, this mapping is a somewhat unnatural way to identify orbits in the two theories.

Mapping (2) compared Schwarzschild geodesics to Newtonian orbits with the same angular momentum L (and hence penetration factor $\beta = L_t^2/L^2$). For this choice, the width of the Newtonian energy distribution is

$$\sigma_{E,\mathrm{N,PD(2)}} = \frac{M_\bullet R_\star}{r_L^2} = E_t \left(\frac{2M_\bullet}{L^2}\right)^2 = \beta^2 E_t \ , \tag{2.34}$$

where r_L is the pericenter of a Newtonian orbit with angular momentum L. Freezing models posit that the energy distribution is frozen in for $\beta > \beta_{N,d}$, implying that $\sigma_{E,\mathrm{N,FD(2)}} = \beta_{N,d}^2 E_t$ for full disruptions in mapping (2). Although there is no nice analytic expression for the widths $\sigma_{E,\mathrm{GR,FD}}$ for full disruption in general relativity, they can be calculated numerically using Eq. (2.30). We show the widths of these distributions in mapping (2) for both partial and full disruptions in the left panel of Fig. 2.7. We see that for partial disruptions $\beta < \beta_d$, the energy distribution is broader in relativity than Newtonian gravity. The ratio $\sigma_{E,\mathrm{GR}}/\sigma_{E,\mathrm{N(2)}}$ reaches a maximum value of $4\sqrt{2}$ at $M_{\max}$, even larger than the peak correction in mapping (1). However, the weaker tides in Newtonian gravity imply that stars can reach larger penetration factors $\beta_{N,d} > \beta_d$ before being fully disrupted. SBHs with masses $M_\bullet \simeq 10^6 M_\odot$ can have deeply penetrating encounters $\beta_d < \beta < \beta_{\mathrm{cap}}$ where the star still manages to avoid direct capture. For such penetration factors, the relativistic prediction can fall below that in Newtonian gravity as can be seen near the right edge of the left panel of Fig. 2.7. It is interesting to note that the relativistic predictions retain some mild β dependence for full disruptions $\beta > \beta_d$, unlike in Newtonian freezing models. This is because the tidal tensor

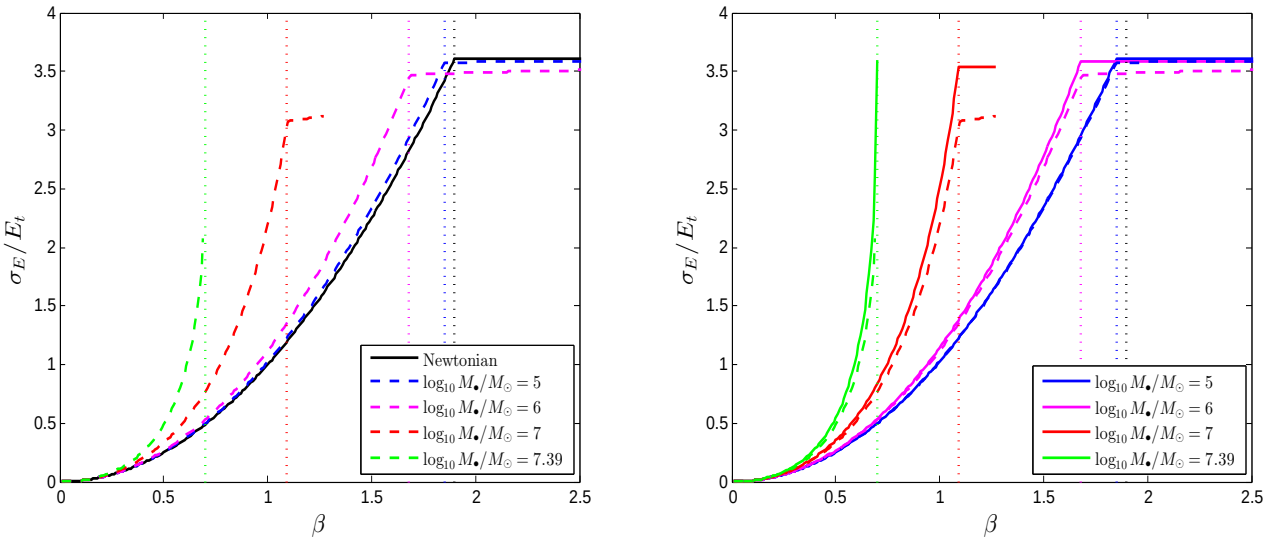

Figure 2.7: Dimensionless width σ_E/E_t of the tidal debris energy distribution as a function of penetration factor β. The solid curves show the Newtonian predictions $\sigma_{E,\mathrm{N}}/E_t$, while the dashed blue, magenta, red, and green curves show the relativistic predictions $\sigma_{E,\mathrm{GR}}/E_t$ for $M_\bullet/M_\odot = 10^5$, 10^6, 10^7, and $10^{7.39}$. The last value is $M_{\max}$, the most massive SBH capable of fully disrupting a Solar-type star. The vertical dotted lines show the thresholds β_d for full disruption; each of the relativistic curves end at β_{cap}. The single black curve in the left panel shows the Newtonian prediction in mapping (2) which is independent of SBH mass, while the three solid curves in the right panel show the Newtonian predictions for mapping (3).

${C^{(i)}}_{(j)}$ and energy width $\sigma_{E,\mathrm{GR}}$ are velocity-dependent in relativity, even if evaluated at the fixed tidal acceleration $2M_\star/(\eta R_\star)^2$ set by the star's self gravity.

Mapping (3) solves the problem of stars being fully disrupted at different values of β in the two theories by identifying the Schwarzschild geodesic with penetration factor β with the Newtonian orbit with penetration factor $\beta_N(\beta)$ on which a star experiences the same peak tidal force at pericenter as shown in Fig. 2.3. In this case, the width of the energy distribution for partial disruptions is

$$\sigma_{E,\mathrm{N,PD(3)}} = \frac{M_\bullet R_\star}{r_F^2} = \beta_N^2(\beta) E_t = \frac{M_\bullet R_\star}{r^2}\left(\frac{r+M_\bullet}{r-2M_\bullet}\right)^{2/3} , \tag{2.35}$$

where r_F is the pericenter of a Newtonian orbit with penetration factor $\beta_N(\beta)$ and r as previously is the pericenter in Boyer-Lindquist coordinates of a Schwarzschild geodesic with penetration factor β. This width again freezes out at $\sigma_{E,\mathrm{N,FD(3)}} = \beta_{N,d}^2 E_t$ for full disruptions as in mapping (2), but these full disruptions now occur for $\beta > \beta_d$ as in general relativity. We show $\sigma_{E,\mathrm{GR}}$ and $\sigma_{E,\mathrm{N(3)}}$ as functions of penetration factor β in the right panel of Fig. 2.7. We see that full disruption occurs at β_d in both theories with this mapping, but that for a given penetration factor β, the relativistic predictions $\sigma_{E,\mathrm{GR}}$ are now below the Newtonian predictions $\sigma_{E,\mathrm{N(3)}}$. The deeper penetration needed for tidal disruption in Newtonian gravity leads to steeper potential gradients and thus broader tidal debris energy distributions. The ratio $\sigma_{E,\mathrm{GR}}/\sigma_{E,\mathrm{N(3)}}$ reaches a minimum value of $(128/625)^{1/6} \simeq 0.768$ at M_{max}. The Newtonian orbit mapped to the Schwarzschild geodesic with $L_{\mathrm{cap}} = 4M_\bullet$ has $L_N = (1024/5)^{1/6} M_\bullet \simeq 2.43 M_\bullet < L_{\mathrm{cap}}$, but this is not a problem in principle since Newtonian point masses have no horizons to capture stars.

Which of the three expressions given by Eqs. (2.33), (2.34), (2.35) is the "right" one to use when comparing TDEs in Newtonian gravity with those in general relativity? The answer to this question depends on which of the three mappings discussed in Sec. 2.4 you are using to relate orbits in the two theories. If you want to compare orbits with the same angular momentum L, Eq. (2.34) provides the width of the tidal energy distribution for a Newtonian orbit with the same penetration factor β, leading to more tightly bound debris in relativity for partial disruptions as seen in the left panel of Fig. 2.7. However, this choice implies that different fractions of the stellar mass are stripped away by tides as seen in Fig. 2.8. More material is lost by the partially disrupted star in relativity, further enhancing the fallback accretion rate in addition to the more tightly bound material falling back more quickly. For $\beta_d < \beta < \beta_{d,N}$, full disruptions occur in general relativity but not Newtonian gravity, while for $\beta > \beta_{d,N}$ stars are fully disrupted in both theories but the tidal debris is more tightly bound in Newtonian gravity.

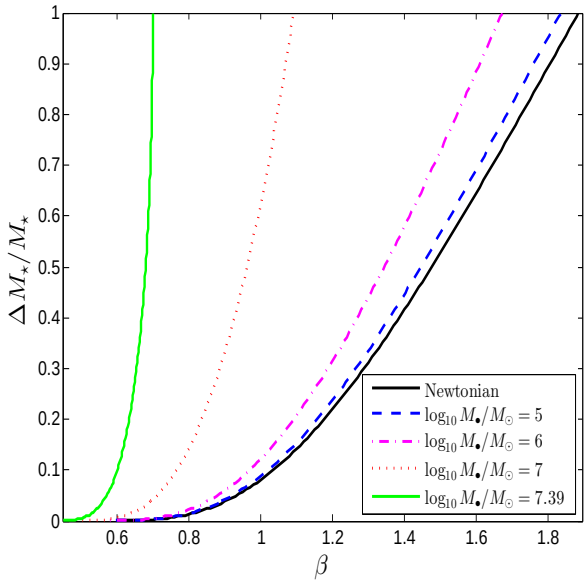

Figure 2.8: The fraction $\Delta M_\star/M_\star$ of the stellar mass lost in partial disruptions as a function of penetration factor β. The solid black curve shows a fit to Newtonian simulations (Guillochon and Ramirez-Ruiz, 2013), while the blue, magenta, red, and green curves show the corresponding relativistic predictions made using our mapping $\beta_N(\beta)$ for SBH masses $M_\bullet/M_\odot = 10^5$, 10^6, 10^7, and $M_{\rm max}/M_\odot \simeq 10^{7.39}$.

If you are instead trying to use Newtonian TDE simulations like those in Guillochon and Ramirez-Ruiz (Guillochon and Ramirez-Ruiz, 2013) to predict what this process might be like in relativity, you should use mapping (3) to relate orbits experiencing the same peak tidal forces and thus the same amount of mass loss by partially disrupted stars. Eq. (2.35) should be used to determine the relativistic correction $\sigma_{E,\rm GR}/\sigma_{E,\rm N(3)}$ as shown in the right panel of Fig. 2.7. We use this correction to predict the peak fallback accretion rate and time delay

$$\dot{M}_{\rm peak}(\beta) = \left(\frac{\sigma_{E,\rm GR}}{\sigma_{E,\rm N(3)}}\right)^{3/2} \times \dot{M}_{\rm peak}[\beta_N(\beta)]\,, \tag{2.36a}$$

$$t_{\rm peak}(\beta) = \left(\frac{\sigma_{E,\rm GR}}{\sigma_{E,\rm N(3)}}\right)^{-3/2} \times t_{\rm peak}[\beta_N(\beta)]\,, \tag{2.36b}$$

in general relativity, where the exponent of 3/2 follows from the energy dependence in Kepler's third law (2.29). We show the corrected differential TDE rates $d\dot{N}/d\dot{M}_{\rm peak}$ and

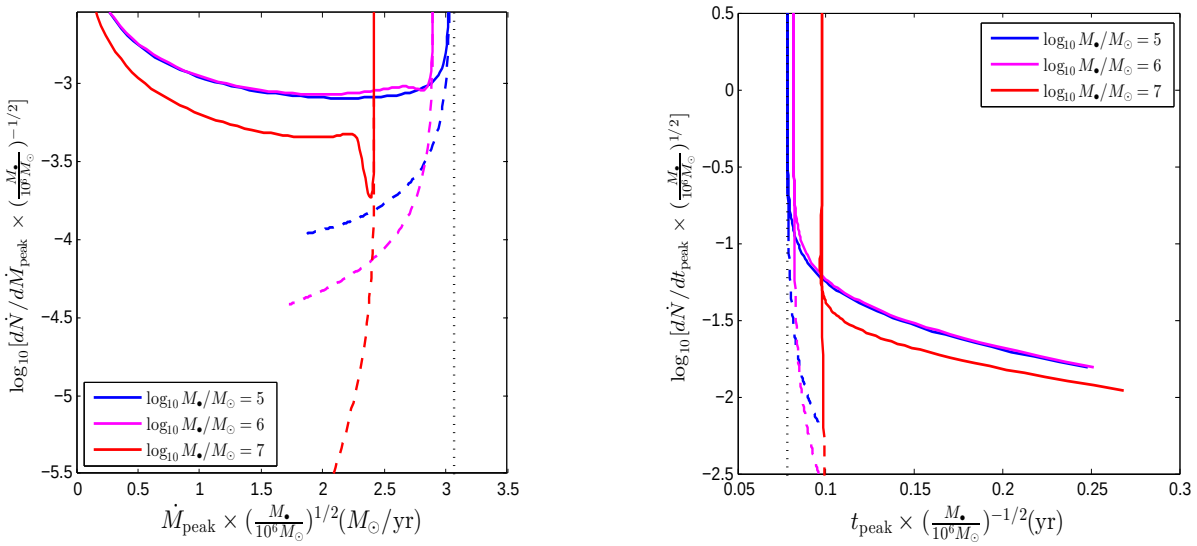

Figure 2.9: The differential TDE rates $d\dot{N}/d\dot{M}_{\rm peak}$ (left panel) and $d\dot{N}/dt_{\rm peak}$ (right panel) as functions of the peak fallback accretion rate $\dot{M}_{\rm peak}$ and time delay $t_{\rm peak}$ between disruption and when this peak is reached. The blue, magenta, and red curves show SBH masses $M_\bullet/M_\odot = 10^5$, 10^6, and 10^7. The solid curves show partial disruptions while the dashed curves show full disruptions. The vertical black dotted lines show the values in Newtonian gravity at the threshold $\beta_{N,d}$ for full disruption.

$d\dot{N}/dt_{\rm peak}$ in Fig. 2.9. For a $10^7 M_\odot$ SBH, this energy correction has reduced the mean value of the (scaled) peak accretion rate $\dot{M}_{\rm peak}$ to $2.337\, M_\odot/{\rm yr}$ and increased the mean value of the (scaled) time delay $t_{\rm peak}$ to $0.1013\,{\rm yr}$. These correspond to $\sim 20\%$ changes compared with the Newtonian predictions given at the end of Sec. 2.5.2, consistent with Eq. (2.36) and the ratios of the curves shown in the right panel of Fig. 2.7. Note that these changes dominate the effect of direct capture discussed at the end of Sec. 2.5.2. Fig. 2.9 conveys the qualitative message of this subsection: the stronger tides in general relativity allow SBHs to tidally disrupt stars at lower penetration factors β leading to less tightly bound debris and lower fallback accretion rates. This conclusion is supported by Fig. 7 and Table II of Cheng and Bogdanović (Cheng and Bogdanović, 2014) which show positive values of the delay in peak time between relativistic and Newtonian simulations, indicating that tidal debris is less tightly bound in relativistic simulations and therefore takes longer to return to pericenter.

2.5.4 Capture of tidal debris by the event horizon

In this subsection, we focus on an issue that was only briefly addressed in Kesden (Kesden, 2012): tidal debris can be captured by the event horizon of an SBH even if the disrupted star is not initially on a capture orbit. In general relativity, the tidal debris will have a distribution of specific angular momentum L with a width given by

$$\sigma_{L,\mathrm{GR}} = |\lambda^{\alpha}{}_{(i)} \nabla_{\alpha} L| R_{\star} = |g_{\beta\gamma} \lambda^{\beta}{}_{(0)} \lambda^{\alpha}{}_{(i)} \Gamma^{\gamma}_{\alpha\phi}| R_{\star} \tag{2.37}$$

analogous to Eq. (2.30) giving the width of the specific energy distribution. This width is set at pericenter r for partial disruptions, allowing us to evaluate Eq. (2.37) as

$$\sigma_{L,\mathrm{GR,PD}} = R_{\star} \left(\frac{2M_{\bullet}}{r} \right)^{1/2} = L_t \left(\frac{M_{\star}}{M_{\bullet}} \right)^{1/3} \left(\frac{r_t}{r} \right)^{1/2} . \tag{2.38}$$

The mass hierarchy $M_{\star} \ll M_{\bullet}$ between the star and SBH implies that $\sigma_{L,\mathrm{GR}} \ll L_t$ and thus that it is usually a good approximation to assume that the specific angular momentum of the tidal debris is equal to that of the initial star. This contrasts with the debris energy distribution for which $E_t \gg \sigma^2$ implying that the tidal debris is much more tightly bound to the SBH than the initial star. However, for highly relativistic TDEs, the small amount of specific angular momentum lost in the disruption process may be enough for some of the tidal debris to be captured by the horizon. We examine this possibility by defining the dimensionless parameter

$$f_L \equiv \frac{L + \Delta L - L_{\mathrm{cap}}}{|\Delta L|} = \frac{L - 4M_{\bullet}}{|\Delta L|} - 1 \, , \tag{2.39}$$

where L is the specific angular momentum of the initial star, $\Delta L < 0$ is the change in specific angular momentum of a fluid element in the disruption process, and $L_{\mathrm{cap}} = 4M_{\bullet}$ is the specific angular momentum threshold for direct capture by the horizon. An element of the tidal debris with $f_L < 0$ will be captured by the SBH, and $f_L = -1$ is the minimum value of this parameter for a star that is not originally on a capture orbit ($L > L_{\mathrm{cap}}$).

We need an estimate for ΔL to evaluate our new parameter f_L. In the freezing model, an element of the tidal debris located at $X^{(i)}$ in Fermi normal coordinates at tidal disruption has its specific energy and angular momentum changed by an amount

$$\Delta E \equiv X^{(i)} r_{E(i)} = X^{(i)} \lambda^{\alpha}_{\ (i)} \nabla_{\alpha} E \,, \tag{2.40a}$$

$$\Delta L \equiv X^{(i)} r_{L(i)} = X^{(i)} \lambda^{\alpha}_{\ (i)} \nabla_{\alpha} L \,, \tag{2.40b}$$

in the tidal-disruption process. The element of the star that will become the most tightly bound element of the tidal debris will have $X^{(i)}$ of magnitude $R_\star$ anti-aligned with $r_{E(i)}$, leading to the specific binding energy $\sigma_{E,\mathrm{GR}}$ given by Eq. (2.30). The element of the star that loses the most angular momentum in the tidal-disruption process will have $X^{(i)}$ of magnitude $R_\star$ anti-aligned with $r_{L(i)}$ and have its angular momentum reduced by an amount $\sigma_{L,\mathrm{GR}}$ given by Eq. (2.37). If $r_{E(i)}$ and $r_{L(i)}$ are parallel to each other (as at pericenter in Newtonian gravity, where both point in the radial direction), the same element of the tidal debris will be both the mostly tightly bound (the first to fall back onto the SBH) and have lost the most angular momentum (and thus be at greatest risk for direct capture). This is also true in general relativity when freezing occurs at pericenter, i.e. $\beta \leq \beta_d$. A consequence of $r_{E(i)}$ and $r_{L(i)}$ being parallel is a one-to-one relationship between the change in specific orbital energy and angular momentum, symmetric for gains and losses. Numerical simulations of full disruptions in general relativity show that this symmetric one-to-one relationship begins to break down for relativistic TDEs only mildly beyond the threshold for full disruption (Cheng and Bogdanović, 2014).

TDEs for which $f_L \leq 0$ for $\Delta L = -\sigma_{L,\mathrm{GR}}$ in Eq. (2.39) will have suppressed fallback accretion rates and greater delays between disruption and the beginning of emission because direct capture will have removed the most tightly bound debris. Furthermore, if $r_{E(i)}$ and $r_{L(i)}$ are parallel, there is a one-to-one relationship

$$\Delta L = \frac{|r_{L(i)}|}{|r_{E(i)}|} E \tag{2.41}$$

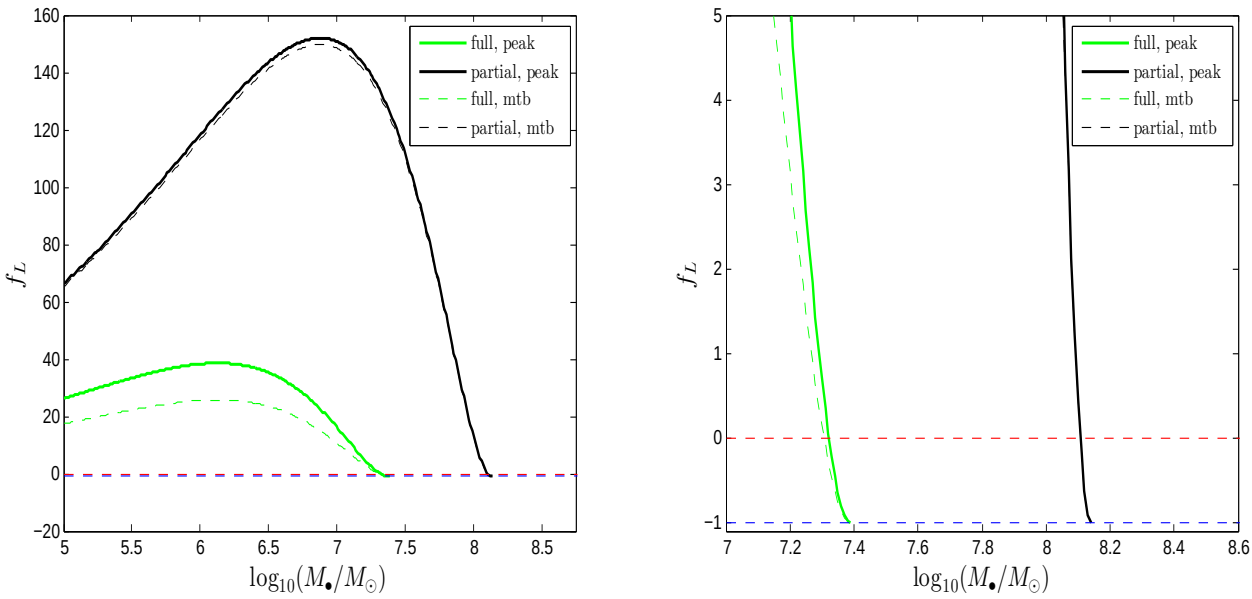

Figure 2.10: The parameter $f_L \equiv (L + \Delta L - L_{\rm cap})/|\Delta L|$, a measure of whether tidal debris is at risk of direct capture by the event horizon, as a function of SBH mass $M_\bullet$. The green (black) curves correspond to stars at the thresholds $\beta = \beta_d$ (β_{pd}) for full (partial) disruptions. The solid curves correspond to elements of the tidal debris that fall back onto the SBH when fallback accretion peaks, while the dashed curves represent the most tightly bound (mtb) elements (first to fall back). The red (blue) horizontal dashed lines show the reference values $f_L = 0$ (-1).

between the specific binding energy E of an element of tidal debris and the specific angular momentum ΔL it loses during tidal disruption. If we use Kepler's third law (2.29) to relate the time delay $t_{\rm peak}$ to the specific binding energy $E_{\rm peak}$ of debris accreted at that time, we can use Eq. (2.41) to estimate ΔL and thus f_L for such debris. When this estimate of f_L becomes negative, all of the debris accreted before the fallback accretion rate reaches its peak will be captured by the horizon.

We show f_L for both peak and most tightly bound fluid elements as a function of SBH mass $M_\bullet$ in Fig. 2.10, for stars with penetration factors β_d and β_{pd} corresponding to the thresholds for full disruption and nonzero partial disruption. For the most tightly bound

elements with $\Delta L = -\sigma_{L,\mathrm{GR}}$, Eq. (2.39) yields

$$f_L = \left(\frac{M_\bullet}{M_\star}\right)^{1/3} \left(\frac{r}{r_t}\right)^{1/2} \left[\frac{1}{\sqrt{\beta}} - \left(\frac{M_\bullet}{M_\star}\right)^{1/3} \sqrt{8E_\star}\right] - 1\,. \tag{2.42}$$

For $M_\star \ll M_\bullet$, the term in the square brackets goes to $\beta^{-1/2}$ and $f_L \propto M_\bullet^{1/3}$, however as $M_\bullet$ increases this term decreases and ultimately reaches zero ($f_L = -1$) for $L = L_{\mathrm{cap}}$ when the entire star is directly captured. This increase then subsequent decrease in f_L as a function of $M_\bullet$ is seen in the left panel of Fig. 2.10 indicating that tidal debris is safe from direct capture for all but the most massive SBHs. Only when $M_\bullet$ is within $\sim 20\%$ of M_{max} does the direct capture of tidal debris become significant as seen in the right panel of Fig. 2.10. Although such events constitute only a small fraction of the total TDE rate, they are the TDEs subject to the most extreme relativistic effects such as the pericenter precession that will be considered in the next subsection.

2.5.5 Relativistic pericenter precession

Early work on TDEs assumed that tidal debris would promptly circularize after falling back to pericenter (Rees, 1988), but Newtonian hydrodynamical simulations demonstrated that energy dissipation at pericenter was inefficient for $M_\star \ll M_\bullet$ (Guillochon et al., 2014). Early analytic work (Kochanek, 1994) suggested that relativistic pericenter precession might promote orbit circularization, because this precession would lead to steam crossings at which the inelastic collisions of tidal elements would transform orbital kinetic energy into heat that could be subsequently radiated away. This suggestion was later supported by relativistic TDE simulations in which such precession was indeed shown to generate tidal stream crossings (Hayasaki et al., 2013; Dai et al., 2013; Guillochon and Ramirez-Ruiz, 2015; Shiokawa et al., 2015; Cheng and Bogdanović, 2014).

The angular coordinate ω specifying the location of pericenter with respect to a reference axis in the orbital plane is known as the argument of pericenter. In Newtonian gravity,

the argument of pericenter is a constant of motion, but this is not true for Schwarzschild geodesics of the metric (2.10) in Boyer-Lindquist coordinates. At lowest post-Newtonian (PN) order, the argument of pericenter changes by an amount

$$\Delta\omega_{\rm 1PN} = 6\pi \left(\frac{M_\bullet}{L}\right)^2 = 3\pi\beta \left(\frac{M_\bullet}{M_\star}\right)^{2/3} E_\star \,. \tag{2.43}$$

This PN approximation breaks down for $L \simeq L_{\rm cap}$ for which pericenter precession must be integrated numerically along Schwarzschild geodesics,

$$\Delta\omega_S = 2\int_r^\infty \frac{\dot{\phi}}{|\dot{r}|} dr' - 2\pi \,, \tag{2.44}$$

where

$$\dot{r} = \pm \left\{ \frac{2M_\bullet}{r} \left[1 + \left(\frac{L}{r}\right)^2 \right] - \left(\frac{L}{r}\right)^2 \right\}^{1/2} \tag{2.45a}$$

$$\dot{\phi} = \frac{L}{r^2} \tag{2.45b}$$

are the first-order derivatives of the Boyer-Lindquist coordinates r and ϕ with respect to proper time τ. This breakdown is also seen in Fig. 5 of Cheng and Bogdanović (Cheng and Bogdanović, 2014), where larger deviations from the PN approximation occur for deeply penetrating orbits. The lower limit of the integral in Eq. (2.44) is the pericenter r which depends implicitly on L and hence β through Eq. (2.19). We can set the upper limit of this integral to ∞ since we assume the tidally disrupted stars are initially on nearly parabolic orbits and the tidal debris remains highly eccentric. Eq. (2.38) also indicates that we can approximate the specific angular momentum of the tidal debris as equal to that of the initial star. We plot $\Delta\omega_{\rm 1PN}$ and $\Delta\omega_S$ in Fig. 2.11, which shows that pericenter precession diverges at $L = L_{\rm cap}$ guaranteeing a tidal stream crossing and perhaps subsequent orbit circularization of the tidal debris.

Given that $\Delta\omega_S$ is a function of β, we can use the differential TDE rate $d\dot{N}/d\beta$ derived in Sec. 2.5.1 and shown in the right panel of Fig. 2.5 to derive the differential TDE rate $d\dot{N}/d\Delta\omega$.

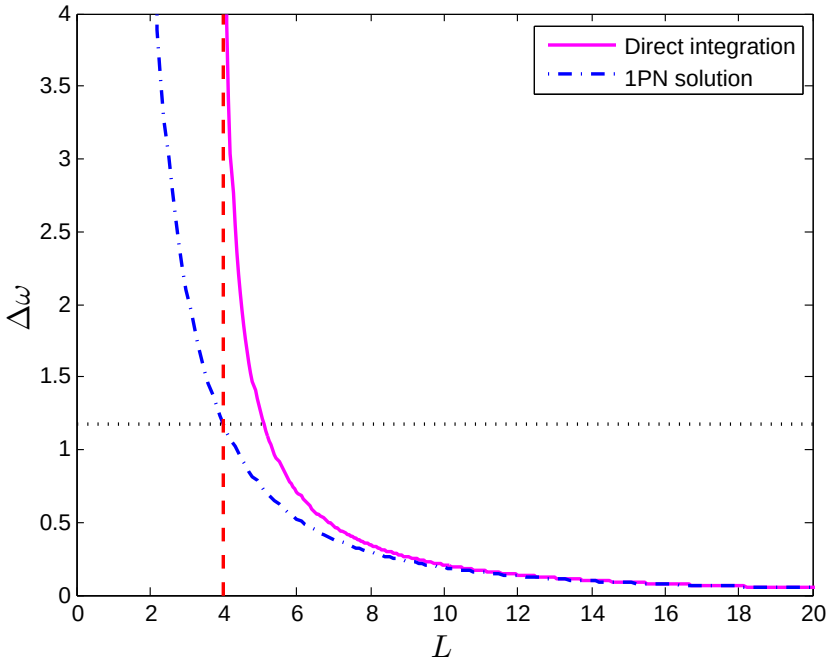

Figure 2.11: Precession of argument of pericenter $\Delta\omega$ (in units of radians) as a function of the specific angular momentum L. The solid magenta and dot-dashed blue curves show the exact precession and its 1PN approximation, respectively. The vertical dashed red line show the capture threshold $L_{\rm cap} = 4M_\bullet$ and the horizontal dotted line shows the 1PN prediction for precession at this threshold.

We show this rate in Fig. 2.12 for several SBH masses $M_\bullet$. As expected from Eq. (2.43), TDEs by more massive SBHs have greater amounts of pericenter precession suggesting that relativistic orbit circularization might be more effective in such events. Greater pericenter precession may also lead to hotter accretion disks, accounting for the discrepancy in color temperatures between TDEs discovered in the optical and X-ray (Dai et al., 2015). Further investigation of this possibility requires a criterion for orbit circularization that we hope to explore in future work. We also note that the differential TDE rate $d\dot{N}/d\beta$, and thus all the distributions shown in this section including $d\dot{N}/d\Delta\omega$, depends on the stellar density profile $\rho(r)$. A profile yielding a larger fraction of TDEs in the full loss-cone (pinhole) regime would provide more stars on deeply penetrating orbits and thus a fattening of the large $\Delta\omega$ tails of the curves in Fig. 2.12.

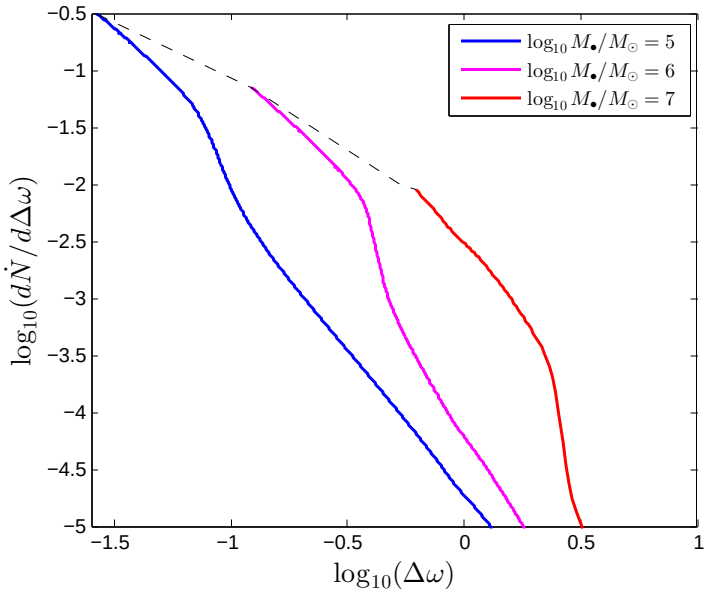

Figure 2.12: The differential TDE rate $d\dot{N}/d\Delta\omega$ as a function of the precession of the argument of pericenter $\Delta\omega$. The solid blue, magenta, and red curves show this distribution for SBH masses $M_\bullet/M_\odot = 10^5$, 10^6, and 10^7, respectively. The dashed black curve connects the lower limit of each rate curve corresponding to the threshold β_{pd} of partial disruption.

2.6 Discussion

In this paper, we have systematically compared tidal disruption by Schwarzschild black holes in general relativity and point masses in Newtonian gravity. Differences between the two theories have potentially observable consequences for both TDE rates and the properties of individual events:

(1) Tidal forces are stronger in general relativity than Newtonian gravity for orbits with the same penetration factor $\beta \equiv L_t^2/L^2$. This implies that the loss cone within which stars are tidally disrupted is larger in general relativity: $L_d > L_{d,N} \implies \beta_d < \beta_{d,N}$. Partially disrupted stars with $\beta < \beta_d$ will lose more material in relativity than Newtonian gravity, and stars with $\beta_d < \beta < \beta_{d,N}$ will be fully disrupted in relativity but not Newtonian gravity.

(2) The width σ_E of the energy distribution of tidal debris is larger in general relativity than Newtonian gravity for orbits with the same penetration factor β. This implies that

stars will not only lose more material in partial disruptions in relativity, but this material will become more tightly bound to the SBH and fall back to pericenter more quickly, leading to a higher peak luminosity if the radiative efficiency is fixed. However, stars that are fully disrupted in both theories ($\beta > \beta_{d,N}$) will be disrupted higher in the potential well in relativity than Newtonian gravity because of the stronger tides. This implies that the tidal debris will be less tightly bound despite the relativistic correction and therefore that the peak fallback accretion rate is lower in relativity than Newtonian gravity.

(3) Black holes have event horizons in general relativity that allow them to directly capture stars. This reduces the TDE rate in relativity compared to Newtonian gravity, since tidal debris captured by the horizon cannot emit photons detectable by observers. As the threshold $L_{\rm cap}$ for direct capture increases more steeply with SBH mass than the thresholds L_d and L_{pd} for full and partial disruptions, SBHs with masses greater than $M_{\rm max,d} = 2.5 \times 10^7 M_\odot$ and $M_{\rm max,pd} = 1.4 \times 10^8 M_\odot$ will no longer be capable of full and partial disruption, respectively. These limits would have been underestimated by a factor of ~ 4.5 without accounting for the stronger tides in relativity.

(4) Event horizons can capture a portion of the tidal debris in general relativity, even if the tidally disrupted star is not initially on a capture orbit. Tidal debris loses both energy and angular momentum during tidal disruption. If the specific angular momentum of the initial star was already close to the capture threshold, this additional loss can cause some of the debris to plunge directly into the horizon. This captured debris is the most tightly bound part of the tidal stream for $\beta \lesssim \beta_d$, so its capture suppresses the early portions of the TDE light curve assuming the luminosity traces the fallback accretion rate.

(5) Tidal streams precess in general relativity, potentially leading to inelastic collisions between parts of the stream that allow energy to be dissipated and debris orbits to circularize. At lowest PN order, this precession scales as $M_\bullet^{2/3}$ at the threshold β_d for full disruption, but it increases more steeply with SBH mass as β_d approaches the threshold for direct capture $\beta_{\rm cap}$.

In future work, we plan to explore how SBH spin affects all five of these relativistic effects. By breaking the spherical symmetry of the spacetime, SBH spin increases the parameter space to include spin magnitude, orbital inclination, and argument of pericenter. As the tidal forces along geodesics depend on all these parameters, the diffusion equation determining the rate at which stars enter the loss cone will likely need to be solved numerically to account for the higher-dimensional boundary conditions. Qualitatively, we expect TDE rates to be biased in favor of stars on retrograde orbits for moderate SBH masses, but this bias should switch towards stars on prograde orbits as the retrograde threshold for disruption falls below that for direct capture. Both of these biases will tend to spin down the SBH, as a larger fraction of the stellar material will be accreted in each case from retrograde orbits. TDEs from stars on prograde orbits however will be more luminous because of the more tightly bound prograde innermost stable circular orbits, leading to a potential observational bias in favor of prograde TDEs.

SBH spin also affects the relativistic precession of tidal debris, as has been found in numerical simulations (Haas et al., 2012). At 1.5PN order, spin-dependent pericenter precession opposes (supports) the 1PN pericenter precession considered in this paper on prograde (retrograde) orbits (Merritt, 2013), imposing a further bias in favor of retrograde TDEs if such precession is required for orbit circularization. SBH spin induces precession of the longitude of ascending node which can cause tidal streams to precess out of their initial orbital planes, inhibiting stream crossings and delaying orbit circularization (Kochanek, 1994; Guillochon and Ramirez-Ruiz, 2015; Hayasaki et al., 2016). Spin-dependent solutions of stellar diffusion into the loss cone will allow us to calculate the fraction of TDEs experiencing such delays between disruption and peak fallback accretion. By providing a unified treatment of TDEs in the Schwarzschild spacetime, this paper performs an important service in its own right and establishes a beachhead for attacking the more ambitious problem of tidal disruption by spinning Kerr black holes.

Acknowledgements

We would like to thank Roseanne Cheng, Chris Kochanek, David Merritt, and Nicholas Stone for useful conversations, and both Tamara Bogdanović and an anonymous second referee for valuable suggestions. M. K. is supported by the Alfred P. Sloan Foundation Grant No. FG-2015-65299 and NSF Grant No. PHY-1607031.

CHAPTER 3

A NEW MODEL FOR TRACKING THE EVOLUTION OF TIDAL DISRUPTION EVENT STREAMS

The work presented in this chapter is part of ongoing research concerning a new model for tracking the behavior and properties of the post disruption tidal stream. After a star is tidally disrupted, roughly half the total mass of the star becomes more tightly bound to the SBH and the rest becomes unbound. The bound portion must lose energy and angular momentum to produce radiation for observations, and the simplest process for this involves inelastic collisions resulting from stream self intersections followed by viscous evolution on the larger viscous timescale $t_{\rm visc}$, as discussed in Section 1.2. Current models in the TDE literature (Dai et al., 2015; Bonnerot et al., 2016; Guillochon and Ramirez-Ruiz, 2015; Bonnerot, Rossi, and Lodato, 2016) track only the most bound debris element, which could potentially yield misleading results. Our new model differs from previous work in that we parameterize the stream and track the evolution of the individual stream elements when determining the outcomes of the self intersections.

3.1 Introduction

As stated in Section 1.2, TDEs are powered by the viscous accretion of a gas stream due to the losses of angular momentum from torques between the inner and outer gas rings. The initial gas stream must instead lose energy via inelastic collisions resulting from stream self-intersections to circularize (such orbits have the least energy for a given angular momentum) and accrete onto the SBH. Recent models (Dai et al., 2015; Bonnerot et al., 2016; Guillochon and Ramirez-Ruiz, 2015; Bonnerot, Rossi, and Lodato, 2016) following this prescription invoked collisions involving only the most tightly bound stream element, arguing that the overall behavior of the stream could be characterized by a single orbit. Related work (Piran

et al., 2015; Pasham et al., 2017) has shown that the (optical) signal from TDE flares in the optical band might actually be due to the energy released from the self-intersections themselves prior to circularization. This could prove useful for astronomers, as having a well defined optical signal as a precursor could aid in searches of TDEs.

In this chapter we present our new model for tracking the behavior of the stream post disruption. Instead of characterizing the stream with a single orbit, we track the behavior of the stream as a whole and compare our results to the models in the TDE literature. We also drop the implicit assumption made in recent work (Dai et al., 2015; Bonnerot et al., 2016; Guillochon and Ramirez-Ruiz, 2015; Bonnerot, Rossi, and Lodato, 2016) that the collisions involve stream particles with equal mass, and instead use the stellar density to determine the particle masses. The radial location and stream elements involved for the first self-intersection are provided as a function of SBH mass and are compared to the results predicted by earlier models. We also determine the radial location and energy lost due to the collisions, both as a function of time.

3.2 Current methodology for tidal stream self-intersections

During the process of tidal disruption, the energy and angular momentum within the star are redistributed according to the freezing model (Lodato et al., 2009),

$$E(R) = \frac{M_\bullet R}{r_t^2}, \tag{3.1a}$$

$$L(R) = L_t \left(1 - \frac{R}{r_t}\right), \tag{3.1b}$$

where r_t and L_t are the tidal radius and angular momentum threshold for disruption, respectively, as given by Eqs. (2.1) and (2.2), and R is the radial distance (from the center of the star outward) to a particular stream element. Under this freezing model it is assumed that the orbital energy distribution of tidal debris is frozen in following the instantaneous

an unperturbed star. The reader should take note: we will be using this R as an affine parameter to characterize the stream long after disruption has occured. For example, we will be referring to the most bound stream element with $R = R_{\odot}$, as this was its radial location, with respect to the center of the star, prior to disruption. As we did in the previous chapter of this dissertation, we will use units where $G = c = 1$ and will assume that the disrupted star approached the SBH on a parabolic orbit with penetration factor $\beta = 1$.

Given the energy and angular momentum, one may obtain the semi-major axis, a, and eccentricity, e, for a particular stream element,

$$a(R) = -\frac{M_{\bullet}}{2E(R)}, \tag{3.2a}$$

$$e(R) = \sqrt{1 - 2E(R)\frac{L^2(R)}{M_{\bullet}^2}}, \tag{3.2b}$$

which are used to define the trajectories traced by these stream elements. To track the evolution of the stream over time, one may use the eccentric anomaly E (not to be confused with the energy E), defined by the equation,

$$(-2E(R))^{3/2}(t - t_0) = \mathrm{E}(R) - e(R)\sin\left(\mathrm{E}(R)\right), \tag{3.3}$$

where t is a particular moment of time, and t_0 is the time when the star was disrupted. The positions of the stream elements, as a function of $\mathrm{E}(R)$, are given by,

$$x(R) = a(R)\left(\cos\left(\mathrm{E}(R)\right) - e(R)\right), \tag{3.4a}$$

$$y(R) = a(R)\left(1 - e^2(R)\right)^{1/2}\sin\left(\mathrm{E}(R)\right). \tag{3.4b}$$

Note that this applies only for $\beta = 1$ (the star's pericenter is equal to the tidal radius), where the arguments of pericenter for all of the stream elements can be set to $\omega = 0$ at

time $t = 0$. Solving Eq. (3.3) for a particular moment of time t would allow one to use the eccentric anomaly as a proxy for time evolution. One, then, need only evolve the stream until a self intersection is produced. The orbits of the stream elements, however, trace concentric ellipses and will thus never intersect using only the above prescription.

Due to the curvature of spacetime near the SBH, orbits are rotated by an angle $\Delta\omega$ after each pericenter passage, known as pericenter precession. In reality, the precession is a continuous process, but one could approximate it as an instantaneous event that occurs when a stream element reaches its orbit's pericenter. If the velocity of the star is non-relativistic ($v_\star \ll c$) and the gravitational field is "weak" (the curvature of spacetime is not terribly high), then one can apply a Taylor expansion (in the variable v/c) to the solutions of the Einstein field equations, known as the post-Newtonian approximation. To first order, the precession per pericenter passage is given by,

$$\Delta\omega(R) = \frac{6\pi M_\bullet^2}{L^2(R)} = 0.2\beta \left(\frac{M_\bullet}{10^6 M_\odot}\right)^{2/3} \left(1 - \frac{R}{r_t}\right)^{-2}. \tag{3.5}$$

By rotating the orbits as they pass through pericenter, the concentric alignment of the orbits is broken and self intersections are now possible. The self intersections yield inelastic collisions that result in a net loss of energy in the stream. To solve for this energy loss, we use conservation of linear momentum,

$$m_\alpha \vec{v}_\alpha + m_\beta \vec{v}_\beta = m_\gamma \vec{v}_\gamma, \tag{3.6}$$

where m is the stream element mass, $\vec{v}$ is the stream element velocity, and α, β, and γ denote the precessed, infalling, and newly created stream elements, respectively. For clarity, the reason the collisions involve three stream elements is as follows. Collisions require a minimum of two particles with two different arguments of pericenter ω, hence the α (precessed, outgoing) and β (unprecessed, infalling) designations. Since these collisions are inelastic, both elements involved combine into a new, single element, hence the γ designation. The models

in the TDE literature (Dai et al., 2015; Bonnerot et al., 2016; Guillochon and Ramirez-Ruiz, 2015; Bonnerot, Rossi, and Lodato, 2016) have $m_\alpha = m_\beta$, given that they characterize the stream with a single orbit. The energy of the γ element is then the sum of its gravitational potential energy and kinetic energy,

$$E_\gamma = \frac{1}{2} v_\gamma^2 - \frac{M_\bullet}{r_{\rm col}}, \tag{3.7}$$

where $r_{\rm col}$ is the radius (from the SBH) where the collision occurs. The energy loss is then the difference of the energy before and after the collision. It has been shown by Newtonian hydrodynamical simulations(Guillochon et al., 2014) that shocks incurred at pericenter passage do not dissapate energy in the stream, and so we do not consider them. Viscous evolution takes over at some time $t > t_{\rm visc}$ and contributes to energy loss in the stream. Once enough energy has been dissapated and the stream has been circularized, torques induced by the viscosity of the stream begin to transfer angular momentum away from the inner ring of the disk and viscous accretion begins.

3.3 Our new model

As mentioned in Section (3.1), previous models have considered the above prescription using only the most bound stream element, corresponding to $R = R_\odot$. The models justify this approach by stating that the trajectory of the stream as a whole closely follows that of the most bound element. In Fig. 3.1 we show the state of the stream at at four different instances of time and see that this assumption breaks down before even the first pericenter passage of the most bound stream element. Characterizing the stream with a single orbit, then, would skew the predictions of models using this assumption, as we will show later in this section.

The model presented in this chapter uses a different parameterization (discussed in greater detail in Appendix A) than the one above. We instead bin the stream elements based on their orbital periods, defining the parameter $0 < S < \infty$,

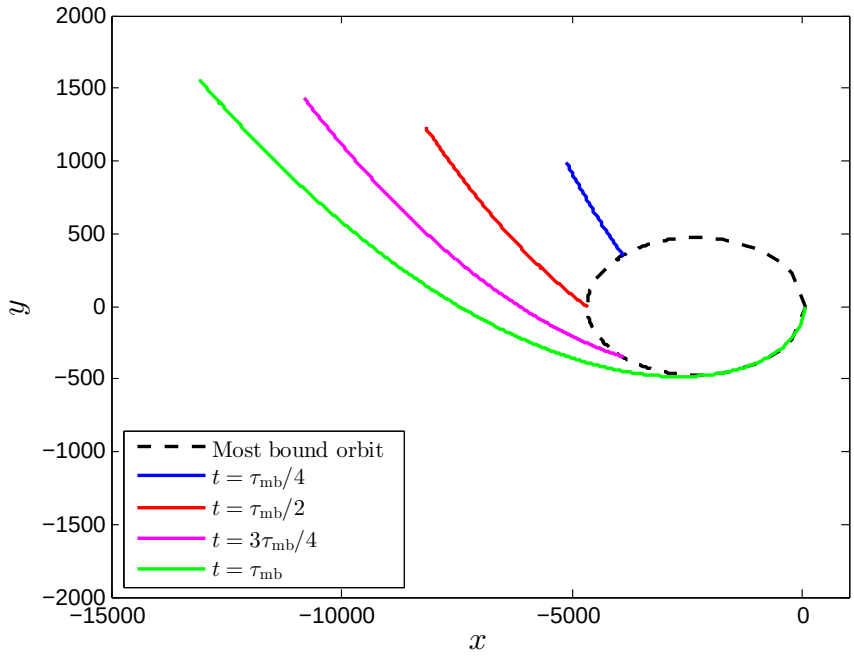

Figure 3.1: The state of the bound portion of the tidal stream post-disruption at times $t = \tau_{\rm mb}/4$ (blue), $t = \tau_{\rm mb}/2$ (red), $t = 3\tau_{\rm mb}/4$ (magenta), and $t = \tau_{\rm mb}$ (green), where $\tau_{\rm mb}$ is the orbital period of the most bound element. The dashed black ellipse shows the trajectory followed by the most bound stream element and is included to emphasize that the entire stream is not characterized well by a single orbit.

$$S = \frac{\tau}{\tau_{\rm mb}} - 1, \tag{3.8}$$

where τ is the orbital period of the stream element and $\tau_{\rm mb}$ is the orbital period of the most bound element. Using this definition, the most bound stream element corresponds to $S = 0$, with the rest of the stream having $S > 0$ given that the most bound element has the shortest orbital period via Kepler's third law. As a function of this S, the energy and angular momentum distributions are,

$$E(S) = E_t \left(1+S\right)^{-2/3}, \tag{3.9a}$$

$$L(S) = L_t \left(1 - \frac{R_\odot}{r_t}\left(1+S\right)^{-2/3}\right). \tag{3.9b}$$

The rest of the orbital parameters, being functions of E and L, can likewise be binned in S using Eqs. (3.2-3.5).

Our new model also drops the implicit assumption that all stream elements involved in the collision are of equal mass. We instead solve the Lane-Emden equation, which is a dimensionless form of the equation of hydrostatic equilibrium for a spherically symmetric polytropic fluid (Lodato et al., 2009). The equation has the form,

$$\frac{d^2\theta}{d\xi^2} + \frac{2}{\xi}\frac{d\theta}{d\xi} + \theta^n(\xi) = 0 \tag{3.10}$$

where $\xi = r/R_\star$ is a dimensionless radius from the center of the star, θ is related to the stellar density via $\rho = \rho_c\theta^n$, with ρ_c the density at the center of the star, and n is the polytropic index of the star. The polytropic index appears in the polytropic equation of state,

$$P = K\rho^{1+\frac{1}{n}}, \tag{3.11}$$

where P is the gas pressure and K is a proportionality constant. We set the polytropic index to $n = 3$ as this corresponds to Sun-like stars. Solving this differential equation for the mass density ρ then allows one to obtain the mass contained in the stream as a function of R, and therefore as a function of S, as well (Lodato et al., 2009). We show the differential mass dM/dS as a function of S in Fig. 3.2. Note that at late times ($\log_{10} S \geq 2$) the differential mass begins to fall off with power $-5/3$, the same decay rate in early TDE predictions (Rees, 1988; Evans and Kochanek, 1989; Genzel et al., 1986; Luminet and Carter, 1983).

Combining all of the above, the procedure for our model is as follows,

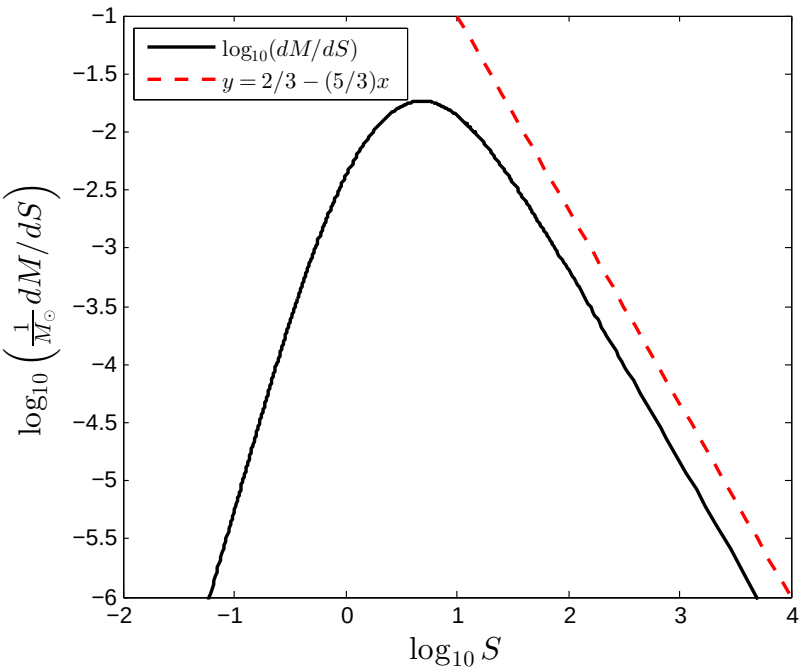

Figure 3.2: The logarithm of the differential mass dM/dS as a function of $\log_{10} S$. Note that at late times (larger S values) the mass falls off with power $-5/3$, similar to the fallback accretion rate seen in early TDE models. (Rees, 1988; Evans and Kochanek, 1989; Genzel et al., 1986; Luminet and Carter, 1983)

(1) evolve the stream forward in time by some time step Δt using Eq. (3.3),

(2) determine the collision radius $r_{\rm col}$, stream velocities $\vec{v}_\alpha$ $\vec{v}_\beta$, and masses of the stream elements involved using Eq. (3.10),

(3) determine the velocity $\vec{v}_\gamma$ and mass m_γ of the new stream element using Eq. (3.6),

(4) determine the energy of the new stream element using Eq. (3.7), and thus determine the energy lost due to the collision,

(5) repeat from Step (1).

The γ element is then added to the stream, and adopts an S parameter of $S_\gamma = S_\beta$ as a convention and is appended to the α stream (since this new particle will eventually pass

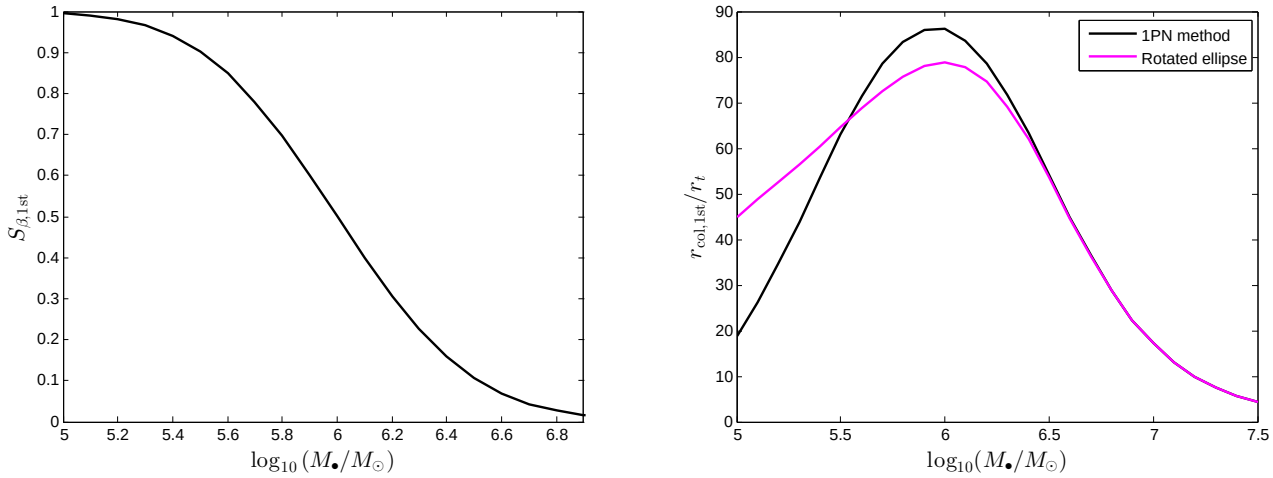

Figure 3.3: The S parameter of the second stream element involved in the first self intersection (left) and the radial distance from the SBH (right) where the self intersection occured, both as a function of SBH mass. For the right panel, the model presented in this chapter is labeled "1PN method", and a model (Dai et al., 2015) that used only the most bound stream element is labeled "rotated ellipse."

through pericenter and be precessed). The mass of the γ element is equal to the sum of the α and β element, following mass conservation. The velocity v_γ is determined via Eq. (3.6). The orbit of the new stream element will not be concentric with the infalling β stream, and so the argument of pericenter ω_γ is determined for each new γ element.

3.4 Results

The most bound stream element will always be involved in the first self-intersection, as it has the shortest orbital period and all of the stream orbits are confined to a single plane. We show, as a function of SBH mass, the S parameter for the second stream element involved in the first collision and the radial distance from the SBH where the collision occurs for both models in Fig. 3.3. Note the behavior at both ends of the SBH mass limits. We know from Eq. (3.5) that orbits around larger (smaller) SBHs will experience stronger (weaker) precession per pericenter passage. For very large SBHs, the precession can become so extreme

that the leading stream element (with $S = 0$) would appear as if it were colliding with itself. We see such behavior in the left panel of Fig. 3.3, where the S parameter for the second particle assymptotically approaches zero with increasing SBH mass. In the limit that precession vanishes (for lower mass SBHs) the stream only approximately intersects at pericenter, given the very narrow distribution of pericenters for the entire stream. Therefore, the first collision would occur between the most bound element and another element that reaches its pericenter at the same time. In other words, the second stream element's orbital period must be an integer multiple of the most bound element's orbital period (*i.e.* $S = 1$, $S = 2$, etc.) and so the first collision will involve $S_\beta = 1$, which we see in the lower mass section on the left panel of Fig. 3.3.

The radial position of the first self-intersection, shown in the right panel of Fig. 3.3, also supports the above. For larger SBH masses we see that the collision radius assymptotically falls towards the tidal radius, consistent with the notion that the increasing precession angles eventually cause the leading stream element to collide with itself at pericenter passage (recall that for $\beta = 1$ the star's pericenter is equal to the tidal radius). For lower mass SBHs, we argued that the vanishing precession would lead to the first collisions occuring closer to pericenter, which we also see in Fig. 3.3. It is unsurprising to see that our model, labeled "1PN method" in Fig. 3.3, agrees with models (Dai et al., 2015) using only the most bound stream element, labeled "rotated ellipse", at higher SBH masses since the large amount of precession eventually leads to the lead element colliding with itself.

For the rest of this chapter, we will focus on an SBH of mass $M_\bullet = 10^6 M_\odot$ to explore the properties of subsequent collisions. Following our model, to obtain predictions for light curves we need to know where the collisions occured and the masses of the stream elements involved. We show in Fig. 3.4 the radial distance $r_{\rm col}$ from the SBH where the self-intersections occur as a function of time t after disruption. The self-intersections initially recede from the SBH because the leading stream elements approach their apocenters at time of collision. At about

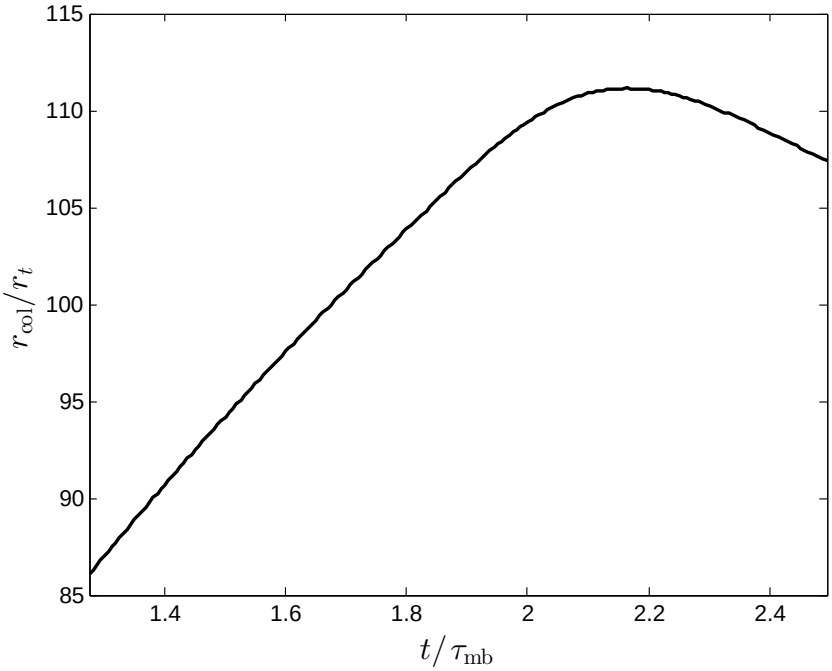

Figure 3.4: The radial distance $r_{\rm col}$ from the SBH where the self-intersections occur as a function of time t after disruption.

$t/\tau_{\rm mb} \approx 2.15$ the leading elements collide prior to apocenter passage, and the collision radii begin approaching the SBH. As the stream elements lose energy due to the collisions, their apocenters become smaller, which also leads to the collision smaller collision radii at later times. The deeper within the gravitational potential well that these self-intersections occur the more energy will be released because of the higher velocities involved in the collisions.

To determine the masses, we must identify which stream elements were involved in the self-intersections, which we show in Fig. 3.5 as a function of time. Given $S_{\alpha,\rm col}$ and $S_{\beta,\rm col}$, we solve the Lane-Emden equation to determine the differential mass dM_α/dS and dM_β/dS. A differential stream section dS_α and dS_β from each stream is involved during each collision, and so the masses of the stream elements involved are $dM_\alpha = dM_\alpha/dS \times dS_\alpha$ and $dM_\beta = dM_\beta/dS \times dS_\beta$. From Fig. 3.2 we see that the initial α stream masses are quite small compared to the β stream masses. From conservation of linear momentum in Eq. (3.6), the

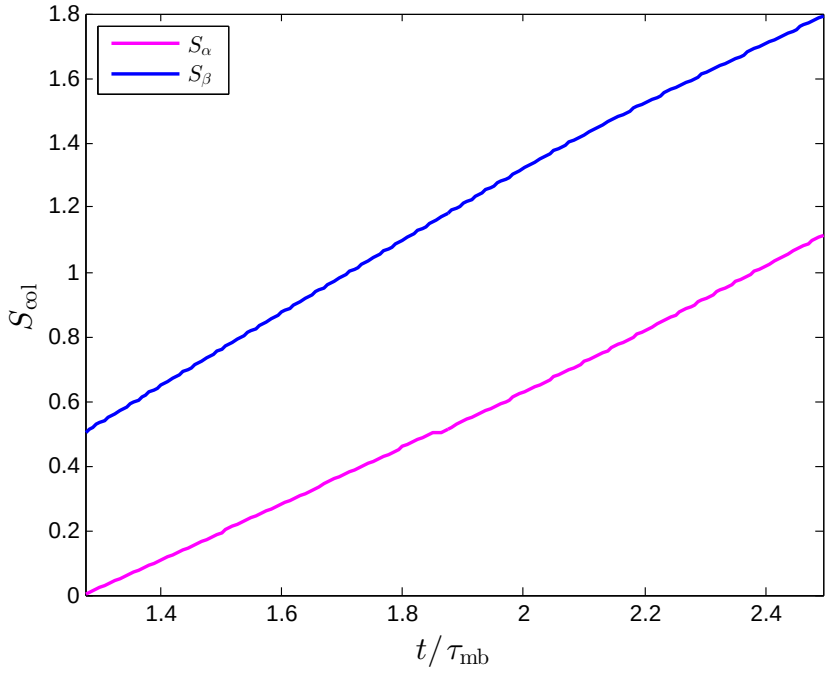

Figure 3.5: The S parameters for the stream elements α and β for the self-intersections as a function of time after disruption.

early collisions will be somewhat ineffective at dissipating energy within the stream. This may also apply to late times, as the α stream increases in mass with each collision and the β stream eventually falls off with power $-5/3$. Viscous dissipation comes into effect at these later times, however, so the stream, if not already so, could still be circularized. At time $t = \tau_{\rm mb}$, the luminosity for a circularized stream with energy $E = E_c$ would be,

$$\mathrm{L} = \frac{M_\odot E_c}{2\tau_{\rm mb}} = \frac{\sqrt{2}}{8\pi G}\left(\frac{GM_\odot}{R_\odot}\right)^{5/2}\left(\frac{M_\bullet}{M_\odot}\right)^{1/6} \tag{3.12a}$$

$$= 1.34\times10^{45}\left(\frac{M_\bullet}{10^6 M_\odot}\right)^{1/6}\ \mathrm{erg/s} = 1.07\times \mathrm{L_{Edd}}\left(\frac{\mathrm{M}_\bullet}{10^6\mathrm{M}_\odot}\right)^{1/6},$$

The inverse of the y-axis in Fig. 3.6 gives an estimate for how much longer the stream would take for the stream to circularize in units of $\tau_{\rm mb}$. While the current estimates are quite large,

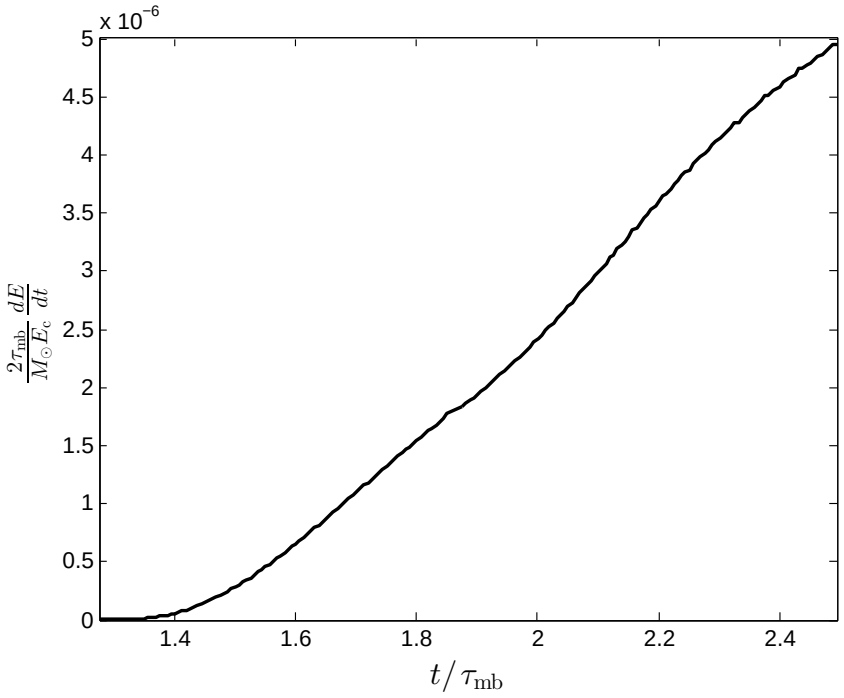

Figure 3.6: The power dissipated as a result of the inelastic collisions between stream elements as a function of time t after disruption. We scale this dE/dt by the power it would take to circularize the stream in a time $t = \tau_{\rm mb}$, equal to $E_c M_\odot/(2\tau_{\rm mb})$given expression Eq. 3.12.

at later times when the masses of the stream increase energy dissipation will increase and will lead to shorter times left until circularization.

Using Eqs. (3.6) and (3.7) we determine the change in energy, dE/dt, which we show in Fig. 3.6 as a function of time after disruption. This change in energy is given by,

$$\frac{dE}{dt} = \frac{1}{2}\left[\frac{dM_\alpha}{dt}\left(v_\alpha^2 - v_\gamma^2\right) + \frac{dM_\beta}{dt}\left(v_\beta^2 - v_\gamma^2\right)\right], \tag{3.13}$$

where dM_α/dt and dM_β/dt are the mass inflows from streams α and β, respectively. The rising mass of the α stream and the closer proximity of the collisions over time to the SBH contribute to the greater energy losses. We can also track the evolution of the energy distribution within the debris, which we show in Fig. 3.7. From Section (1.2) we know that

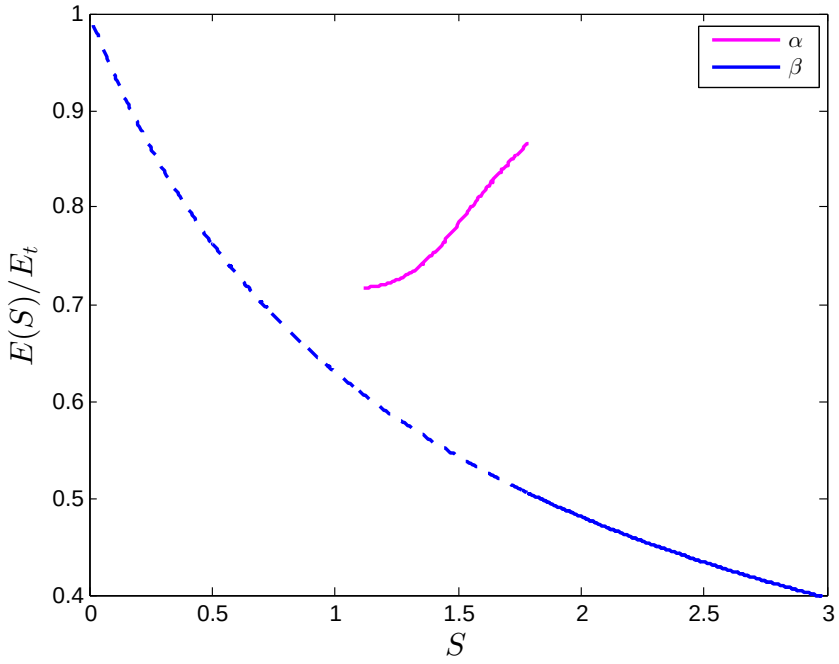

Figure 3.7: The binding energy distribution $E(S)$ at time $t = 2.5\tau_{\rm mb}$ after , where $\tau_{\rm mb}$ is the orbital period of the original most bound debris element corresponding to $S = 0$. The solid magenta curve represents the α stream, the solid blue curve represents the β stream, and the dashed blue curve represents the original α stream distribution prior to self intersection.

the radius of the eventual accretion disk will be $a_{\rm circ} = 2r_t$. As a ratio of E_t, the binding energy of the accretion disk is,

$$\frac{E_{\rm circ}}{E_t} = \frac{GM_\bullet/(4r_t)}{GM_\bullet R_\odot/r_t^2} = \frac{r_t}{4R_\odot} = \frac{1}{4}\left(\frac{M_\bullet}{M_\odot}\right)^{1/3}, \tag{3.14}$$

where we have used the relation $a_{\rm circ} = GM_\bullet/(2E_{\rm circ})$ relating the energy and semi major axis for the accretion disk. For a $10^6 M_\odot$ SBH, we have $E_{\rm circ}/E_t = 25$, and we would need to run our model until the energy distribution $E(S)/E_t = 25$ is achieved.

CHAPTER 4

TIDAL DISRUPTION IN KERR GEOMETRY

Our treatment of TDEs in Chapter 2 naturally motivates a generalization into the Kerr spacetime, but this is not without its own obstacles. In this chapter, we present unpublished work concerning TDE parameter thresholds and the remapping procedure for the penetration factor β for rotating SBHs.

4.1 Differences between the Schwarzschild and Kerr spacetimes

The Kerr metric (Kerr, 1963) in Boyer-Lindquist (BL) coordinates and in units of $G = c = 1$ is,

$$g^{\alpha\beta} = \begin{pmatrix} -\frac{A}{\Sigma\Delta} & 0 & 0 & -\frac{2M_\bullet ar}{\Sigma\Delta} \\ 0 & \frac{\Delta}{\Sigma} & 0 & 0 \\ 0 & 0 & \frac{1}{\Sigma} & 0 \\ -\frac{2M_\bullet ar}{\Sigma\Delta} & 0 & 0 & \frac{\Delta - a^2\sin\theta^2}{\Sigma\Delta\sin\theta^2} \end{pmatrix}$$

where $M_\bullet$ is the mass of the black hole, $a/M_\bullet$ is the dimensionless spin angular momentum of the black hole, and

$$\Sigma \equiv r^2 + a^2\cos^2\theta, \tag{4.1a}$$

$$\Delta \equiv r^2 + a^2 - 2M_\bullet r, \tag{4.1b}$$

$$A \equiv \left(r^2 + a^2\right)^2 - \Delta a^2 \sin^2\theta. \tag{4.1c}$$

The Schwarzschild metric, given by Eq. (2.10), is recovered by setting $a = 0$. The Kerr metric is axisymmetric, with the spin angular momentum of the SBH providing a well defined axis that is lacking in the Schwarzschild spacetime. This leads to a rather daunting expansion of

the parameter space for TDEs under the Kerr metric and raises the possibility that analytical expressions for our TDE parameter thresholds may no longer be available.

Test particles traveling on geodesics of the Kerr metric will have the three constants of motion,

$$E \equiv -g_{\alpha\beta}u^{\alpha}\left(\frac{\partial}{\partial t}\right)^{\beta}, \tag{4.2a}$$

$$L_z \equiv g_{\alpha\beta}u^{\alpha}\left(\frac{\partial}{\partial \phi}\right)^{\beta}, \tag{4.2b}$$

$$K \equiv K_{\alpha\beta}u^{\alpha}u^{\beta} \equiv Q + \left(L_z - aE\right)^2, \tag{4.2c}$$

where E is the orbital energy of the star (including its rest mass), L_z is the z-component of the star's angular momentum, u^{α} is the 4-velocity of the star, $\left(\frac{\partial}{\partial t}\right)^{\beta}$ and $\left(\frac{\partial}{\partial \phi}\right)^{\beta}$ are Killing vector fields (Wald, 1984) associated with E and L_z, respectively, K is the constant of motion associated with the Killing tensor $K_{\alpha\beta}$,

$$K_{\alpha\beta} = \Sigma\left(l_{\alpha}n_{\beta} + n_{\alpha}l\beta\right) + r^2 g_{\alpha\beta}, \tag{4.3a}$$

$$l^{\alpha} \equiv \frac{r^2 + a^2}{\Delta}\left(\frac{\partial}{\partial t}\right)^{\alpha}\frac{a}{\Delta}\left(\frac{\partial}{\partial \phi}\right)^{\alpha} + \left(\frac{\partial}{\partial r}\right)^{\alpha}, \tag{4.3b}$$

$$n^{\alpha} \equiv \frac{r^2 + a^2}{2\Sigma}\left(\frac{\partial}{\partial t}\right)^{\alpha}\frac{a}{2\Sigma}\left(\frac{\partial}{\partial \phi}\right)^{\alpha} - \frac{\Delta}{2\Sigma}\left(\frac{\partial}{\partial r}\right)^{\alpha}, \tag{4.3c}$$

n^{α} and l^{α} are the repeated principal null vectors found in the Petrov classification of the Weyl tensor (Wald, 1984), and Q is the Carter constant, which in the Newtonian limit reduces to $Q \to L_x^2 + L_y^2$. We can use the Carter constant to define the inclination

$$\cos\iota \equiv \frac{L_z}{\sqrt{Q + L_z^2}}, \tag{4.4}$$

which in the Newtonian limit reduces to the angle between the spin axis of the SBH and the orbital angular momentum of the star. The angle $\theta_{\rm p}$ in Fig. 4.1 is, in the Newtonian limit, between the radial vector pointing towards pericenter and the spin axis of the SBH.

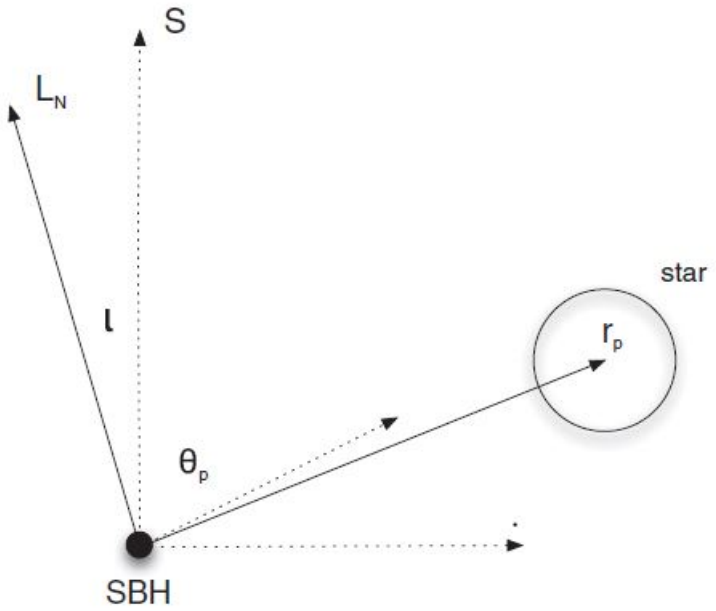

Figure 4.1: A diagram of the orientation of the disrupted star's orbit with respect to the SBH spin axis, where $r_{\rm p}$ is the pericenter of the star's orbit, $L_{\rm N}$ is the star's orbital angular momentum, and $\boldsymbol{S}$ points in the direction of the SBH spin. We also have the inclination angle ι between $\boldsymbol{L}_{\rm N}$ and $\boldsymbol{S}$ and the angle $\theta_{\rm p}$ between $\boldsymbol{r}_{\rm p}$ and $\boldsymbol{S}$. Figure adapted from (Kesden, 2012).

Comparing our parameter space under the Schwarzschild metric to that under the Kerr metric, we see that it has grown to,

$$\{M_\bullet, L, r\}_{\rm Schwarzschild} \longrightarrow \{M_\bullet, L_z, Q, r, \cos\theta, a\}_{\rm Kerr}. \tag{4.5}$$

We show in Fig. 4.1 the orientation of the above parameters with respect to one another under the Kerr metric.

4.2 Disruption thresholds under the Kerr metric

As discussed in Chapters 1 and 2 the tidal stresses experienced by a star are equal to the negative eigenvalue of the tidal tensor $C^{(i)}_{\ \ (j)}$. The negative eigenvalue, in BL coordinates, was $-2\left(1+3L^2/(2r^2)\right)M_\bullet/r^3$ under the Schwarzschild metric. There is no equivalent analytic

expression for this eigenvalue in Kerr spacetime, and we must instead rely on numerical solutions. In what follows we calculate the tidal forces at pericenter $r = r_{\rm p}$ and hold one of either the orbital angular momentum of the star, L, or the spin angular momentum of the SBH, a, fixed. We then solve for the negative eigenvalue as a function of $\cos\iota$ and $\cos\theta_p$ (the value of $\cos\theta$ at pericenter), which we show in Fig. 4.2 for a maximally rotating SBH at $a/M_\bullet = 1$. The blue region outside the of the "diamond" is unphysical, as the inclination ι and coordinate angle θ_p must satisfy the relation,

$$\frac{\pi}{2} - \iota \leq \theta_p \leq \frac{\pi}{2} + \iota, \iota < \frac{\pi}{2} \tag{4.6a}$$

$$\iota - \frac{\pi}{2} \leq \theta_p \leq \frac{3\pi}{2} - \iota, \iota > \frac{\pi}{2}. \tag{4.6b}$$

The dark blue region within the white diamond in the bottom two panels of Fig. 4.2 corresponds to direct capture by the SBH event horizon, within which there is no well defined pericenter coordinate and thus no numerical soultions to determine. Unlike under the Schwarzschild spacetime the capture threshold is no longer fixed at $L_{\rm cap} = 4M_\bullet$ and instead depends on the inclination angle ι and the SBH spin angular momentum a (Bardeen, Press, and Teukolsky, 1972). We show this dependence as a function of $\cos\iota$ for various SBH spin angular momenta in Fig. 4.3. Inclinations of $\cos\iota = 1$ and $\cos\iota = -1$ correspond to equatorial prograde and retrograde orbits, respectively.

Under the Schwarzschild spacetime the orbital angular momentum L and radial coordinate r were enough to determine the tidal stresses, whereas under the Kerr spacetime it is now possible to have two stars with the same orbital angular momentum at the same radial coordinate experience entirely different tides if they approach from different directions with respect to the SBH spin axis. Our remapping procedure for the β parameter becomes significantly more complex, and so it would behoove us to find a way to reduce the size of our parameter space. Note the weak dependence on $\cos\theta_p$ for the tidal forces in Fig. 4.2. We

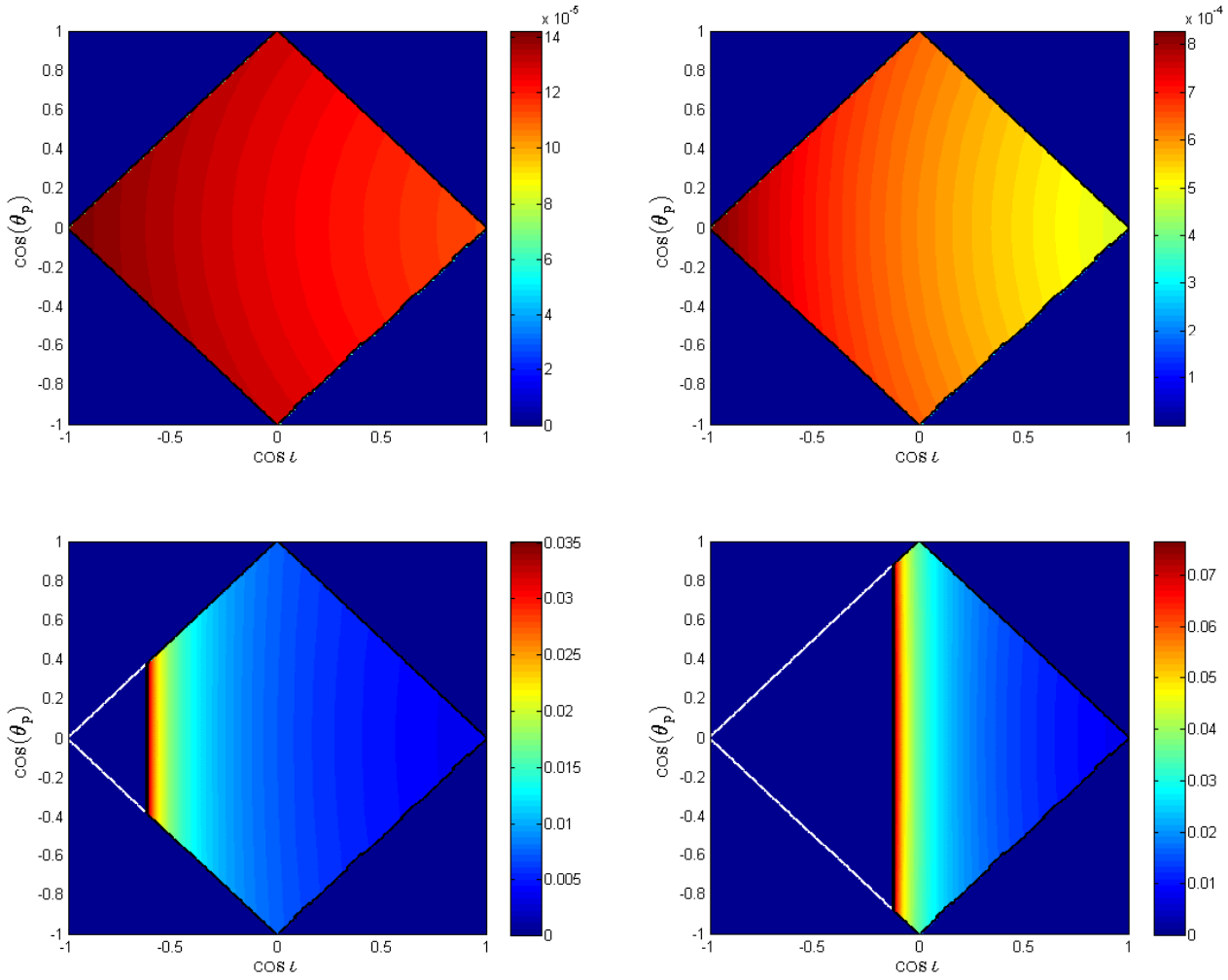

Figure 4.2: The negative eigenvalue, $M_\bullet^2\lambda_-$, of the tidal tensor $C^{(i)}_{\ \ (j)}$, in units of $G = c = 1$ under the Kerr metric for a maximally rotating SBH. The top-right, top-left, bottom-right and bottom-left panels correspond to stars with orbital angular momenta of $L/M_\bullet = 7.5$, $L/M_\bullet = 6.0$, $L/M_\bullet = 4.5$, and $L/M_\bullet = 4.0$, respectively.

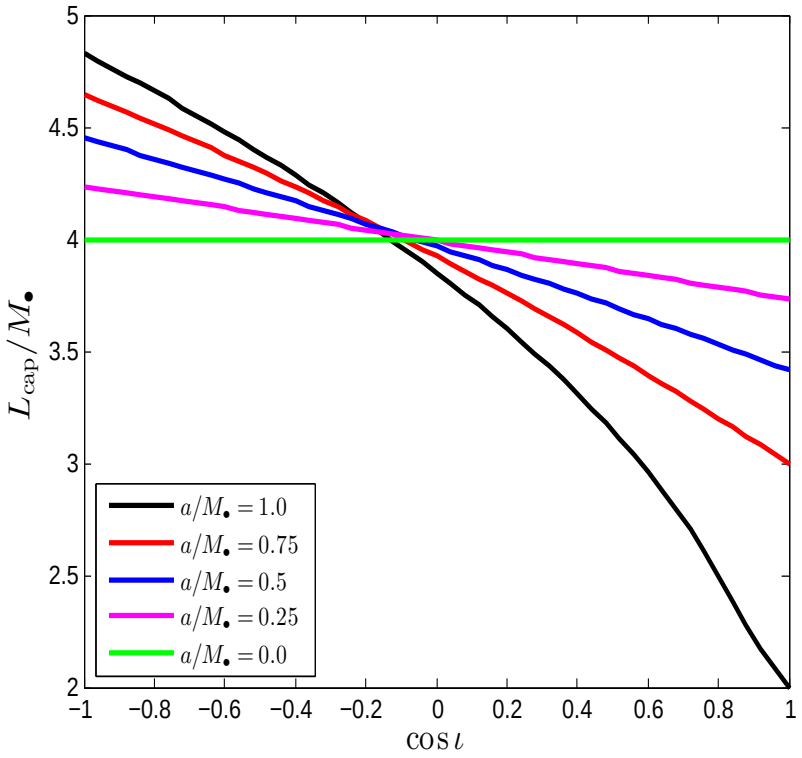

Figure 4.3: The angular momentum capture threshold under Kerr geometry for various SBH spin angular momenta, a, as a function of the inclination angle ι.

now determine how weak this dependence on $\theta_{\rm p}$ is, and whether are not we can average it out of our remapping procedure.

Recall that we defined the penetration factor β as,

$$\beta = \frac{L_t^2}{L^2}, \tag{4.7}$$

where L_t is as defined in Eq. (2.2). The tidal stresses experienced by the star at pericenter under Newtonian gravity was given as $\lambda_- = (2M_\bullet/L_N^2)^3$. For $\beta = 1$ and for a given SBH mass, we can numerically determine, as a function of $\cos\iota$ and $\cos\theta_{\rm p}$ the orbital angular momentum $L_d(\iota, \theta_{\rm p})$ a star would need to be disrupted in the Kerr spacetime. To determine the strength of the dependence on $\cos\theta_{\rm p}$, we average this L_d over $\cos\theta_{\rm p}$ as follows,

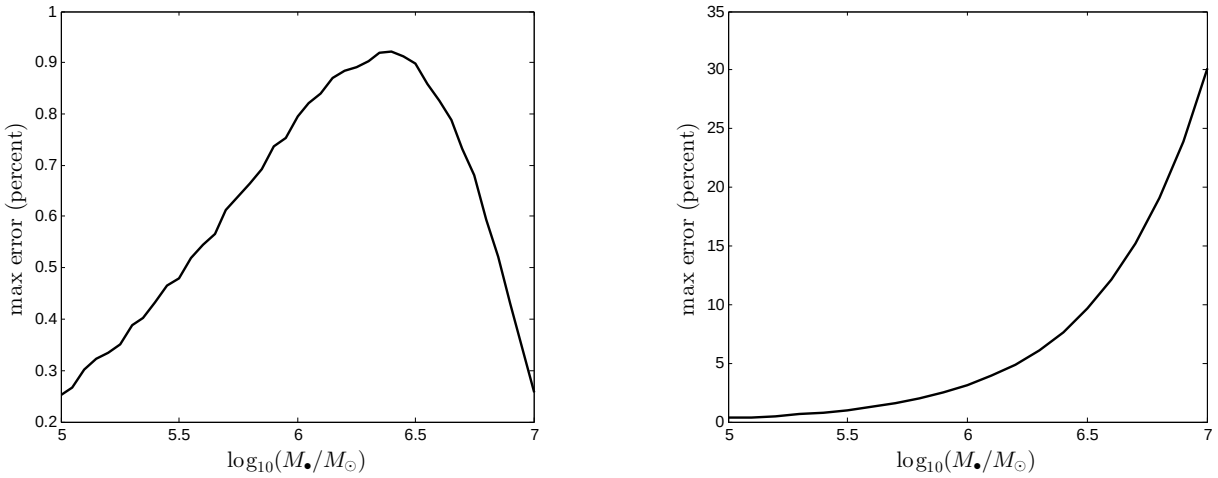

Figure 4.4: The error in averaging the remapped angular momentum threshold for disruption, $L_{\rm d}$, over $\cos\theta_p$ (left) and $\cos\iota$ (right).

$$\overline{L}_d(\cos\iota) = \frac{1}{2\pi}\int_0^{2\pi} L_d(\cos\iota, \cos\omega\sin\iota)d\omega, \tag{4.8}$$

where we have made the change of variable to the argument of pericenter ω via $\cos\theta_{\rm p} = \cos\omega\sin\iota$, which is consistent with Eq. (4.6). Comparing the averages $\overline{L}_d$ to the actual L_d would give us the error in averaging over $\theta_{\rm p}$, which we define as,

$$Error(\iota, \theta_{\rm p}) = \frac{|L_d(\iota, \theta_{\rm p}) - \overline{L}_d(\iota)|}{L_d(\iota, \theta_{\rm p})}. \tag{4.9}$$

Although this error is a function of ι and θ_p, we can determine the maximum error for any ι or $\theta_{\rm p}$, which we show on the left panel of Fig. 4.4. The largest error in averaging over $\cos\theta_{\rm p}$ does not surpass even 1%, and we may thus remove it from our parameter space to high accuracy.

We can also average over ι as follows,

$$\overline{\overline{L}}_d = \frac{1}{2}\int_{-1}^{1} \overline{L}_d(\cos\iota)d(\cos\iota). \tag{4.10}$$

This is actually a doubly averaged L_d, but this is valid as the $\theta_{\rm p}$ depdence has been shown to be weak. The error for this particular averaging is given by,

$$Error2(\iota, \theta_{\rm p}) = \frac{|L_d(\iota, \theta_{\rm p}) - \overline{\overline{L}}_d(\iota)|}{L_d(\iota, \theta_{\rm p})}. \tag{4.11}$$

For the averaging over ι, it is unsurprising to see vanishing error for the lower end of the SBH masses, which we see in the right panel of Fig. 4.4, as rotations have no effect on gravity in the Newtonian limit. For masses greater than $10^6 M_\odot$, however, our errors quickly rise, and we must thus keep the ι dependence in our remappings.

4.3 The remapping of β in Kerr spacetime

As we did in Chapter 2 we now remap orbital parameters in Newtonian gravity to their counterparts under relativity that yield the same tidal stresses at pericenter, except this time using the Kerr metric. We still define the penetration factor as in Eq. (2.22). Recall that under Schwarzschild geometry our remapping procedure involved solving for the angular momentum L in Eq. (2.21) that yielded the same tidal stresses as under Newtonian gravity. The Kerr metric includes the inclination angle, ι, the SBH spin angular momentum, a, and the angle $\theta_{\rm p}$ to our parameter space, although we showed in the previous section that we may average out the latter to high accuracy.

In Fig. 4.5, we show for a $10^7 M_\odot$ mass SBH the remapping of β_d for equitorial orbits using various dimensionless SBH spin angular momenta $\chi = a/M_\bullet$. The ends of the curves correspond to direct capture, which show that while retrograde orbits, ceteris paribus, experience stronger tides than prograde orbits they are more prone to capture. These prograde orbits for large SBH spins are also able to penetrate deeper than their Schwarzschild ($a = 0$) counterparts, which would likely extend the maximum possible SBH mass observable via TDEs. This also suggests, however, that TDE observations would be skewed towards prograde orbits at higher SBH masses. Note that all remapped curves lie above the black dashed

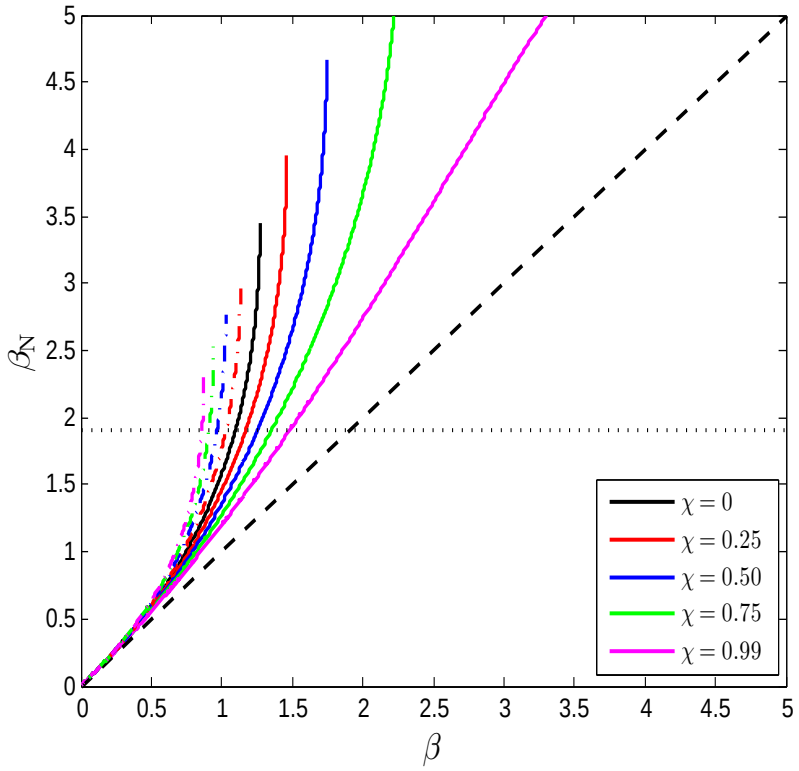

Figure 4.5: The remapping of the penetration factor under Newtonian gravity β_N to under Kerr geometry β for various SBH spin angular momenta $\chi = a/M_\bullet$ for a $M_\bullet = 10^7 M_\odot$ SBH. The solid curves represent prograde equatorial orbits with $\cos\iota = 1$ and the dot-dashed curves retrograde equatorial orbitswith $\cos\iota = -1$. The ends of the curves correspond to direct capture by the SBH. The black dashed curve shows a one-to-one relation and is added to emphasize that tides under relativity are always stronger than under Newtonian gravity.

curve, representing a one-to-one relation, which emphasizes that tides under GR are always stronger than under Newtonian gravity.

CHAPTER 5

CONCLUSION

Tidal disruption events are observationally interesting for because they grant us the possibility of probing the spacetime near the vicinity of the black hole event horizon, where spacetime curvature is at its most extreme. They also provide the opportunity of studying otherwise quiescent black holes, granting astronomers another means of studying galactic centers.

The stronger tides under GR mean that stars do not need to penetrate as deeply into the gravitational potential well of the SBH as Newtonian gravity would imply. Mapping Keplerian orbits to their corresponding geodesics under general relativity grants us a means of applying relativistic corrections to Newtonian hydrodynamical simulations without needing to directly solve the Einstein field equations, which can be computationally expensive. We have found that relativistic effects lead to an exponential suppression of the TDE rate at higher SBH masses, in agreement with previous estimates in the loss-cone regime (Stone and Metzger, 2016). We applied our mapping procedure to recent hydrodynamical simulations (Guillochon and Ramirez-Ruiz, 2013) and found that relativistic corrections to the width of the binding energy distribution within tidal debris would lead to lower fallback accretion rates and potentially dimmer TDE flares.

We also presented a new model for tracking the evolution of the bound debris after disruption. Instead of approximating the tidal debris with a single orbit, we parameterize the stream based on their orbital periods and trace the behavior of the stream overall. We found that approxiating the stream with a single orbit can potentially mischaracterize predictions for the observed TDE flare brightness due to errors in the predicted collision radii and stream masses. We did find, however, that for very large SBH masses the single orbit model can be a decent approximation for stream collisions due to the extreme amounts of precession per pericenter passage.

Finally, we generalized our remapping procedure in Chapter 2 from the Schwarzschild to the Kerr spacetime and found that TDE observations could likely be skewed towards prograde orbits for high SBH spins. This does grant the possibility, however, of observing TDEs for larger SBH masses than Schwarzschild predictions might suggest. In every case we find that tides under GR are stronger than under Newtonian gravity, emphasizing the importance of Einstein's groundbreaking theory to yet another natural phenomenon.

APPENDIX

THE S PARAMETERIZATION OF TDE STREAMS

Here we define the S variable used in Chapter 3 to parameterize the tidal stream. Let S be defined as follows,

$$S \equiv \frac{\tau}{\tau_{\rm mb}} - 1, \tag{A.1}$$

where τ is the orbital period of a stream element and $\tau_{\rm mb}$ is the orbital period of the most bound debris element. Binning the stream based on their orbital periods is advantageous during numerical calculations as it prevents the stream particle positions from becoming too spread out.

The binding energy E and orbital period of an object orbiting a mass $M_\bullet$ are related by,

$$\tau = 2\pi \frac{GM_\bullet}{(2E)^{3/2}} \tag{A.2}$$

where G is Newton's constant. If R is the radial distance from the center of the star where a stream element was located pre-disruption, then the energy distribution as a function of this R is,

$$E(R) = \frac{E_t R}{R_\odot}, \tag{A.3}$$

where E_t is the binding energy of the most bound stream element and $R_\odot$ is the solar radius. Inserting Eq. (A.3) into Eq. (A.2) yields,

$$\tau = 2\pi \frac{GM_\bullet}{(2E_t)^{3/2}} \left(\frac{R}{R_\odot}\right)^{-3/2}. \tag{A.4}$$

For the most bound stream element with binding energy E_t, we have $\tau_{\rm mb} = 2\pi GM_\bullet/(2E_t)^{3/2}$. Thus, we can relate our new S parameter to R using Eq. A.1,

$$S \equiv \frac{\tau}{\tau_{\rm mb}} - 1 = \left(\frac{R}{R_\odot}\right)^{-3/2} - 1. \tag{A.5}$$

Given that the orbital parameters of the stream are given as functions of R, with Eq. (A.5) we can now rebin them as a function of S,

$$E(S) = E_t\,(1+S)^{-2/3}\,, \tag{A.6a}$$

$$L(S) = L_t\left(1 - \frac{R_\odot}{r_t}\,(1+S)^{-2/3}\right), \tag{A.6b}$$

$$a(S) = \frac{-M_\bullet}{2E(S)} = -\frac{M_\bullet}{2E_t}\,(1+S)^{2/3}\,, \tag{A.6c}$$

$$e(S) = \sqrt{1 - 2E(S)\frac{L^2(S)}{M_\bullet^2}} = \sqrt{1 - \frac{2E_tL_t^2}{M_\bullet^2}\,(1+S)^{-2/3}\left(1 - \frac{R_\odot}{r_t}\,(1+S)^{-2/3}\right)}. \tag{A.6d}$$

REFERENCES

Abbott, B. P. et al. *Observation of gravitational waves from a binary black hole merger*. PRL, 116, 061102, 2016.

Arcavi, I. et al. *A continuum of H- to He-rich tidal disruption candidates with a preference for E+A galaxies*. Astrophys. J., 793, 38, 2014.

Bade, N., S. Komossa, and M. Dahlem. *Detection of an extremely soft X-ray outburst in the HII-like nucleus of NGC 5905*. Astron. Astrophys., 309, L35, 1996.

Bahcall, J. N. and R. A. Wolf. *Star distribution around a massive black hole in a globular cluster*. Astrophys. J., 209, 214, 1976.

Bardeen, J. M., W. H. Press, S. A. Teukolsky. *Rotating black holes: locally nonrotating frames, energy extraction, and scalar synchrotron radiation*. Astrophys. J., 178:347-369, 1972.

Binney, J., S. Tremaine. *Galactic Dynamics*. (Princeton University Press, Princeton, NJ, 2008), ISBN 978-0-691-13027-9.

Bloom, J. S. et al. *A Possible Relativistic Jetted Outburst from a Massive Black Hole Fed by a Tidally Disrupted Star*. Science, 333, 203, 2011.

Bonnerot, C., E. M. Rossi, G. Lodato, and D. J. Price. *Disc formation from tidal disruptions of stars on eccentric orbits by Schwarzschild black holes*. MNRAS, 455, 2253, 2016.

Bonnerot, C., E. M. Rossi, and G. Lodato. *Long-term stream evolution in tidal disruption events*. MNRAS, 464:2816-2830, 2016.

Boyer, R. H. and R. W. Lindquist. *Maximal Analytic Extension of the Kerr Metric*. J. Math. Phys. (N.Y.), 8, 265, 1967.

Brassart, M. and J.-P. Luminet. *Shock waves in tidally compressed stars by massive black holes*. Astron. Astrophys., 481, 259, 2008.

Burrows, D. N. et al. *Relativistic jet activity from the tidal disruption of a star by a massive black hole*. Nature (London), 476, 421, 2011.

Carter, B. *Global structure of the Kerr Family of Gravitational Fields*. Phys. Rev., 174, 1559, 1968.

Carter, B., and J. P. Luminet. *Tidal compression of a star by a large black hole*. Astron. Astrophys., 121, 97-113, 1983.

Cenko, S. B. et al. *PTF10iya: a short-lived, luminous flare from the nuclear region of a star-forming galaxy*. MNRAS, 420:2684-2699, 2012.

Cenko, S. B. et al. *SWIFT J2058.4+0516: Discovery of a possible second relativistic tidal disruption flare?*. Astrophys. J., 753, 77, 2012.

Chandrasekhar, S. *Dynamical Friction. I. General Considerations: the Coefficient of Dynamical Friction*. Astrophys. J., 97, 255, 1943.

Chandrasekhar, S. *Dynamical Friction. II. The Rate of Escape of Stars from Clusters and the Evidence for the Operation of Dynamical Friction*. Astrophys. J., 97, 263, 1943.

Chandrasekhar, S. *Dynamical Friction. III. a More Exact Theory of the Rate of Escape of Stars from Clusters*. Astrophys. J., 98, 54, 1943.

Cheng, R. M. and C. R. Evans. *Relativistic effects in the tidal interaction between a white dwarf and a massive black hole in Fermi normal coordinates*. Phys. Rev. D, 87, 104010, 2013.

Cheng, R. M. and T. Bogdanović. *Tidal disruption of a star in the Schwarzschild spacetime: Relativistic effects in the return rate of debris*. Phys. Rev. D, 90, 064020, 2014.

Chornock, R. et al. *The ultrviolet-bright, slowly declining trannsient PS1-11af as a partial tidal disruption event*. Astrophys. J., 780, 44, 2014.

Cohn, H. and R. M. Kulsrud. *The stellar distribution around a black hole - Numerical integration of the Fokker-Planck equation*. Astrophys. J., 226, 1087, 1978.

Dai, L., A. Escala, and P. Coppi. *The impact of bound stellar orbits and general relativity on the temporal behavior of tidal disruption flares*. Astrophys. J. Lett., 775, L9, 2013.

Dai, L., J. C. McKinney, and M. C. Miller. *Soft X-ray tidal disruption events from stars on deep plunging orbits*. Astrophys. J. Lett., 812, L39, 2015.

Diener, P., V. P. Frolov, A. M. Khokhlov, I. D. Novikov, and C. J. Pethick. *Relativistic Tidal Interaction of Stars with a Rotating Black Hole*. Astrophys. J., 479, 164, 1997.

Donley, J. L., W.N . Brandt, M. Eracleous, and T. Boller. *Large-Amplitude X-Ray Outbursts from Galactic Nuclei: A Systematic Survey using ROSAT Archival Data*. Astron. J., 124, 1308, 2002.

Esquej, P. et al. *Evolution of tidal disruption candidates discovered by XMM-Newton*. Astron. Astrophys., 489, 543, 2008.

Evans, C. R., and C. S. Kochanek. *The tidal disruption of a star by a massive black hole*. Astrophys. J., 346, L13, 1989.

Ferrarese, L. and D. Merritt. *A Fundamental Relation between Supermassive Black Holes and Their Host Galaxies*. Astrophys. J., 539, L9, 2000.

French, K. D., I. Arcavi, and A. Zabludoff. *Tidal disruption events prefer unusual host galaxies*. Astrophys. J., 818, L21, 2016.

Frank, J. and M. J. Rees. *Effects of Massive Central Black Holes on Dense Stellar Systems*. MNRAS, 176, 633, 1976.

Gebhardt, K., R. Bender, G. Bower, A. Dressler, S. M. Faber, A. V. Filippenko, R. Green, C. Grillmair, L. C. Ho, J. Kormendy, T. R. Lauer, J. Magorrian, J. Pinkney, D. Richstone, and S. Tremaine. *A Relationship between Nuclear Black Hole Mass and Galaxy Velocity Dispersion*. Astrophys. J. Lett., 539, L13, 2000.

Genzel, R., N. Thatte, A. Krabbe, H. Kroker, and L. E. Taconni-Garman. *The dark mass concentration in the central parsec of the Milky Way*. Astrophys. J., 472:153-172, 1996.

Gezari, S. et al. *An ultravioletoptical flare from the tidal disruption of a helium-rich stellar core*. Nature (London), 485, 217, 2012.

Gezari, S. et al. *Ultraviolet Detection of the Tidal Disruption of a Star by a Supermassive Black Hole*. Astrophys. J., 653, L25, 2006.

Gezari, S. et al. *UV/Optical Detections of Candidate Tidal Disruption Events by GALEX and CFHTLS*. Astrophys. J., 676:944-969, 2008.

Gezari, S. et al. *Luminous thermal flares from quiescent supermassive black holes*. Astrophys. J., 698, 1367, 2009.

Grupe, D., H.-C. Thomas, and K. M. Leighly. *RX J1624.9+7554: a new X-ray transient AGN*. Astron. Astrophys., 350, L31, 1999.

Guillochon, J. and E. Ramirez-Ruiz. *Hydrodynamical simulations to determine the feeding rate of black holes by the tidal disruption of stars: the importance of the impact parameter and stellar structure*. Astrophys. J., 767, 25, 2013.

Guillochon, J., E. Ramirez-Ruiz, S. Rosswog, and D. Kasen. *Three-dimensional simulations of tidally disrupted solar-type stars and the observational signatures of shock breakout*. Astrophys. J., 705, 844, 2009.

Guillochon, J. and E. Ramirez-Ruiz. *A dark year for tidal disruption events*. Astrophys. J., 809, 166, 2015.

Guillochon, J., H. Manukian, and E. Ramirez-Ruiz. *PS1-10jh: the disruption of a main-sequence star of near-solar composition*. Astrophys. J., 783, 23, 2014.

Haas, R., R. V. Shcherbakov, T. Bode, and P. Laguna. *Tidal disruptions of white dwarfs from ultra-close encounters with intermediate-mass spinning black holes*. Astrophys. J., 749, 117, 2012.

Hayasaki, K., N. Stone, and A. Loeb. *Circularization of tidally disrupted stars around spinning supermassive black holes*. MNRAS, 461, 3760, 2016.

Hayasaki, K., N. Stone, and A. Loeb. *Finite, intense accretion bursts from tidal disruption of stars on bound orbits*. MNRAS, 434, 909, 2013.

Heger, A., C. L. Fryer, S. E. Woosley, N. Langer, D. H. Hartmann. *How massive single stars end their life*. Astrophys. J., 591:288-300, 2003.

Hills, J. G. *Possible power source of Seyfert galaxies and QSOs*. Nature, 254:295-298, 1975.

Holoein, T. W. -S. et al. *ASASSN-14ae: A tidal disruption event at 200 Mpc*. MNRAS, 445:3263-3277, 2014.

Hung, T., S. Gezari, N. Blagorodnova, N. Roth, S. B. Cenko, S. R. Kulkarni, A. Horesh, I. Arcavi, C. McCully, L. Yan, R. Lunnan, C. Fremling, Y. Cao, P. E. Nugent, and P. Wozniak. *Revisiting Optical Tidal Disruption Events with iPTF16axa*. Astrophys. J., 842, 29, 2017.

Ivanov, P. B., M. A. Chernyakova, and I. D. Novikov. *The new model of a tidally disrupted star: further development and relativistic calculations*. MNRAS, 338, 147, 2003.

Ivanov, P. B. and M. A. Chernyakova. *Relativistic cross sections of mass stripping and tidal disruption of a star by a super-massive rotating black hole*. Astron. Astrophys., 448, 843, 2006.

Kauffman, G., T. M. Heckman, C. Tremonti, J. Brinchmann, S. Charlot, S. D. M. White, S. E. Ridgway, J. Brinkmann, M. Fukugita, P.B. Hall, Ž. Ivezić, G. T. Richards, and D. P. Schneider. *The host galaxies of active galactic nuclei*. MNRAS, 346:1055-1077, 2003.

Kerr, R. P. *Gravitational Field of a Spinning Mass as an Example of Algebraically Special Metrics*. Phys. Rev. Lett., 11, 237, 1963.

Kesden, M. *Tidal-disruption rate of stars by spinning supermassive black holes*. Phys. Rev. D, 85, 024037, 2012.

Kesden, M. *Black-hole spin dependence in the light curves of tidal disruption events*. Phys. Rev. D, 86, 064026, 2012.

Kobayashi, S., P. Laguna, E. S. Phinney, and P. Mészáros. *Gravitational Waves and X-Ray Signals from Stellar Disruption by a Massive Black Hole*. Astrophys. J., 615, 855, 2004.

Kochanek, C. S. *The aftermath of tidal disruption: The dynamics of thin gas streams*. Astrophys. J., 422, 508, 1994.

Komossa, S. and N. Bade. *The giant X-ray outbursts in NGC 5905 and IC 3599: following up observations and outburst scenarios*. Astron. Astrophys., 343, 775, 1999.

Kormendy, J., and D. Richstone. *Inward bound - the search for supermassive black holes in galactic nuclei*. Annu. Rev. Astron. Astrophys., 33:581-624, 1995.

Laguna, P., W. A. Miller, W. H. Zurek, and M. B. Davies. *Tidal disruptions by supermassive black holes - Hydrodynamic evolution of stars on a Schwarzschild background*. Astrophys. J. Lett., 410, L83, 1993.

Lauer, T. R., S. M. Faber, K. Gebhardt, D. Richstone, S. Tremaine, E. A. Ajhar, M. C. Aller, R. Bender, A. Dressler, A. V. Filippenko, R. Green, C. J. Grillmair, L. C. Ho, J. Kormendy, J. Magorrian, J. Pinkney, and C. Siopis. *The Centers of Early-Type Galaxies with Hubble Space Telescope. V. New WFPC2 Photometry*. Astron. J., 129, 2138, 2005.

Lodato, G., A. R. King, and J. E. Pringle. *Stellar disruption by a supermassive black hole: is the light curve really proportional to $t^{-5/3}$?*. MNRAS, 392:332-340, 2009.

Luminet, J. P. and J. A. Marck. *Tidal squeezing of stars by Schwarzschild black holes*. MNRAS, 212, 57, 1985.

Luminet, J. P. and J. A. Marck. *General Relativity and Gravitation*, edited by B. Bertotti, F. de Felice, and A. Pascolini (Consiglio Nazionale delle Ricerche, Rome, 1983), Vol. 1, p. 438.

Luminet, J. P. and B. Carter. *Dynamics of an affine star model in a black hole tidal field*. Astrophys. J., 61, 219-248, 1986.

MacLeod, M., J. Guillochon, and E. Ramirez-Ruiz. *The tidal disruption of giant stars and their contribution to the flaring supermassive black hole population*. Astrophys. J., 757, 134, 2012.

Magorrian, J., and S. Tremaine. *Rates of tidal disruption of stars by massive central black holes*. MNRAS, 309, 447, 1999.

Magorrian, J., S. Tremaine, D. Richstone, R. Bender, G. Bower, A. Dressler, S. M. Faber, K. Gebhardt, R. Green, C. Grillmair, J. Kormendy, and T. Lauer. *The demography of massive dark objects in galaxy centers*.

Manasse, F. K and C. W. Misner. *Fermi Normal Coordinates and Some Basic Concepts in Differential Geometry*. J. Math. Phys. (N.Y.), 4, 735, 1963.

Maksym, W. P., M. P. Ulmer, and M. Eracleous. *A tidal disruption flare in A1689 from an archival X-ray survey of galaxy clusters*. Astrophys. J., 722, 1035, 2010.

Merritt, D. *Dynamics and Evolution of Galactic Nuclei*. (Princeton University Press, Princeton, NJ, 2013), ISBN 978-0-691-15860-0.

Merritt, D. *Loss-cone dynamics*. Classical and Quantum Gravity, 30, 244005, 2013.

Pasham, D. R., S. .B. Cenko, A. Sadowski, J. Guillochon, N. C. Stone, S. van Velzen, and J. K. Cannizzo. *Disk formation versus disk accretion - what powers tidal disruption events?*. Astrophys. J., 837:L30, 2017.

Peebles, P. J. E. *Star Distribution Near a Collapsed Object*. Astrophys. J., 178, 371, 1972.

Piran, T., G. Svirski, J. Krolik, R. M. Cheng, and H. Shiokawa. *Disk formation versus disk accretion - what powers tidal disruption events?*. Astrophys. J., 806:164, 2015.

Pringle, J. E. *Accretion discs in astrophysics*. Annu. Rev. Astron. Astrophys., 19:137-62, 1972.

Rees, M. J. *Tidal disruption of stars by black holes of* $10^6 - 10^8$ *solar masses in nearby galaxies*. Nature (London), 333, 523, 1988.

Saxton, R. D., A. M. Read, P. Esquej, S. Komossa, S. Dougherty, P. Rodriguez-Pascual, and D. Barrado. *A tidal disruption-like X-ray flare from the quiescent galaxy SDSS J120136.02+300305.5*. Astron. Astrophys., 541, A106, 2012.

Sądowski, A., E. Tejeda, E. Gafton, S. Rosswog, and D. Abarca. *Magnetohydrodynamical simulations of a deep tidal disruption in general relativity*. MNRAS, 458, 4250, 2016.

Schmidt, M. *3C 273: A star-like object with large red-shift*. Nature, 197, 1040, 1963.

Schwarzschild, K. Sitzungsberichte der Kniglich Preußischen Akademie der Wissenschaften (Berlin), 1916, 189, 1916.

Servin, J. and M. Kesden. *Unified treatment of tidal disruption by Schwarzschild black holes*. Phys. Rev. D, 95, 083001, 2017.

Shakura, N. I. and R. A. Sunyaev. *Black Holes in Binary Systems. Observational Appearance*. Astron. Astrophys., 24, 337-355, 1973.

Shiokawa, H., J. H. Krolik, R. M. Cheng, T. Piran, and S. C. Noble. *General relativistic hydrodynamical simulation of accretion flow from a stellar tidal disruption*. Astrophys. J., 804, 85, 2015.

Spitzer, L. and M. H. Hart. *Random Gravitational Encounters and the Evolution of Spherical Systems. I. Method*. Astrophys. J., 164, 399, 1971.

Stern, D. et al. *Discovery of a Transient U-Band Dropout in a Lyman Break Survey: A Tidally Disrupted Star at z = 3.3?*. Astrophys. J., 612, 690, 2004.

Stone, N. C. and B. D. Metzger. *Rates of stellar tidal disruption as probes of the supermassive black hole mass function*. MNRAS, 455, 859, 2016.

Stone, N. C. and S. van Velzen. *An enhanced rate of tidal disruptions in the centrally overdense E+A galaxy NGC 3156*. Astrophys. J. Lett., 825, L14, 2016.

Stone, N. C., M. Kesden, R. M. Cheng, S. van Velzen *Stellar disruption events in general relativity*. arXiv:1801.10180, 2018.

Stone, N. C., R. Sari, and A. Loeb. *Consequences of strong compression in tidal disruption events*. MNRAS, 435, 1809, 2013.

van Velzen, S., G. R. Farrar, S. Gezari, N. Morrell, D. Zaritsky, L. Östman, M. Smith, J. Gelfand, and A. J. Drake. *Optical discovery of probable stellar tidal disruption flares*. Astrophys. J., 741, 73, 2011.

Vinkó, J., F. Yuan, R. M. Quimby, J. C. Wheeler, E. Ramirez-Ruiz, J. Guillochon, E. Chatzopoulos, G. H. Marion, and C. Akerlof. *A luminous, fast rising UV-transient discovered by ROTSE: a tidal disruption event?*. Astrophys. J., 798, 12, 2015. Astron. J., 115:2285-2305, 1998.

Volonteri, M. *Formation of supermassive black holes*. Astron. Astrophys. Rev., 18:279-315, 2010.

Wald, R. M. *General Relativity*. University of Chicago Press, 1984

Wang, T.-G., H.-Y. Zhou, S. Komossa, H.-Y. Wang, W. Yuan, and C. Yang. *Extreme coronal light emitters: tidal disruption of stars by massive black holes in galactic nuclei?*. Astrophys. J., 749, 115, 2012.

Wang, J. and D. Merritt. *Revised Rates of Stellar Disruption in Galactic Nuclei*. Astrophys. J., 600, 149-161, 2004.

Weisskopf, M. C., M. Guainazzi, K. Jahoda, N. Shaposhnikov, S. L. O'Dell, V. E. Zavlin, C. Wilson-Hodge. *On calibrations using the crab nebula and models of the nebular x-ray emission*. Astrophys. J., 713:912-919, 2010.

Young, P. J., G. A. Shields, and J. C. Wheller. *The black tide model of QSOs*. Astrophys. J., 212, 367, 1977.

BIOGRAPHICAL SKETCH

Juan E. Servin began his undergraduate studies in Physics at The University of Texas at Dallas in the Fall of 2010. He then entered the graduate program at UTD in the Spring of 2014, and began his research with Michael Kesden a year later in the Spring of 2015. This research involved applying relativistic corrections to the astrophysical phenomenon known as tidal disruption events, eventually leading to a peer reviewed publication. Juan is the eldest son of a proud immigrant family from Guanajuato, Mexico. He was born and raised in Dallas, and will be the first in his family to graduate with a doctorate degree.

CURRICULUM VITAE

Juan E. Servin

June 21, 2018

Contact Information:

Department of Physics
The University of Texas at Dallas
800 W. Campbell Rd.
Dallas, TX 75208, U.S.A.

Voice: (214) 434-6125
Email: jes105020@utdallas.edu

Educational History:

B.S., Physics, University of Texas at Dallas, 2013
M.S., Physics, University of Texas at Dallas, 2016
Ph.D., Physics, University of Texas at Dallas, 2018

A unified relativistic treatment of tidal disruption events and a new model for self-intersections involving tidal debris streams for Schwarzschild black holes
Ph.D. Dissertation
Department of Physics, University of Texas at Dallas
Advisor: Dr. Michael Kesden

Employment History:

Teaching Assistant, The University of Texas at Dallas, January 2014 – May 2016
Research Assistant, The University of Texas at Dallas, May 2016 – present

Research Publications:

Servin J., M. Kesden (2017). Unified treatment of tidal disruption by Schwarzschild black holes. Phys. Rev. D, 95, 083001, 2017.

Professional Recognitions and Honors:

Margie Renfrow Scholarship, Natural Sciences and Mathematics, UTD, 2016
Outstanding Graduate Student Presentation Award, 2017 Fall Meeting of the Texas Section of the American Physical Society, 2017

Academic Presentations:

A unified relativistic treatment of tidal disruption by a Schwarzschild black hole, 229th Meeting of the American Astronomical Society, January 2017
Corrections imposed by the Schwarzschild spacetime on the parameter space and bound debris of tidal disruption events, Fall Meeting of the Texas Section of the American Physical Society, October 2017
A new relativistic model for tidal stream evolution during tidal disruption events, 231st Meeting of the American Astronomical Society, January 2018